SYNTHESIS AND CHARACTERISATION OF UP-SCALABLE LAYERED DOUBLE HYDROXIDES FOR ENERGY STORAGE APPLICATION

by

NYONGOMBE EKAMBO GAYI

submitted in accordance with the requirements for
the degree of

MASTER OF SCIENCE

in the subject

PHYSICS

at the

UNIVERSITY OF SOUTH AFRICA

SUPERVISOR: Prof. MS. DHLAMINI

CO-SUPERVISOR: Dr LL. NOTO

Dr G. LEBA KABONGO

OCTOBER 2019

DECLARATION

Name :**NYONGOMBE EKAMBO GAYI**

Student number :**6341-582-8**

Degree :**MSC PHYSICS (98980)**

SYNTHESIS AND CHARACTERISATION OF UP-SCALABLE LAYERED DOUBLE HYDROXIDES FOR ENERGY STORAGE APPLICATION

I declare that the above dissertation is my own work and that all the sources that I have used or quoted have been indicated and acknowledged by means of complete references.

I further declare that I submitted the dissertation to originality checking software and that it falls within the accepted requirements for originality.

I further declare that I have not previously submitted this work, or part of it, for examination at Unisa for another qualification or at any other higher education institution.

_____ _____15th October 2019_____

SIGNATURE DATE

NYONGOMBE EKAMBO GAYI

This dissertation is dedicated to my children

NYONGOMBE EKAMBO Mystère,

NYONGOMBE DIFUMBA Merje,

and my future generation.

“Discipline is the bridge between goals and accomplishment”.

Jim Rohm.

Acknowledgments

I firstly thank God, for giving me strength during these years.

I am sincerely grateful to my promoters, ***Prof. M.S. Dhlamini, Dr. Luyanda NOTO*** and ***Dr. Guy LEBA KABONGO*** for their supports; encouragement and research guidance that made this work a success.

I also acknowledge the support of ***Dr. Bahati MUKERU***.

I sincerely acknowledge the assistance and support that my fellow researchers and staff of the Physics Department of UNISA have given to me during these years.

My great thanks to my spouse ***Mme. Hordaline MAYINGILA*** for her understanding, to my parents ***Mr. Othis DIFUMBA LONGENGO*** and ***Mme. Anne Marie BOSALA BOMBUSA***, to my younger brother ***Mr. Atshitsha ONEMA*** and his Wife ***Mme. Fanny ONEMA*** for their huge support during these years. I also thank my entire family for their encouragement and support during these years.

Special thanks to the ***National Research Foundation (NRF)*** for funding this project. The supports of the ***University of South Africa (Unisa)***, ***Université Pédagogique Nationale (Kinshasa)*** and the ***Ministère de l'Enseignement Supérieur et Universitaire (R.D. Congo)*** are also appreciated.

Summary

The development of cost-effective and scalable synthetic methods is of paramount importance to achieve industrial application of energy conversion and storage devices based on layered double hydroxides (LDH). Herein, we synthesized NiCo-LDH nanosheets via a simple up-scalable co-precipitation method at relatively low temperature. Moreover, we used several characterization techniques to unveil the unique properties of the novel NiCo-LDH among which XRD, EDS, XPS and FT-IR. Consequently, we further investigated NiCo-LDH nanosheets using cyclic voltammetry (CV) and electrochemical impedance spectroscopy (EIS) to evaluate the electroactivity of the as-synthesized NiCo-LDH for energy storage in supercapacitor. Overall, the electrochemical test of the as-synthesized NiCo-LDH revealed remarkable performance exhibiting a specific capacitance as high as **2,140 Fg^{-1}** (5 mV/s).

Key terms

Co-precipitation, energy storage, supercapacitor, layered double hydroxides (LDH), upscalable, large-scale, metal oxides, metal hydroxides.

Acronyms

XRD	: X-ray diffraction
XPS	: X-ray photoelectron spectroscopy
SEM	: Scanning Electron Microscopy
EDS	: Energy dispersive spectroscopy
FTIR	: Fourier Transform Infra-Red
CV	: Cyclic Voltammetry
EIS	: Electrochemical Impedance Spectroscopy
GCD	: Galvanostatic Charge-Discharge
SCs	: Supercapacitors
EDLC	: Electric double layer capacitor
PSC	: Pseudo-supercapacitor
MSC	: Micro-supercapacitor
LDH	: Layered double hydroxides
Ni	: Nickel
Co	: Cobalt
Fe	: Iron
KOH	: Potassium hydroxides
Na_2SO_4	: Sodium sulfate

Table of contents

Chapter 1. Introduction

Chapter 2. Literature review

Chapter 3. Sample preparation and characterization techniques

Chapter 4. Physic-chemical properties of NiCo-LDH

Chapter 5. Conclusion and future works

Chapter 1. Introduction

1.1. Background

The increasing environmental challenges such as the rise of global warming and depletion of fossil fuels have enthused the scientific community to dedicate tremendous effort to the development of various clean energy technologies in recent years [1-4]. Thus, most of the efficient, clean and sustainable energy production sources were successfully developed, such as solar cells, tidal power, wind energy, hydrogen fuel cells, geothermal energy, and so forth. However, most of these energy production sources are not able to generate electric power continually and thus they cannot meet domestic and industrial growing energy demand. Therefore, to store the produced energy from common energy production sources, proper energy storage devices are required [5]. In addition, the electric and hybrid vehicles sector and the demand for energy in modern digital communications (i.e. 5G) also encourage the development of the next generation of energy storage devices exhibiting high energy and power density.

Electrochemical capacitors also known as ultracapacitor or supercapacitors (SCs) are gaining worldwide research interest because of their superior storage capabilities relative to conventional batteries, such as long lifespan, safe operation and high-power density [6-8].

Supercapacitors have the merit to be one of the most effective energy storage devices to date due to their long cycle life, zero maintenance and capability to deliver high power and energy density simultaneously. The recently developed supercapacitor configurations are also displaying several advantages such as fast charging in the order of seconds, the capability to work under wide voltage window, at relatively high temperatures and exhibit exceptionally high number of the charge-discharge cycle (> 500 000) [9-10].

Owing to the above-mentioned advantages, supercapacitors have found numerous applications in memory backup systems, elevators, consumer electronics, bullet trains [11-13] and electric & hybrid electric vehicles [14]. The high power capability of supercapacitors is comparable to that of batteries and it offers an inspiring route to meet the shortage of power in energy storage systems in the up-coming industrial revolution [15].

1.2. Supercapacitors applications

There are several supercapacitors applications and many varied models exhibiting capacities ranging from a few farads to several thousand farads proposed by manufacturers. In recent years, supercapacitors have proved their reliability in embedded systems. Their service life and almost zero maintenance cost allow them to be the component of choice for many applications.

To date, the field of transport is the main field of application targeted for supercapacitors. The best illustration of their reliability in this area is that a module of supercapacitors is associated with an alternator-starter in the e-HDI system developed by PSA, on the Citroën C4 and C5, and 400 000 vehicles are already equipped (see **figure 1.1(A)**). The upcoming implementation of these systems on diesel models will allow fuel consumption to be reduced by 15% and to be in line with the European standard on carbon dioxide emissions of 130 grams of CO_2 emitted per 100 km [16]. Moreover, in Germany a prototype light rail vehicle equipped with a MITRAC storage unit which is based on higher performance supercapacitors connected in series was successfully completed a trial period of four years in the public transportation system (see **figure 1.1(B)**) [17].

Interestingly, the innovative designs of supercapacitors such as flexible supercapacitors are nowadays possible. This opens the field to new applications which is allowing the active material to be deposited on textiles [18]. The best illustration is the first military uniforms sold in 2008 by Sagem to the French Army comprising flexible electronic components and flexible supercapacitors used as energy storage and power supply units (see **figure 1.2**) [18-19].

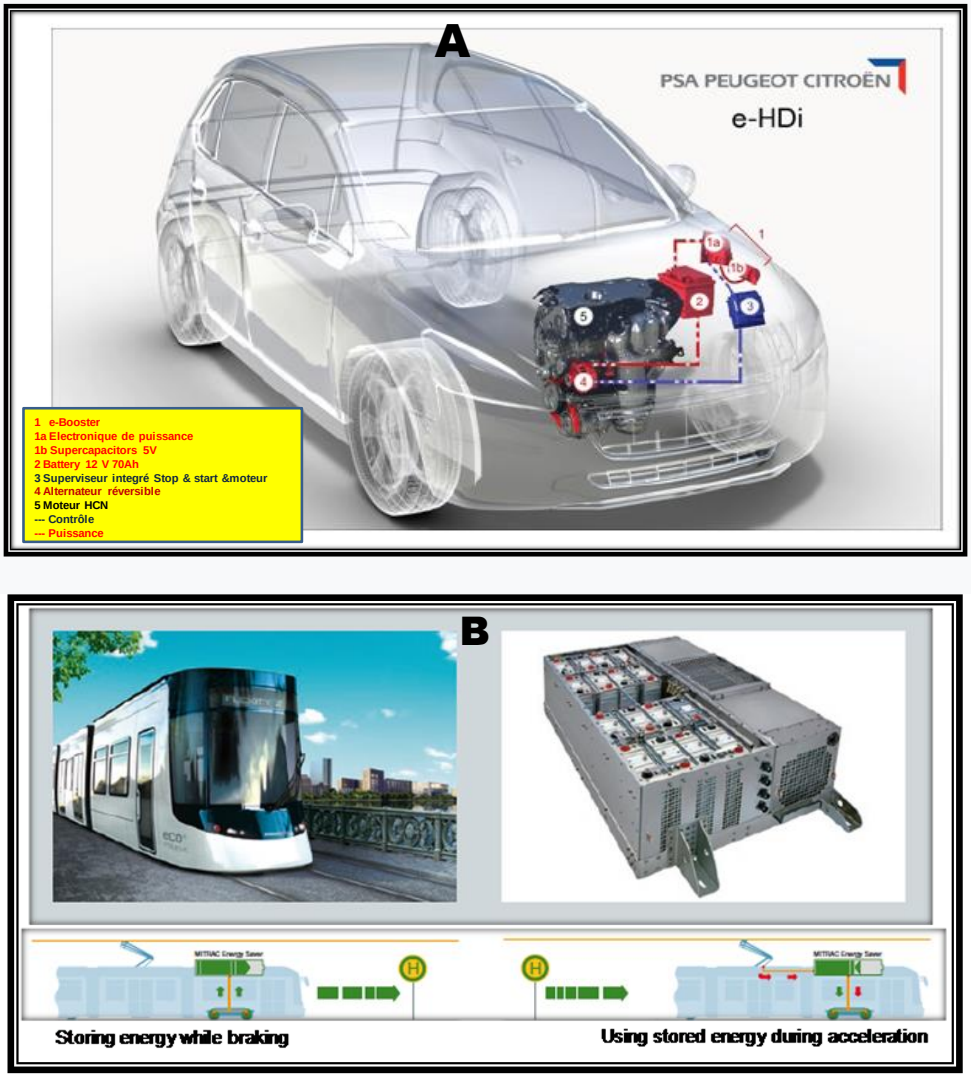

Figure 1.1: (A) Citroën C5 (e-HDI system) [16], **(B)** Tramway filled with MITRAC storage unit[17].

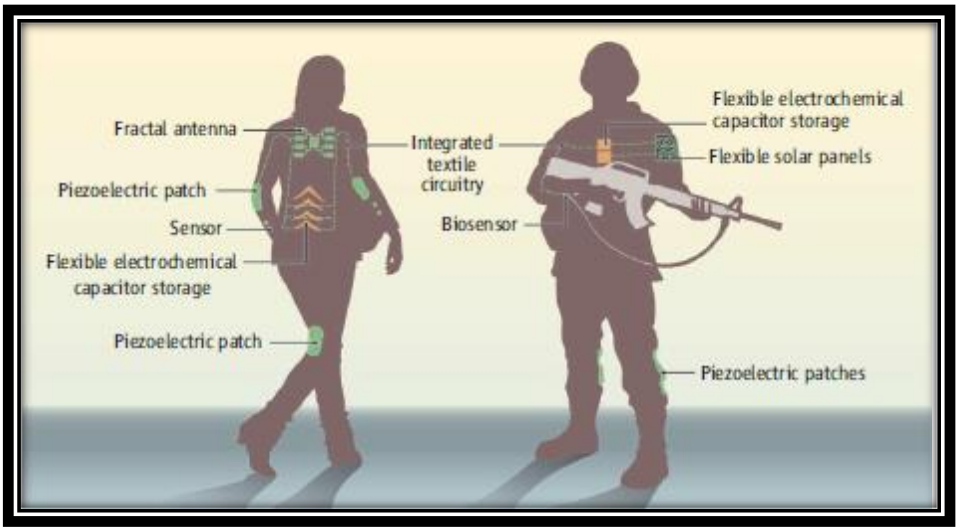

Figure 1.2: Military uniforms comprising flexible electronic components and flexible supercapacitors as energy storage and power supply units[18].

1.3. The problem statement

The energy storage devices remain a hot research topic due to the exponential growth of energy demand across the global arena [20].

Currently, different energy storage technologies are widely researched and developed which include compressed air, flywheel, superconducting magnetic energy storage, pumped hydro and various electrochemical technologies (fuel cells, lithium-ion batteries, Sodium-ion batteries, lead-acid batteries, Zinc-air batteries, super-ionic conductors, solid-state garnet oxides, flow batteries, Lithium-ion capacitors and supercapacitors, etc.) [21].

The important role that each conversion system or energy storage plays is remarkable in the respective areas of dominance. While the popular choice of energy storage for most portable devices is batteries, which attain energy densities of 180 Wh kg^{-1} for Li-ion batteries [22], their electrode materials suffer enormously because of the electrochemical reaction that occurs during the charge/discharge cycling [23].

Batteries store a relatively great amount of energy compared to supercapacitors due to the faradaic storage mechanism. However, batteries suffer a drawback of volumetric expansion. Their storage mechanism does not allow them to deliver high power density due to the volumetric faradaic reactions. During the charging process, the electrolyte ions are stored within the batteries electrodes, while the supercapacitors charge mechanism occurs on the surface of electrodes material. This phenomenon remains the main obstacle, which impedes the usage of batteries for high power performance applications, which usually need fast charging and discharging in short time intervals and favored batteries not to have a long lifetime compared to supercapacitors. Furthermore, batteries encounter thermal management issues [23-24].

Thus, the scientific community is devoting tremendous effort in improving supercapacitor properties to allow their industrial viability. **Figure 1.3 (A)** displays the charge process of batteries, while the supercapacitors charge process is shown in **figure 1.3 (B)**.

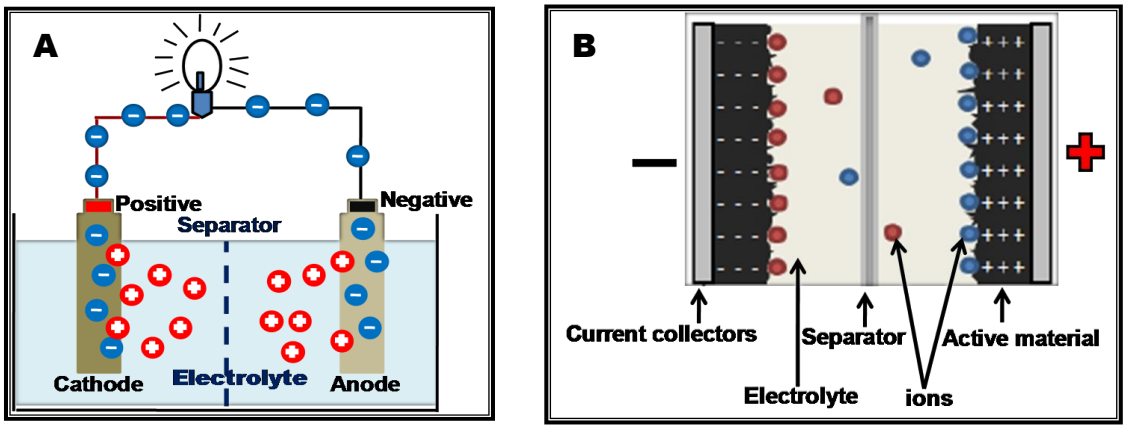

Figure 1.3: (A) Charge process of batteries**, (B)** Supercapacitors charge process.

Supercapacitors are one of the most assuring energy storage devices, which have the ability to transport high power loads within a very short period of time and store large amounts of energy, combining the properties of conventional dielectric capacitors and rechargeable batteries [25–29].

Overall, having superior capabilities and several advantages over other energy storage devices, supercapacitors in principle exhibit a major drawback that permanently limits their practical application. Generally, they have low energy density compared to batteries, which are globally the center-topic of thousands of research reports yearly [30]. Successful engineered electrode interfacial properties can contribute to achieving high specific capacitance, which is one of the keys to improving energy density of supercapacitors available on the market.

This work is focused on the synthesis of Nickel Cobalt layered double hydroxide using a scalable co-precipitation technique with various diverse reactants and on its electrochemical evaluation for application as an electrode material. The main focus is to achieve relatively high capacitive performances which are scarce in the current literature while maintaining structural stability.

1.4. Research aim and objectives

The main aim of this study was to investigate the physicochemical and electrochemical properties of Layered Double Hydroxides (LDH) as supercapacitor electrodes.

Further objectives of the research were:

(a) To synthesize NiCo-LDH via a scalable co-precipitation method,

(b) To use comprehensive analytical techniques such as XRD, FTIR, SEM, EDS, and XPS, to characterize the sample,

(d) To investigate via standardized electrochemical tests the storage capabilities of the as-obtained NiCo-LDH for supercapacitor electrodes.

1.5. Dissertation layout

- **Chapter 1:** Introduces the current dissertation;
- **Chapter 2:** Presents the review of the literature;
- **Chapter 3:** Deals with the sample preparation method and characterization techniques used in this study;
- **Chapter 4:** Discusses the results obtained from NiCo-LDH properties analysis and electrochemical behaviors;
- **Chapter 5:** Summarizes the research findings and suggests future perspectives.

1.6. References

[1] N.T. Suen *et al*., Electrocatalysis for the oxygen evolution reaction: recent development and future perspectives, ***Chem. Soc. Rev***., 46 (**2017**) 337.

[2] Wang *et al*., Quantum dots derived from two-dimensional materials and their applications for catalysis and energy, ***Chem. Soc. Rev***., 45 (**2016**) 2239.

[3] K. Fan *et al*., Nickel–vanadium monolayer double hydroxide for efficient electrochemical water oxidation, ***Nat. Commun***., 7 (**2016**)11981.

[4] V. Litty *et al*., Bioinspired fractal electrodes for solar energy storages, ***Scientific Reports***, 7 (**2017**) 45585.

[5] C.O. Baker *et al*., Polyaniline nanofibers: broadening applications for conducting polymers, ***Chem. Soc. Rev***., 46 (**2017**) 1510.

[6] C. Chen *et al*., All-wood, low tortuosity, aqueous, biodegradable supercapacitors with ultra-high capacitance, ***Energ. Environ. Sci***., 10 (**2017**) 538..

[7] L. Liu *et al*., Unconventional supercapacitors from nanocarbon-based electrode materials to device configurations, ***Chem. Soc. Rev***., 45 (**2016**) 4340.

[8] X. Sun *et al*., Morphology controlled high performance supercapacitor behaviour of the NieCo binary hydroxide system, ***J. Power Sources***, 238 (**2013**) 150.

[9] G. Wang *et al*., A Review of Electrode Materials for Electrochemical Supercapacitors. ***Chem. Soc. Rev***., 41 (**2012**) 797.

[10] I.E. Rauda *et al*., Enhancing Pseudocapacitive charge storage in polymer Templated Mesoporous Materials. ***Acc. Chem.Res***., 46 (**2013**) 1113.

[11] X. Lu *et al*., Flexible Solid-state Supercapacitors: Design, Fabrication and Applications. ***Energ. Environ. Sci***., 7 (**2014**) 2160.

[12] K. Naoi *et al*., Second Generation "Nanohybrid Supercapacitor" Evolution of capacitive energy storage devices. ***Energ. Environ. Sci***.,5 (**2012**) 9363.

[13] L.L. Zhang *et al*., Carbon-Based Materials as Supercapacitor Electrodes. ***Chem. Soc. Rev***., 38 (**2009**) 2520.

[14] E. Karden *et al*., Energy Storage Devices for future Hybrid Electric Vehicles, ***J. Power sources***.,168 (**2007**) 2.

[15] Keita Nomura *et al*., 4.4 V Supercapacitors based on Super-Stable Mesoporous Carbon sheet made of edge-free Graphene Walls, ***Energ. Environ. Sci***., 12 (**2019**) 1542.

[16] http://www.citroen.fr/technologie-ehdi/#/technologie-ehdi/ [Accessed, 25 July 2019].

[17] www.bombardier.com [Accessed, 25 July 2019].

[18] J.R. Miller, Valuing Reversible Energy Storage, ***Science***, 335 (**2012**) 1312.

[19] Jérémy COME, Thèse de doctorat, ***l'Université Toulouse III– Paul Sabatier*** **(2012).**

[20] Bruce Dunn *et al*. Electrical Energy Storage for the Grid: A Battery of Choices, ***Science***, 334 (**2011**) 928.

[21] J.C. Beardsall *et al*., ***Power Engineering Conference*** (UPEC), 50th International Universities (**2015**).

[22] S. Faraji *et al*., Nanomaterials in Advanced Batteries and Supercapacitors, ***J. Power Sources***, 263 (**2014**) 338.

[23] S.M.Chen *et al*., Recent Advancements in Electrode Materials for the High-Performance Electrochemical Supercapacitors. ***Int.J. Electrochem. Sci***., 9 (**2014**) 4072.

[24] B. Conway, Electrochemical supercapacitors: scientific fundamentals and technological applications, ***kluwer academic/plenum***: New York, (**1999**).

[25] P. Simon *et al*., Materials for electrochemical capacitors, ***Nat. Mater***., 7 (**2008**) 845.

[26] L. Zhao *et al*., Nitrogen-Containing Hydrothermal Carbons with Superior Performance in Supercapacitors, ***Adv. Mater***., 22 (**2010**) 5202.

[27]A. S. Arico *et al*, Nanostructured materials for advanced energy conversion and storage devices, ***Nat. Mater***., 4 (**2005**) 366.

[28] J. Fang *et al*., Advances in Nanostructured Composites: Volume 1: Carbon Nanotube and Graphene Composites, ***Electro. chim. Acta***, 85 (**2012**) 248.

[29] M. Armand *et al*., Building Better Batteries, ***Nature***, 451 (**2008**) 652.

[30] Brian Kihun Kim *et al*., Electrochemical Supercapacitors for Energy Storage and Conversion, ***Handbook of Clean Energy Systems*** (**2015**). DOI: 10.1002/9781118991978.hces112.

Chapter 2. Literature Review

2.1. Supercapacitors

2.1.1. Historical background

Becker from General Electric's company is the first known inventor to date who filed the first-ever patent on supercapacitors in 1957 [1]. Becker's supercapacitor invention was based on electrodes designed using porous carbon deposited on stainless steel using an aqueous H_2SO_4 electrolyte. However, the principle of storage charge carriers was not entirely understood at that time and was therefore not included in the invention's description. Later between 1966 and 1970, another reputable company known as Sohio (Standard Oil Company of Ohio) Corporation filed several patents on supercapacitors based on graphite, using an organic electrolyte allowing the increase of the operating voltage [2]. Interestingly, their research and development activities established the link between Helmholtz's work on the double-layer capacity carried out a long time before 1879 [3], and the charge storage process at the electrode/electrolyte interface.

2.1.2. Working principle of supercapacitors

Supercapacitors are devices mainly composed of two electrodes of desired highly porous materials that are electrically isolated using a separator that prevents short-circuiting between electrodes commonly impregnated in a suitable electrolyte. Presently, they are designed and manufactured in several scales, ranging from micro to above centimeters.

Two typical categories of supercapacitors can be considered, the electric double layer (EDLC) and pseudocapacitors (PCs). The EDLC stores the charges in a way such that it is free of any chemical reaction, via electrostatic adsorption of electrolyte ions at the electrolyte/electrodes interfaces. While PCs store energy through a faradaic reaction, which takes place on the

surface of electrodes. During the polarization of a supercapacitor, anions and cations are adsorbed on the surface of the positive and negative electrodes, respectively. Overall, these supercapacitors involve highly performing materials with relatively high specific surface area, between 1000 and 2000 m^2g^{-1}[4].

It is worth mentioning that supercapacitors are usually categorized as symmetric type or asymmetric type due to the type of electrodes used to store charge. The symmetric type supercapacitors involve two electrodes based on the same active material. In contrast, the asymmetric type supercapacitors include electrodes based on different active material. Nevertheless, the asymmetric type supercapacitor mostly exhibit good performance compare to their symmetric counterpart due to the duel contribution of active materials [4,8].

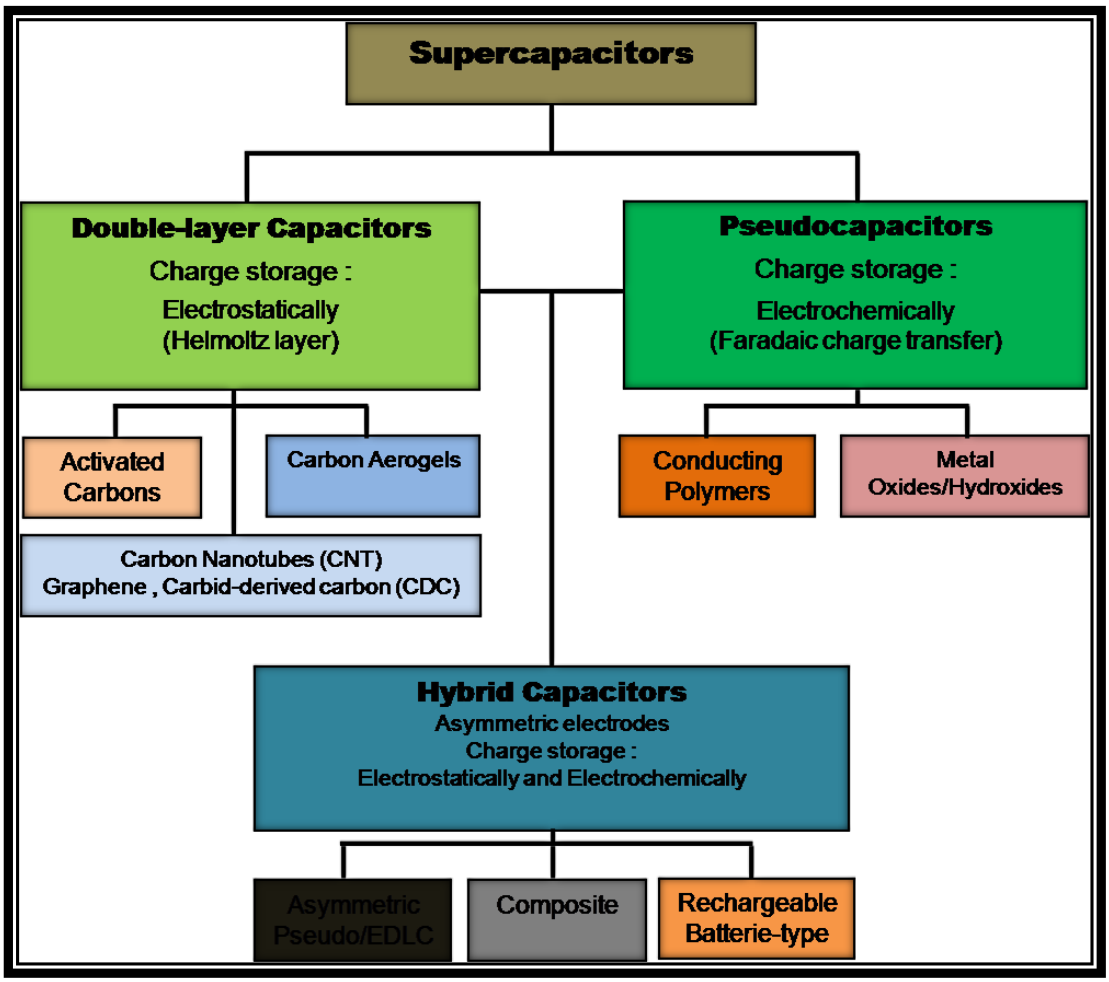

Figure 2.1: Classification of electrochemical capacitors [5].

2.1.2.1. Electric double layer capacitors

In the 19th century, Helmholtz and later, Gouy & Chapman and Stern & Geary have proposed that the ions gathered around the surface of the electrode were the base of a diffuse layer. They also stated that the mechanism was fundamentally different from batteries because the charges are stored on the surface of electrode materials involving no redox reaction. Thus, that charge mechanism is named double-layer capacitance [6-8].

Unlike batteries, during charge/discharge, the above-highlighted mechanism includes no charge movement at the electrode/electrolyte interface and involves no ionic exchange from the electrode to the electrolyte and vice versa; which indicate that no change related to the electrolyte concentration can occur during charge/discharge processes [9]. Thus, the double-layer capacitor charge/discharge electrochemical processes can be expressed as follow [5, 9-11]:

On the positive electrode:

$$E_{s1} + A^- \xrightarrow{\text{charge}} E_{s1}^+ // A^- + e^- \quad (2.1)$$

$$E_{s1}^+ // A^- + e^- \xrightarrow{\text{discharge}} E_{s1} + A^- \quad (2.2)$$

On the negative electrode:

$$E_{s2} + C^+ + e^- \xrightarrow{\text{charge}} E_{s1}^- // C^+ \quad (2.3)$$

$$E_{s1}^- // C^+ \xrightarrow{\text{discharge}} E_{s2} + C^+ + e^- \quad (2.4)$$

Thus, the total charge/discharge process can be expressed analytically as follows:

$$E_{s1} + E_{s2} + A^- + C^+ \xrightarrow{\text{charge}} E_{s1}^- // A^- + E_{s2} // C^+ \quad (2.5)$$

$$E_{s1}^+ // A^+ + E_{s2}^- // C^+ \xrightarrow{\text{discharge}} E_{s1} + E_{s2} + A^- + C^+ \quad (2.6)$$

where:

- E_{s1} and E_{s2} : are carbon electrode surfaces,
- // : is the double-layer containing charges,
- C^+ and A^- : are designed as the cations and anions of the electrolyte.

Nevertheless, it should be noted that each electrode can be considered to be a single capacitor of capacitance (C1) or (C2) which can be assumed as a straightforward proportional improvement to the surface area A of the electrode/electrolyte interface and the electrolyte permittivity **ε** [5].

During electrode immersion in the electrolyte, an excess of charges superficial to the electrode and accumulation of ionic charges on its surface forms the electrochemical double layer, shown in **figure 2.2**. According to Stern, it is consisting of a compact layer, or layer of Helmholtz C_H, and a diffuse layer C_{diff}, also known as layer of Gouy-Chapman. Grahame's model considered an additional layer in the compact Helmholtz layer, which is divided into an internal plane and an external plane. In the case of an aqueous electrolyte, the internal plane is defined by the center of desolvated anions irreversibly adsorbed on the electrode. The external plane corresponds to solvated cations, according to Helmholtz's model [12]. The electric double layer capacitor behavior can be identified form the cyclic voltammetry curve displayed in **figure 2.3.**

Carbon-based materials are mainly used for the electric double layer capacitor electrode materials because they exhibit a high specific surface area, have a good cycling stability, controllable porosity, high maximum power density, and safety. However, the reversible ion adsorption limitation at the electrode/electrolyte interface impedes them to have high specific capacitance. Thus, the pseudo-capacitive materials can achieve that goal and exhibit a good rate capability.

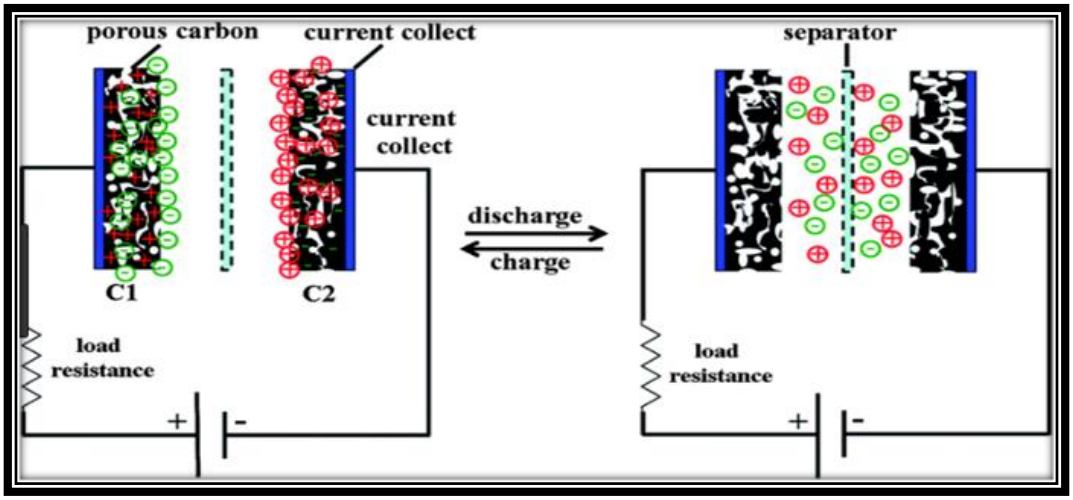

Figure 2.2: Schematic principle of EDLCs [13].

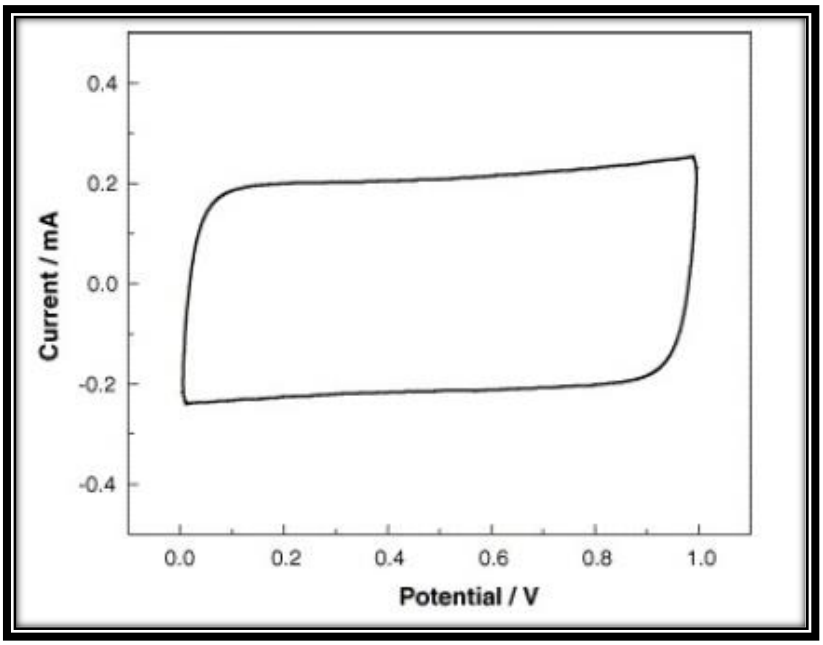

Figure 2.3: Cyclic voltammetry of typical EDLCs [5].

2.1.2.2. Pseudocapacitors

The pseudo-capacitive behavior is generated from certain electro-sorption processes and redox reactions at the surface of the electrode active materials. It is commonly the result of faradaic reactions, which implicate the diffusion of charges across the double layer [5] due to the charge acceptance and the change in voltage [12].

The expression pseudo-capacitive was used to describe the electrochemical behavior of RuO_2 in 1971 and the first PCs were reported [14]. The pseudo-capacitive behavior refers to the reversible faradaic reaction which occurs on the surface of active materials during the charge/discharge process. Three types of pseudo-capacitive behavior exist and can be classified following various faradaic processes. **Figure 2.4** displays the schematic diagram illustrating the three types of pseudo-capacitive behavior, while **figure 2.5** shows a cyclic voltammetry curve identifying the pseudo-capacitive behavior.

a) Under potential deposition

b) Redox pseudocapacitor

c) Intercalation pseudocapacitor

a) Under potential deposition

Generally, this process includes the adsorption of metal atoms and leads its deposition on the surface of a foreign metal, for example on a gold electrode. In the electrolyte, the $Pb^{2+}$is reduced and then a monolayer of lead on the surface of Au electrode is formed, which means the metal atoms are adsorbed and deposited on the foreign metal electrode surfaces as presented in the following equation [15]:

$$\mathbf{Au + \mathit{X}Pb^{2+} + 2\mathit{X}e^{-} \longrightarrow Au\cdot \mathit{X}Pb_{ads}} \qquad \mathbf{(2.7)}$$

b) Redox pseudocapacitor

Under the redox pseudo-capacitance, a metal oxide can be used as the electrode material. For example RuO2, in the vicinity of electrode surface is reduced by the electrolyte ions as shown in the following equation [15]:

$$RuO_x(OH)_y+\delta H^+ +\delta e^- \longleftrightarrow RuO_{x-\delta}(OH)_{y+\delta} \quad (2.8)$$

c) Intercalation pseudocapacitor

In the intercalation pseudo-capacitance process, the active electrode material is constituted as tunnels or layers where the ions will be intercalated to form reversible composites; during the charge and the discharge, the ions are released following the below equation [15]:

$$Nb_2O_5+Li^+ +Xe^- \longleftrightarrow Li_xNb_2O_5 \quad (2.9)$$

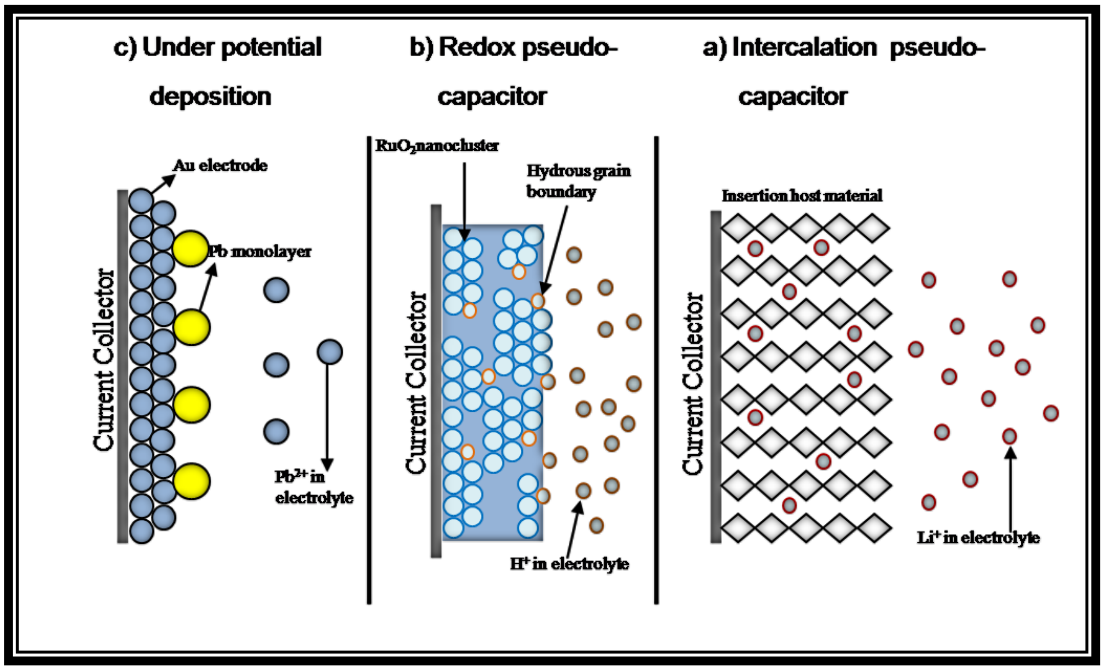

Figure 2.4: Energy storage illustration of PSCs [16].

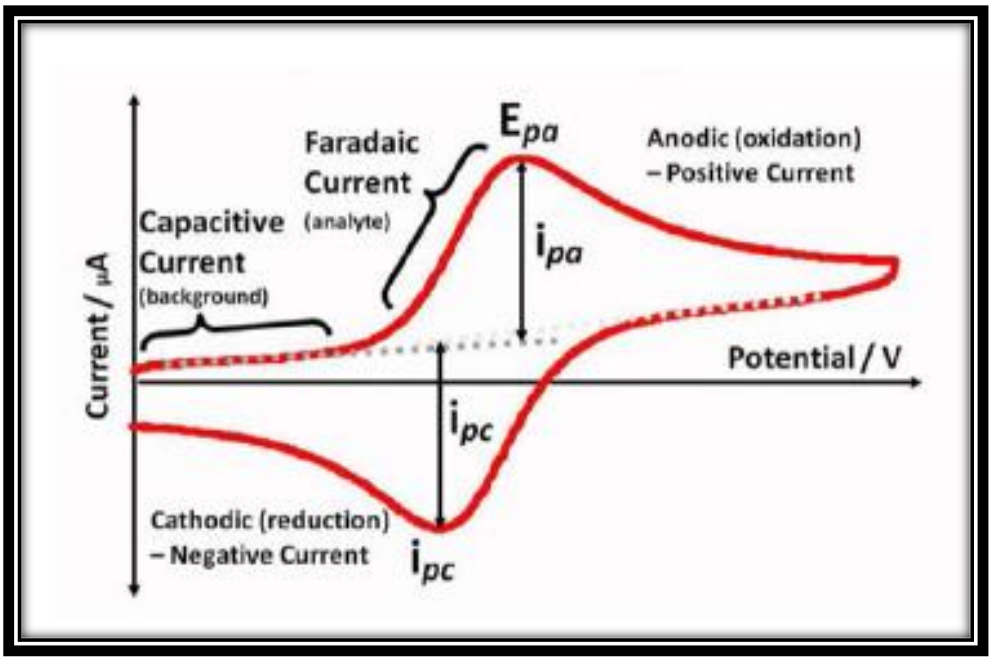

Figure 2.5: Cyclic voltammetry of typical PSCs [5].

2.1.2.3. Micro-supercapacitors

The term "micro-supercapacitors" characterizes the miniaturization of supercapacitors comprised in the scale range from microns to centimeters [17]. The miniaturization of supercapacitors has allowed their integration in the microelectronic components. Thus, the micro-supercapacitors displaying stable performances with excellent safety can be used as energy storage and power supply units in microelectronic modules. Commonly, the device's components should fall within micro scale.

Currently, many asymmetric micro-supercapacitors composed of battery-like faradaic electrode and capacitor-like electrodes have also been reported [18].

Moreover, the potential applications of micro-supercapacitors are very common in wireless sensor networks, nanorobotics, micro-electromechanical systems, wearable microelectronics (e.g., biomedical devices and sensors) and flexible electronics [19–22]. The schematic of the manufacture of micro-supercapacitors based on MnO_2/NCAs and rGO is shown on **figure 2.6**.

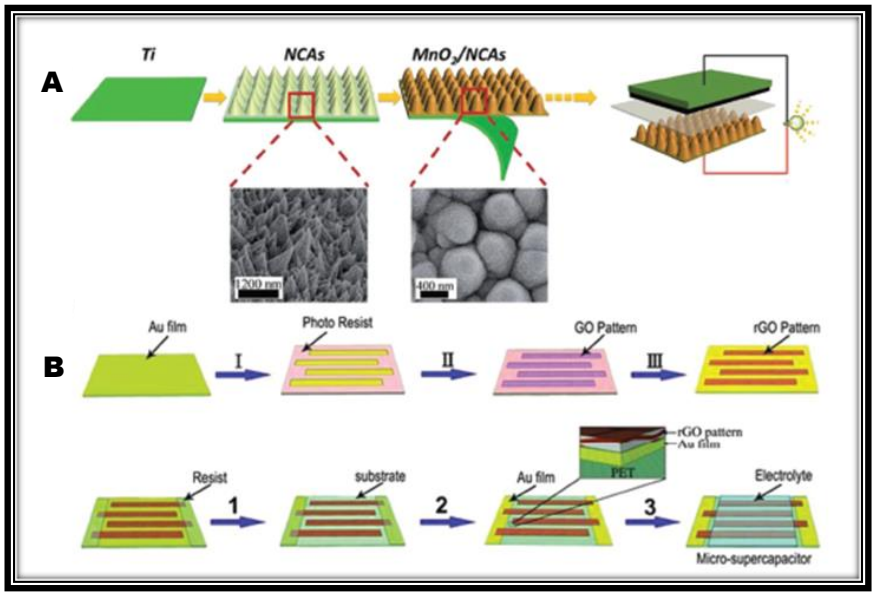

Figure 2.6: A) Schematic of the fabrication of ultrathin MnO_2/NCAs-based MSCs. B) Schematic of the fabrication of rGO MSCs directly on a substrate by electrophoresis method [18].

2.1.3. Evaluation of supercapacitor's performance

The evaluation of supercapacitor's performance is very important in perfecting the technology. Two important parameters can characterize supercapacitors: the energy density (E, Wh Kg^{-1}) and the power density (P, W Kg^{-1}) [4].

The maximum energy density is defined by **equation (2.4)** [4],

$$E = \frac{1}{2} C V^2 \qquad (2.10)$$

where:

- E: the maximum stored energy density (Wh.kg^{-1});
- C: the capacitance of the electrode (Fg^{-1})
- V: the maximum operating voltage (V)

The maximum specific power of supercapacitors is calculated from [23]:

$$\boldsymbol{Pmax = \frac{1}{4Rs} V^2} \qquad (\mathbf{2.11})$$

where:

Rs is the equivalent series resistance of the supercapacitors (in Ω).

These two equations above essentially define the performances of supercapacitors. We note in these two equations that the energy and the maximum specific power both depend on the square of the maximum voltage. This parameter is therefore essential to improve the performance of supercapacitors.

The voltage of the cell is limited by the window of electrochemical stability of the electrolyte. It is, therefore, necessary to use electrolytes having a field of electro-activity as large as possible, to increase both energy and power. Power is the main characteristic of a supercapacitor and it is inversely proportional to the equivalent series resistance of the cell. The electrical resistivity of the electrode materials used, the contact resistance with the current collectors, the ion resistivity of the electrolyte contribute both to the overall resistance of the supercapacitor and must, therefore, be reduced to enhance the specific power.

The energy density is a function of the capacity of the materials used. A compromise can be found between power density and energy density, because the increase of one parameter irremediably causes the decrease of the other and vice versa, so the challenge is to increase the energy density without sacrificing power density in any context [24].

2.1.4. Components of a supercapacitor and their roles

The supercapacitor is composed of two current collectors, an electrolyte, a separator that prevents short-circuiting between two working electrodes (see **figure 2.7**). However, the electrolyte and the electrodes are the foremost components of the supercapacitor because of their significant roles in the achievement of high rate capabilities. High specific capacitance

and a long cycling life belong to an ideal electrode active material, while the high ionic conductivity and the improvement of the voltage window are the results of the electrolyte.

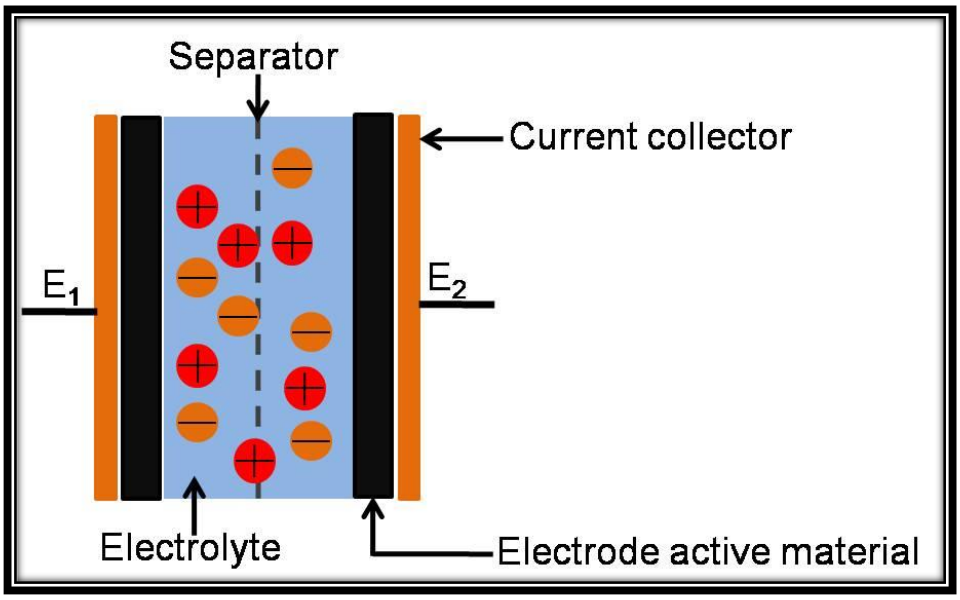

Figure 2.7: Schematic showing supercapacitor device.

2.1.4.1. Current collectors

Current collectors provide electrical contact between the electrode and the active material. Their electrical resistivity must, therefore, be as low as possible. Similarly, they should have good chemical stability in the electrolyte used, as well as stability electrochemically with the applied potentials. They should be mechanically light and resistant to corrosion, in order to contribute as little as possible to the overall mass of the device. Aluminum is used as current collector in organic electrolytes because it has an immunity range compatible with the range of potential studied (about 3 V). However, aluminum is not used in aqueous electrolyte because it is not stable (corrosion, passivation, and dissolution by anodization). The resistance of contact between the active material and the current collector contributes significantly to the internal resistance of the supercapacitor and should accordingly be reduced [25].

2.1.4.2. Electrolytes

Commonly, electrolytes consist of dissolved ions in a liquid solvent. The choice of the electrolyte is critical for the performance of the supercapacitor. Indeed, its ionic conductivity is closely related to the power, and the electrochemical stability window to the voltage of the cell so to energy and power. In addition, so that the adsorption and desorption reactions of the electrolyte ions occur so fast and on the entire surface of the electrodes, the electrolyte should have total access to porosity. The wettability of the electrolyte on active material must, therefore, be the highest possible. The operating temperature is also a parameter that is increasingly taken under consideration in current applications. The ionic conductivity is determined via the **equation (2.6)**:

$$\boldsymbol{\sigma = F\Sigma_i z_i c_i u_i} \qquad \textbf{(2.12)}$$

where:

- σ: ionic conductivity ($S.m^{-1}$)
- F: the Faraday constant ($C.mol^{-1}$)
- z_i: the charge of the ion *i* (number of valence, without unit)
- c_i: the concentration of *i* ions ($mol.m^{-3}$)
- u_i: the mobility of ions *i* ($m^2.V^{-1}.s^{-1}$)

The ionic mobility depends on the viscosity of the electrolyte $\boldsymbol{\eta}$ (in Pa.s), the charge of the ions $\boldsymbol{q}$ (in C), as well as their size defined by the hydrodynamic radius of a solvated species, or Stockes radius $\boldsymbol{r_i}$ (in m) according to the following equation:

$$\mathbf{u}_i = \frac{|\boldsymbol{q}|}{\boldsymbol{6\pi\eta r_i}} \qquad (\mathbf{2.13})$$

The most commonly used electrolytes for supercapacitors are the aqueous, the organic and ionic liquids. Their physicochemical properties are illustrated on **table 2.1**. Moreover, the solid-state electrolyte is the recent unveiled electrolytes having good properties for portable electronic devices and wearable applications.

a) Aqueous electrolytes

The aqueous electrolytes possess fast ion transportation during the process of charge/discharge, which is the result of their high ionic conductivity and low resistance. However, their voltage window is limited to < 1.2 V caused by the decomposition effect of solvent water which disadvantage and limit the power and energy density. The following chemicals are widely used in aqueous electrolytes preparation: H_2SO_4, KOH, KCI, Li_2SO_4, Na_2SO_4, and NH_4Cl [16].

b) Organic electrolytes

The organic electrolytes provide excellent properties as compared to their aqueous electrolytes counterpart, having a large voltage window up to 3.5 V which can strongly contribute to the improvement of the performance of supercapacitors. However, their main disadvantage is that their voltage window can significantly be reduced caused by the absorption of water, owing to their weakness in the event of moisture. The chemicals commonly used to prepare organic electrolytes include ethy-methylimidazolium bis (trifluoromethylsulfonyl) imide (EMIM TESI) and $TEABF_4$, tetreethyphoniumtetrafluoroborate (Pet_4-BF_4) are largely used for supercapacitors [26-31].

c) Ionic liquids and solid-state electrolytes

The chemical stability, the wide range of voltage window (2.0 to 6.0 V), the high thermal and the low flammability are the main advantages of ionic liquids electrolytes, making them excellent candidates for the fabrication of supercapacitors. However, at certain temperatures, the smelting of salts which is present in certain chemical used for those electrolytes such as: the imidazolium, aliphatic, pyrrolidinium ammonium salts and cyclic amines included in ionic liquids, can impede their applications in supercapacitors planned to be used in some areas that need a large range of temperature [31-36].

Table 2.1: The physicochemical properties of electrolytes [25].

Nature of electrolyte	aqueous	Organic	Ionic liquids
Electrochemical stability (V)	≤ 1,2	≤ 5	3.0 to 6.0 V
Ionic conductivity ($mS.cm^{-1}$)	>400	≤ 100	≤ 15
Temperature (°C)	-20 to +50	-40 to +80	-100 to +400

In general, supercapacitors using electrolytes in liquid phase require a high cost of packaging and after packaging, their size increased. However, their usage for wearable applications is avoided because of possible electrolyte leakage. Thus, the solid-state electrolytes are the best ever candidates for wearable devices exhibiting excellent properties such as flexibility, high safety, small size and low weight [37].

The solid-state electrolytes are composed of polymers. The widely used are polymer-based gel electrolytes. Poly (ethylene oxide) (PEO), Poly (vinyl alcohol) (PVA), Poly (vinylidene fluoride) (PVDF), Polyacrylonitrile (PAN), Poly (vinylidene fluoride-co-hexafluoropropylene) (PVDF-co-HFP), Poly (methyl methacrylate) (PMMA), Poly (ethylene glycol) blending Poly (acrylonitrile) (PAN-b-PEG-b-PAN) and Poly (amine-ester) (PAE) are mostly included in the usually used polymers [38-41].

2.1.4.3. Electrodes materials

The major problem that impedes supercapacitors to be used for practical applications is its low energy density. Exploring electrodes interfacial properties with high specific capacitance is one of the keys to improving the energy density of supercapacitors. The achievement of that goal depends intimately on the active materials used. Therefore, the selection and the preparation of the active electrode materials must be done with particular care.

It is necessary to use a non-polarizable electrode, electrically conductive and possessing a large specific surface area in order to reach high capacities. The carbon-based materials, the conducting polymers, and the metal oxides/hydroxides are the three main types of materials used as supercapacitors electrodes active materials.

a) Carbon – based materials for supercapacitors

Carbon is a material whose porosity is easy to develop by different existing carbonated structures (sp^2, sp^3 ...). It is the main electrodes active materials used for the EDLC supercapacitors. It has also good electronic and stable conductor electrochemically in a wide range of potential (~3 V). However, the carbon in different forms has been tested as an electrode for supercapacitors [37,42-44], including carbon nanotubes, graphene sheets, carbon onions, fibers [45], carbon blacks [46], carbide-derived carbons [47], or activated carbons [48]. These are the latter mainly used as active materials in supercapacitors because they have a very high specific surface area, electrical conductivity in the order of 50 $S.cm^{-1}$, good thermal stability, excellent corrosion resistance for a moderate cost [49].

Most of supercapacitors available in the market utilize activated carbon. They are produced by the first stage of the carbonization of organic precursors under an inert atmosphere. Natural materials (coconut shell, wood, charcoal), or Synthetics (polymers) can be used as precursors. After carbonization, activation creates pores in the amorphous carbon structure, creating a random network and interconnected porosity and developing a specific surface that can reach 3000 m^2g^{-1}. However, carbon material can also be submitted to further treatment in order to adjust its chemical structures and other properties for its suitability in diverse applications [8].

Carbon-based electrodes of supercapacitors are interesting because they offer high power with relatively low costs of active materials. The capacity of activated carbons can be considered in this first approach as proportional to their specific surface. A lot of work has been done to increase the capacity of the active materials by developing porous carbons with a high specific surface area. However, this approach has been shown to have considerable limitations. By testing activated carbons of several surfaces, Kötz *et al.* showed that at values above 1500 $m^2.g^{-1}$, the mass capacity does not exceed 100 $F.g^{-1}$ [49-50]. They attributed this limitation to the decrease of the pore wall thickness of carbon with the increase of the specific surface area. This tightening of the distance between the pores reduces the screen effect of carbon, which increases the repulsive interactions between ions and decreases the attractive interactions between ions and carbon [51].

b) Conducting polymers

The conducting polymers possess high specific capacitance compared to the limited capacitance of carbon materials. Conducting polymers are also referred to as "synthetic metals" of 1 to 100 $S.cm^{-1}$ [52]. They are constituted of the succession of saturated and unsaturated bonds between the hybridized carbon atoms sp^2, which gives them a planar configuration. This configuration is necessary for good electrical conductivity; it promotes the recovery of carbon orbitals, which leads to the hybridization of π type. The strong conjugation of the orbitals is responsible for the electrical conductivity. The introductions of charges in the polymer provoke faradaic reactions and a continuous variation of the potential; that is the reason why those materials are defined as pseudo-capacitive. When a conductive polymer is used as an electrode, the electrochemical reaction involved the doping/dedoping of the polymer depending on electrons injection or snatching. Thus, when the polymer is doped, the ions of the electrolyte are inserted into the polymer chain in order to keep the local electroneutrality. The terms "N doping " and "P doping " are then used to describe the reduction and oxidation reactions respectively, according to the reactions below [25]:

$$\mathbf{Polymer^{(o)}+e^{(-)}+cation^{(+)}} \underset{\text{N de-doping}}{\overset{\text{N doping}}{\rightleftharpoons}} \mathbf{polymer^{(-)}cation^{(+)}} \qquad \mathbf{(2.14)}$$

$$\mathbf{Polymer^{(o)}+anion^{(-)}} \underset{\text{P de-doping}}{\overset{\text{P doping}}{\rightleftharpoons}} \mathbf{polymer^{(+)}anion^{(-)}+e^{(-)}} \qquad \mathbf{(2.15)}$$

Most conducting polymers involve p-doping, which is easier to obtain than n-doping, sensitive to the oxidation in the ambient air, which decreases its life. In addition, the conductivity of conducting polymers doped n is generally lower, which increases the resistance of the electrode and decreases the capacitance. Moreover, the coulombic reversibility of conducting polymers is low, and attributed to a phenomenon of charge-trapping, responsible for the partial trapping of ions in the entanglement of polymer chains, preventing their extraction. Typically, supercapacitors based on conducting polymers suffer a

loss of more than 10% of their capacity after 1000 cycles. Thus, these materials are currently neglected for this type of application. Furthermore, the insulating properties of dedoped polymers and the low operating voltage limit the power density of these supercapacitors [44]. **Table 2.2** compares electrochemical properties of main types of conducting polymers.

Table 2.2: Electrochemical properties of certain conducting polymers [25].

Conducting polymers	Conductivity ($S.cm^{-1}$)	Type of dopage	Capacitance ($F.g^{-1}$)
Polypyrrole(Ppy)	10 - 50	p	240
Polyaniline (PANI)	0,1 - 5	p	530
Polythiophene (PHT)	300 - 400	p n	260 -
Poly(3-methylthiophene)	>500	p n	220 165

c) Metal oxides/hydroxides

Metal oxides/hydroxides show excellent charge storage abilities, good cycling stability than conducting polymers and high specific capacitance relative to carbon materials. Supercapacitors using metal oxides/hydroxides as electrode materials present simultaneously good energy density and high power ability [44].

Metal oxides/hydroxides are widely studied in the field of energy storage with a focus on supercapacitors, because of abundance of metal based materials and a large number of compounds that can be synthesized. It should be noted that various electrochemical characteristics also depend on it. However, most of those metal oxides/hydroxides exhibit pseudo-capacitive behavior. Among those materials, ruthenium oxide and manganese oxide are the most studied because of the capabilities of several hundred farads over a wide potential window that can be reached at high sweeping speeds. It is worth mentioning that the vast majority of pseudo-capacitive oxides operate in aqueous electrolyte [16].

➢ Ruthenium oxide (RuO_2)

Ruthenium oxide with 700 F g^{-1} was the first report on metal oxide as electrodes materials for supercapacitors [38]. The enhancement of the ruthenium oxide theoretical maximum capacitance (1450 Fg^{-1} with a voltage window of 1 V) is the result of the presence of structural water. Ruthenium oxide as an electrode materials exhibit a high proton conductivity, good thermal stability, and high cycling stability. Nevertheless, its usage is limited for a large range of applications because of the rarity (in the earth crust) and the expensive cost of the material [16].

➢ Manganese oxide (MnO_2)

Manganese Oxides (MnO_2) exhibits promising properties as compared to RuO_2, such as its low cost, it is abundant in the earth crust and environmentally friendly [53-55]. The charge storage mechanism of MnO_2 is shown in equation 2.14 [54].

$$\mathbf{MnO_2 + C^+ + e^- \leftrightarrow C^+MnO^-_2} \qquad \mathbf{(2.16)}$$

where:

- ❖ C^+ : is the electrolyte cations or protons
- ❖ MnO_2 : is the storages charges by a redox reaction (oxidation states of Mn: +4 and +3).

However, the improvement of the capacitive performance of MnO_2 by the understanding of the charge storage mechanism is still remaining a hot research topic [56-57].

MnO_2 exhibit a theoretical capacitance of 1233 Fg^{-1} with a potential window of 0.9 V, meanwhile, despite tremendous efforts made in order to increase the charge capability of MnO_2, the capacitive performance of MnO_2 remained not satisfactory because of its poor conductivity (10^{-7} to 10^{-3} S/cm^3) [58-61].

Considering the unsatisfactory performance of MnO_2, several other materials have been also studied and confirmed to be promising pseudo-capacitor electrode materials; such as Mn_3O_4 [62], Fe_3O_4 [63], V_2O_3 [64], SnO_2 [65], CuO [66], Cu_2O [67], MoO_3 [68], MoS_2 [69], Nb_2O_3 [70], $Na_3Ti_3O_2$ [71], WO_2 [72], Bi_3O [73].

However, despite materials cited above, Nickel and Cobalt based materials have been reported as excellent electrode material candidates for supercapacitors due to their high theoretical capacitance, best chemical stability, low toxicity and low cost [74]. The first specific capacitance of 50 to 64 $F.g^{-1}$ had been obtained with NiO/Ni composite film in the 1990s, while the capacitance obtained with Cobalt was 291 $F.g^{-1}$ [75,76]. Since then diverse Nickel and Cobalt based materials have been developed. Most of them have exhibited the best capacitive performances for supercapacitor applications.

Presently, Nickel and Cobalt based materials containing oxides [77-80], hydroxides [81-83], sulphides [85-86], selenides [87-89], phosphide [90-92], phosphates [93-95] and layered double hydroxides (LDH) [96] are used as pseudo-capacitive materials for supercapacitors.

Among them, Nickel-Cobalt LDH materials are gaining tremendous momentum and becoming the center of attention of a large number of studies due to their high surface area and rapid intercalation/de-intercalation of charge ions amidst of the layered structure [16].

2.2. Layered Double Hydroxides for supercapacitors applications

LDH is a class of ionic lamellar compounds, also known as anionic clays (see **Figure 2.8**). To date, they become the center of a massive research interest because of their excellent properties, such as facile synthesis, unique structure (see **Figure 2.9**), unvarying dispersion of different metal cations in the brucite layer, good chemical stability and easy tenability through the intercalation of numerous varieties of anions (inorganic, organic, biomolecules, and even genes) [97].

The most interest part of LDH among other layered materials is the feasibility to obtain the composition and combination of metal-anions [97].

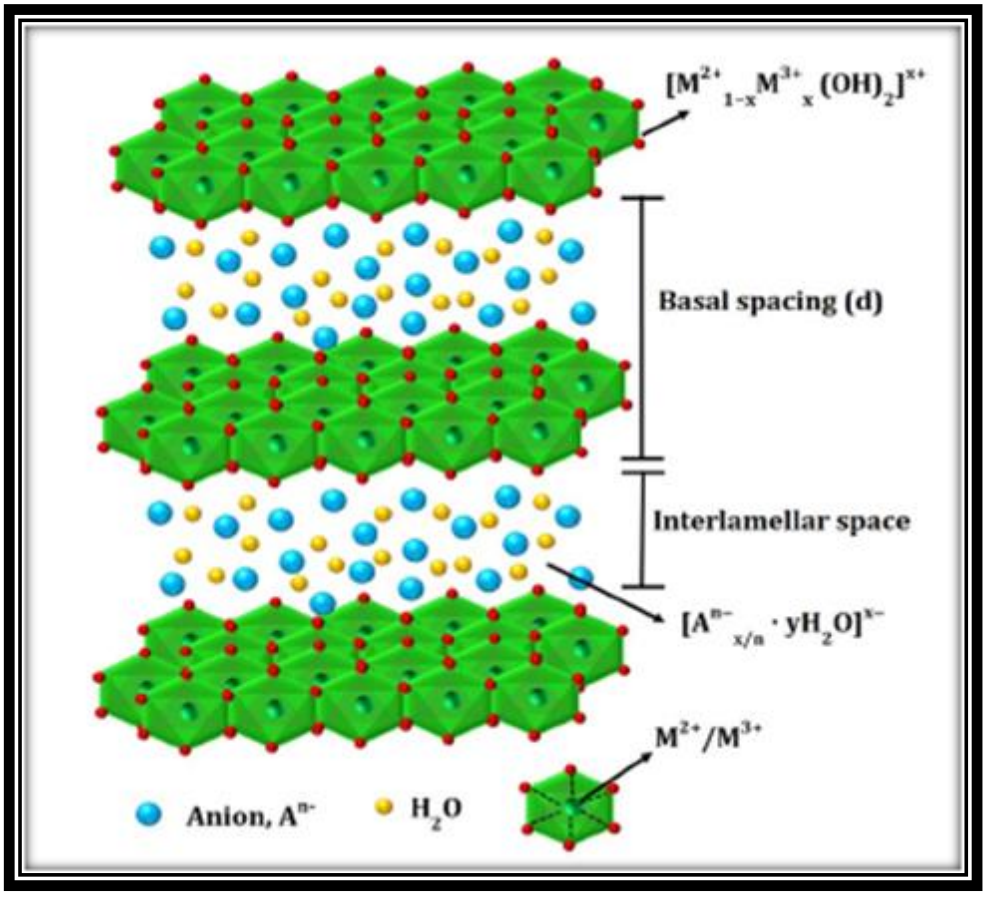

Figure 2.8: Structure of layered double hydroxide [97].

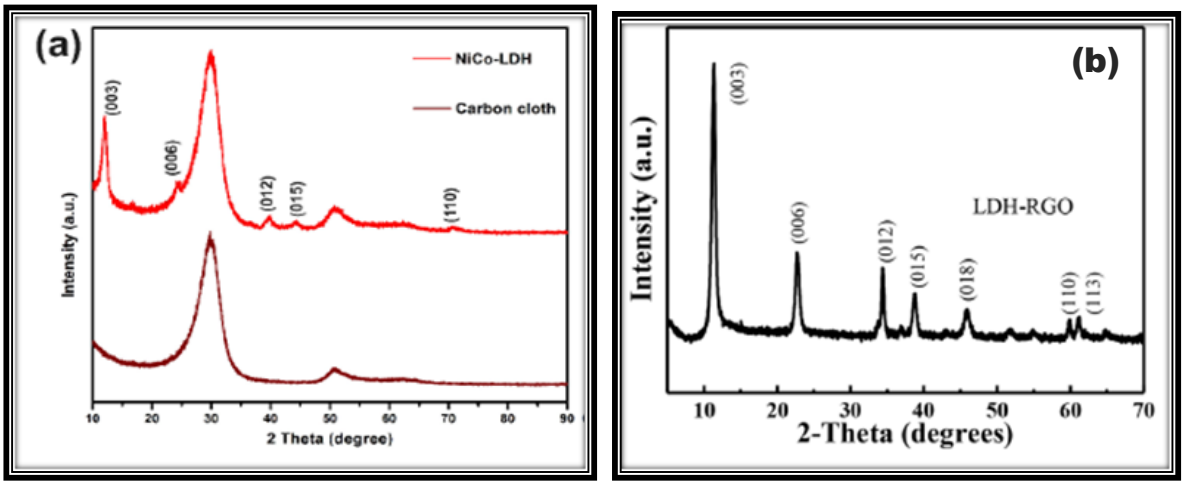

Figure 2.9: XRD patterns showing the crystalline structures of (a) NiCo-LDH (b) LDH-RGO [99,112].

2.2.1. Description of Layered Double Hydroxides structure

The LDH structure is settled on $M(OH)_6$ octahedral units sharing their borders to form $M(OH)_2$ brucite-like layers. These octahedral units comprise the divalent and the trivalent metallic cations. Moreover, the principal layers are charged positively and the charge density is directly related to the arithmetical values of the trivalent metal ratio $x = M^{III}/(M^{II} + M^{III})$ [98].

Nevertheless, the entire structure is composed by the stacking of such layers, intercalating charge-balancing anionic species, and water molecules (see **figure 2.10**). The general LDH chemical formula can be reduced as $[M^{II}\text{-}M^{III}\text{-}X]$ [98].

To date, several authors have demonstrated that during the faradaic redox charge transfer, the surface of a LDH is not the only part that participates; they have stated that the entire crystalline structure is also involved in the charge storage mechanism via intercalation/de-intercalation of electrolyte ions favoring LDH to possess excellent energy storage capabilities [99-101].

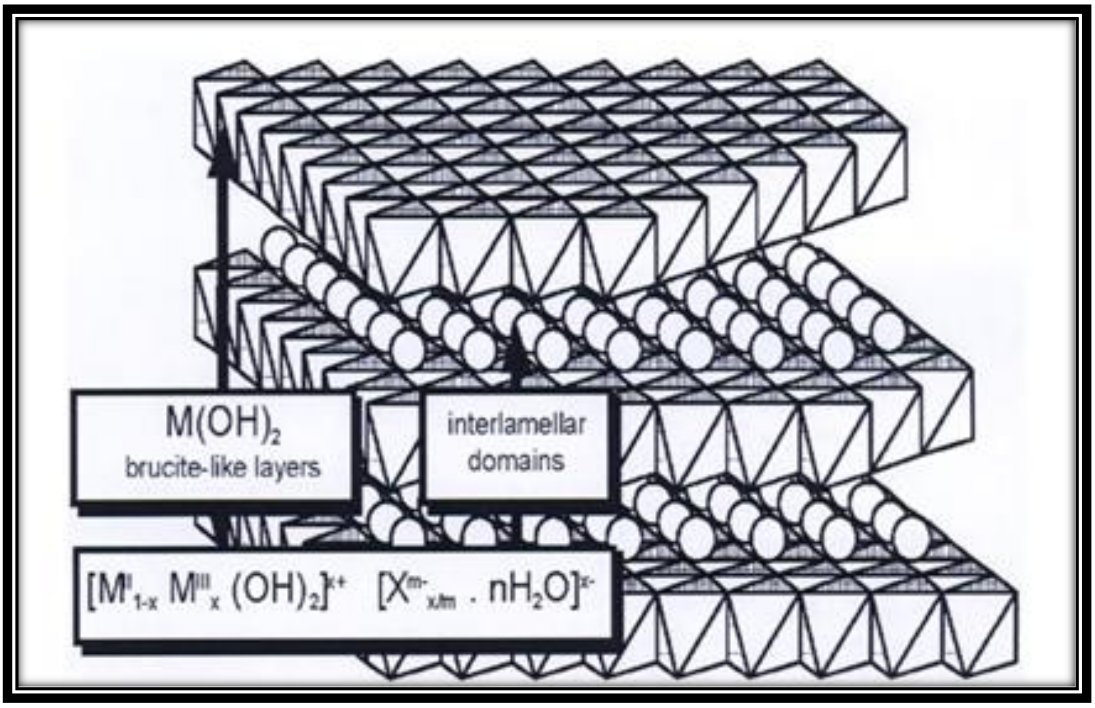

Figure 2.10: Schematic view of LDH structure and general formula [98].

2.2.1.1. Metal cations in the layers

Most of the divalent and trivalent metal cations discovered in LDH are the property of the third and fourth periods of the periodic classification of the elements [98].

- Divalent cations : Mg, Mn, Fe, Co, Ni, Cu, Zn.
- Trivalent cations : Al, Mn, Fe, Co, Ni, Cr, Ga.

❖ Trivalent metal ratio

Generally, several layered double hydroxides systems can fit a large range of trivalent ratios. However, it is not studied and reported because of the variation that occurs from 0 to 1 without involving any change within the main structural configuration. Layered double hydroxides display a high charge density on the main layers. This can be explained by the example below [98]:

[*a x = 1/3 trivalent metal ratio corresponds to one charge for 50 Å^{2}on each side of the layer, leading to one charge for 25 Å^2 in the interlamellar domains [98].*]

❖ Interlamellar domains

LDH interlamellar domains comprise anions, water molecules and most of the times some neutral or charged moieties. Generally, there is no huge number of bonding which takes place between these interlamellar ions or molecules and the host structure [98]. Because several anionic species can be introduced between the layers, especially when the lamellar structure undergoes its formation by anionic exchange among others [98].

The following anions can be located between the layers:

- Halides: fluoride, chloride, …
- Oxo-anions: carbonate, nitrate, sulphate, bromated,…
- Oxo and polyoxo-metallates: chromate, dichromate, $(Mo_7O_{24})^{6-}$, $(V_{10}O_{28})^{6-}$,…
- Anionic complexes: ferro and ferricyanide, $(PdCl_4)^{2-}$, …
- Organic anions: carboxylates, phosphonates, alkyl sulphates,…

However, it should be noted that there is a close correlation between the size, charge, and layout of these interlamellar species because they can lead to the modification of the basal spacings of the layers (see **figure 2.11**). That is the reason a stringent selection should be done, either an inorganic or an organic species [98].

- In LDH, large distance between the brucite and the smallest basal spacings is an indication of intercalation of an interlamellar monolayer,
- The small gap for some types of small anions such as hydroxyl, fluoride, carbonate, chloride, corresponds to a "leveling" which is the effect of water molecules.

In addition, in the case of inorganic anions intercalation LDH, the basal spacings are lower than 15 Å, while for organic anions the gap is larger than 15 Å [98].

Recently, Yinyin Lin et al., have synthesized NiCo-LDH nanosheets by introducing sodium dodecylbenzene sulfonate (NiCo-SDBS-LDH) within the interlayer region of LDH, resulting in a remarkable specific capacitance of 1094 Fg^{-1} at 5 A g^{-1} and a super long cycle life with 81% retention over 3000 cycles [102].

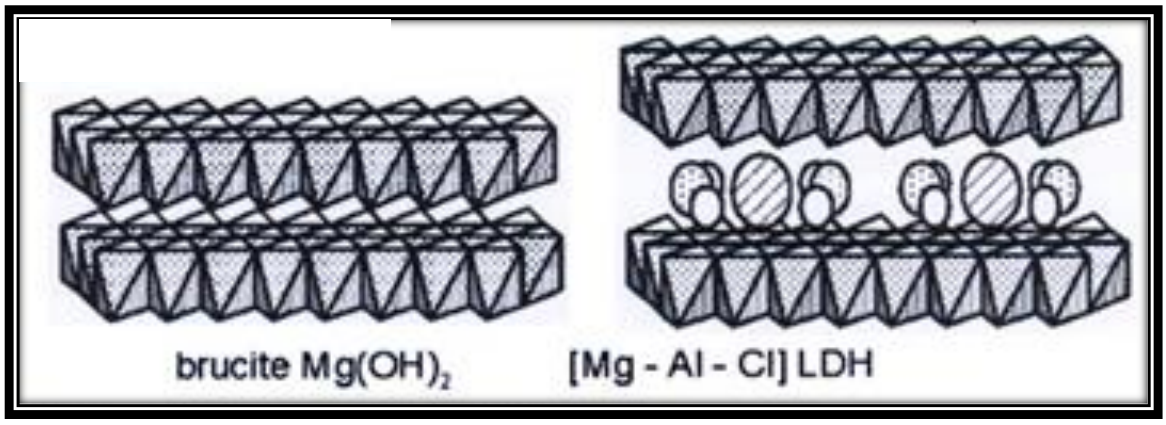

Figure 2.11: Evolution of basal spacing with intercalated anions [98].

❖ Contribution of water within the LDH structure

There are a number of sites where water related molecules can be hosted in LDH. The presence of water within LDH can be characterized using infrared spectra analysis. The LDH water bending is between the region from 1500 to 1700 cm^{-1}, followed by O-H stretching vibrations in the region of 3000-4000 cm^{-1} [98].

Various forms of water related molecules in LDH:

- Water between the interlayer of the hydroxide layers,
- Adsorbed water on the outer surface,
- Free water between the particles.

Previous studies have demonstrated that the presence of water within LDH is highly beneficial for their electrochemical performances. V. Rives reported that when in the brucite, a portion of M^{II+} is replaced; the anions located in the interlayer region together with water molecules balance the positive charge of the layer [103]. Consequently, it was also reported that the incorporation of anions in the interlayer region is always along with the molecules of water for the restoration of charge neutrality and stability [104]. Moreover, it has been demonstrated that according to the mechanism of anion exchange reactions of LDH, the interlayer interactions of LDH can also be mediated by the hydrogen bonding between the hydroxyl groups of the layer with the anions and the molecules of water within interlayer [105]. In the same direction, Richetta *et al.*, reported that the presence of water in LDH structure, no matter their types, whether crystallite water or water adsorbed contributes greatly to the spectacular characteristics of layered double hydroxides [106]. Finally, Teng Wang *et al.*, reported that the hydrophilic nature of LDH is highly advantageous in improving the ionic diffusion in aqueous solution electrolyte [99].

In 1915, Manasse E professor of mineralogy at the University of Florence (Italy) reported for the first time the hydrotalcite stoichiometry of LDH $[Mg_6Al_2(OH)_{16}](CO3)\cdot_4(H_2O)]$ [107]. Thus, hydrotalcite was given as a name referring to its hydrophilic nature and its similarity to talc (talcite). Then later in 1968, Allmann demonstrated the structure and the properties of

LDH through XRD, following by Taylor in 1969 [108,109], it was confirmed that most of LDH have the same structure than the mineral hydrotalcite (HT).

To date, numerous LDH composites have been reported. Afriyanti Sumboja et al. reported on efficient electrocatalysts made by NiMn layered double hydroxides for the oxygen evolution reaction and their application in rechargeable Zn–air batteries [110]. On the other hand, Feifei Wang *et al*., reported on a novel CoNiFe-LDH/CNFs-0.5 composite exhibiting 114.2 m^2g^{-1} and 1203 Fg^{-1} at 1 Ag^{-1} as specific surface area and specific capacitance, respectively [111].

Beyond energy storage, the outstanding physicochemical properties of LDH have been world widely acclaimed in a variety of technological applications as depicted in **figure 2.12**.

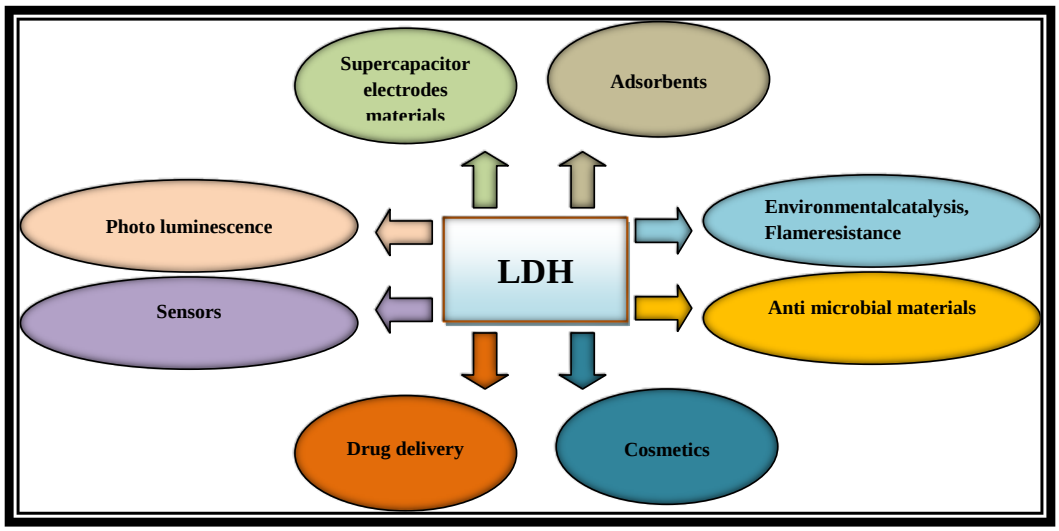

Figure 2.12: Different applications of LDH.

2.2.2. Different synthesis method of LDHs

A number of studies devoted to the preparation of LDH have been discussed in the recent past years. He *et al*., [112], Khan and O'Hare [113] and Rives [98], have reported about many facile as well as expensive preparation procedures of LDH for diverse applications. However, in this section, the attention will be given to two of them: the co-precipitation method (direct method) and the anion-exchange method (indirect method).

2.2.2.1. Co-precipitation method

The co-precipitation method is the most usually applied technique for direct synthesis of LDH with various divalent and trivalent cations and different anions. It can also be applied for large-scale fabrication of materials. The inorganic anions, such as Cl^-, NO_3^-, and CO_3^{2-}, the organic molecules and large biomolecules can be intercalated [114,115]. The goal with the co-precipitation method is the slow addition of a solution having targeted anions, which must be intercalated into the solution of divalent and trivalent metal cations present into a container, respecting an appropriate ratio. It is desired that the pH be increased during the operation by adding a base or urea for hydrolysis that contributes to the precipitation of the LDH as displayed on **figure 2.13**. The above presented mechanism is totally based on the condensation of hexa-aqua metal complexes in solution, allowing the brucite-like layers to be formed with a uniform distribution of metallic cation with solvated interlamellar anions [116]. It is important to mention that several types of LDH and their composites have been synthesized via co-precipitation method for various purposes.

Finally, in recently hot identified research Shao *et al*., reported on Zn-Ti LDH exhibiting high crystallinity and significant photocatalytic activity [117]. Also, R. Li *et al*. synthesized through the co-precipitation method a Large Scale $Ni_{50}Co_{50}$-LDH supercapacitor electrode exhibiting excellent specific capacitance of 1537 F g^{-1} at 0.5 A g^{-1} [74].

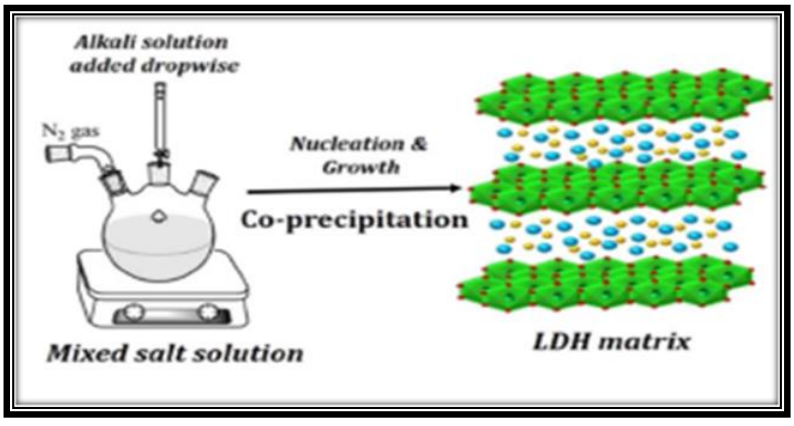

Figure 2.13: Schematic representation of co-precipitation method of LDH [97].

2.2.2.2. Anion-exchange method

Anion-exchange, also known as an indirect method is a frequently used synthesis method of LDHs composites. It is a practical route for the intercalation of a number of various types of anions [114,118-119]. In the later of their formation, by stirring the LDH precursor, the anions present in the interlayer region will be exchanged for intercalation with the desired anions in a solution with an excess anion [120].

The host-guest exchange is usually linked to the electrostatic forces based between the positive charged LDH layers and the exchanging anions [121]. Nevertheless, as the electrostatic interaction with the layers is weak, the anions present in the interlayer can be easily replaced by those which possess high electrostatic interaction with layers [97]. **Figure 2.14** displayed the schematic representation of the ion-exchange method. Two possible routes can be used to intercalate targeted anions, as shown in the following equations [97]:

$$\mathbf{LDH{\cdot}X^{m-} + Y^{n-} \rightarrow LDH{\cdot}(Y^{n-})_{m/n} + X^{m-}} \qquad \mathbf{(2.17)}$$

$$\mathbf{LDH{\cdot}X^{m-}Y^{n-} + mH^{+} \rightarrow LDH{\cdot}(Y^{n-})_{m/n} + H_mX} \qquad \mathbf{(2.18)}$$

The anion-exchange reactions of LDH are usually associated with the following main features:

1. The anion-exchange process might be favored by the appropriate solvent.
2. The chemical composition of the brucite type layers determines the process.
3. Anion-exchange process will be optimal at high temperatures.
4. It must be noted that under the working pH lower than 4.0 the hydroxyl layers will be broken, that is why it is preferable to keep the working pH at 4.0 or above 4.0.

Das and Parida, reported that it is challenging to synthesize the hybrid LDH composites using the co-precipitation method and confirm that anion-exchange method presented many advantages and has been adopted as an excellent route over the traditional co-precipitation

[125]. Thus, various types of LDH composites have been synthesized using the anion-exchange method in order to get satisfactorily materials properties out of the LDH precursor.

More importantly, it should be pointed out that the unique role that each method plays is clear in their region of dominance. While the anion-exchange method is excellent for large-sized anions, the co-precipitation method remains a critical choice because during the co-precipitation process several synthesis parameters can be controlled independently such as the temperature, the reaction medium pH, the metallic salts condition, the concentration of alkali solution and anion species etc [97].

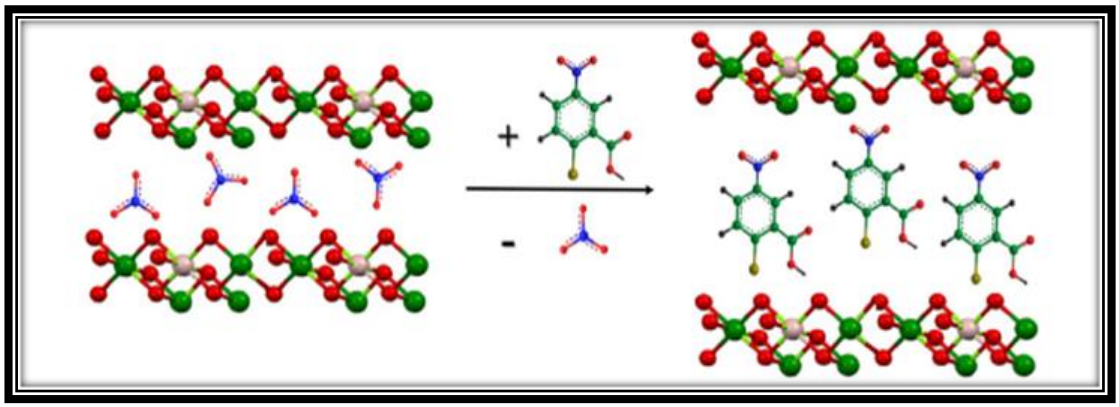

Figure 2.14: Schematic representation of ion-exchange technique [97].

2.3. References

[1] H. Becker, “Low voltage electrolytic capacitor”, ***U.S. Patent*** **(1957)** 2800616.

[2] R.A. Rightmire, “Electrical energy storage apparatus”,***U.S. Patent*** **(1966)** 3288641.

[3] H. Helmholtz, ***Annalen der Physik und Chemie***, 243 **(1879)** 337.

[4] A. Burke, R&D considerations for the performance and application of electrochemical capacitors, ***Electrochimica. Acta.***, 53, **(2007)** 1083.

[5] Bello Abdulhakeem, Thesis (PhD.), ***University of Pretoria*** (**2014**).

[6] G. Gouy, Sur la constitution de la charge électrique à la surface d’un électrolytes, ***J. Phys.,*** 9 (**1910**) 457.

[7] D.L. Chapman *et al*., A contribution to the theory of electrocapillarity, ***Mag. J. Sci***., 25 (**1913**) 475.

[8] Brian Kihun Kim *et al*., Electrochemical Supercapacitors for Energy Storage and Conversion, ***Handbook of Clean Energy Systems*** (**2015**). DOI: 10.1002/9781118991978.hces112.

[9] G. Wang *et al*., A review of electrode materials for electrochemical supercapacitors,***Chem. Soc. Rev***. 41 (**2012**) 797.

[10] J.P. Zheng *et al*., The Limitations of Energy Density for Electrochemical Capacitors,***J. Electrochem. Soc***. 144 (**1997**) 2026.

[11] Y.M. Vol’fkovich, Electrochemical capacitors, ***Russ. J. Electrochem***. 38 (**2002**) 935.

[12]B.E. Conway, Electrochemical Supercapacitors: Scientific Fundamentals and TechnologicalApplications, ***Kluwer*** **(1999)**.

[13] Xi-Lin Wu *et al*., Carbonaceous hydrogels and aerogels for Supercapacitors, ***J. Mater.Chem.,*** A, 2 **(2014)** 4852.

[14] S. Trasatti *et al*., Ruthenium Dioxide : A New Interesting Electrode Material. Solid State Structure and Electrochemical Behavior. ***J. Electroanal.Chem***. ***Interfacial Electro. Chem.,*** 29 **(1971)** A1-A5.

[15] Teng Wang, Thesis (PhD.), ***Queensland University of Technology*** **(2018)**.

[16] V. Augustyn *et al*.,Pseudocapacitive Oxide Materials for High-Rate Electrochamical Energy Storage. ***Energ. Environ. Sci.,*** 7 **(2014)** 1597.

[17] Jinhui Wang *et al*., Recent Progress in Micro-Supercapacitor Design, Integration, and Functionalization, ***Adv. Sciences***. ***News Small Methods*** **(2018)** 1800367.

[18] X. Lu *et al*., Flexible solid-state supercapacitors: design, fabrication and applications, ***Energ. Environ. Sci.,*** 7 **(2014)** 2160.

[19] M. Beidaghi *et al.*, Capacitive energy storage in micro-scale devices: recent advances in design and fabrication of micro-supercapacitors***, Energ.Environ. Sci.,*** 7 **(2014)** 867.

[20] D. P. Dubal *et al*., Towards flexible solid-state supercapacitors for smart and wearable electronics***, Chem. Soc. Rev.*** 47 **(2018)** 2065.

[21] P. Zhang *et al*., Two-dimensional materials for miniaturized energy storage devices: from individual devices to smart integrated systems, ***Chem. Soc. Rev.***, 47 **(2018)** 7426.

[22] Y. Liu *et al*., Nature-Inspired Structural Materials for Flexible Electronic Devices, ***Chem. Rev***.,117 **(2017)** 12893.

[23] J. Zhang *et al*., On the Configuration of SuprecapacitorsforMaximizing Electrochemical Performance. ***Chem. SuS. Chem.,*** 5 **(2012)** 818.

[24] L.L. Zhang *et al*., Carbon-based Materials as Supercapacitor Electrodes. ***Chem. Soc. Rev***., 38 **(2009)** 2520.

[25] Jérémy COME, Thèse de doctorat, ***l'Université Toulouse III– Paul Sabatier*** **(2012).**

[26] R. Kötz *et al*., Principles and applications of electrochemical capacitors***, Electro. chimica. Acta***., 45 **(2000)** 2483.

[27] C. Ramirez-Castro *et al*., On the Development of Activated carbons with high affinity for high voltage propylene carbonate based Electrolytes. ***J. Power sources,*** 270 **(2014)** 379.

[28] J.M. Griffin *et al*., In Situ NMR and Electrochemical Quartz Crystal Microbalance Techniques Reveal the structure of the Electrical Double Layer in Supercapacitors. ***Nat.Mater.,*** 14 **(2015)** 812.

[29] M.D.Stoller *et al*., Graphene-Based Ultracapacitors, ***Nano Lett.,*** 8 **(2008)** 3498.

[30] Y. Zhu *et al*., Carbon-based Supercapacitorsproduced by activation of Graphene. ***Science,*** 332 **(2011)** 1537.

[31] J. Chmiola *et al*., Monolithic Carbine-Derrived Carbon Films for Micro-Supercapacitors. ***Science.,*** 328 **(2010)** 480.

[32] J. Chmiola *et al*., Anomalous Increase in Carbon Capacitance at Pore Sizes Less than 1 nanometer. ***Science.,*** 313 **(2006)** 1760.

[33] K.L. Van Aken *et al*., Formulation of Ionic-Liquid Electrolyte to Expand the Voltage Window of Supercapacitors. Angew. ***Chem. Int.Ed.,*** 54 **(2015)** 4806.

[34] C.Liu *et al*., Graphene-Based Supecapacitor with an Ultrahigh Energy Density. ***Nano. Lett.,*** 10 **(2010)** 4863.

[35] W.Y. Tsai *et al*., Outstanding Performance of Activated Graphene Based Supercapacitors in Ionic Liquid Electrolyte from – 50 to 80°C. ***Nano energy,*** 2 **(2013)** 403.

[36] S. Sathyamoorthi *et al*., Organo-Redox shuttle Promoted Protic Ionic Liquid Electrolyte for Supercapacitors. ***J. Power Sources,*** 274 **(2015)** 1135.

[37] Y.Z. Zhang *et al*., Flexible Supercapacitors based on Paper Substrates: A New paradigm for Low-Cost Energy Storage. ***Chem. Soc. Rev.,*** 44 **(2015)** 5181.

[38] M.M. Hantel *et al.*, Investigation of Diluted Ionic liquid 1-ethyl-3- methyl-inidazolium Tetrafluoroborate Electrolytes for Intercalation-like Electrodes Used in supercapacitors. ***Electro. chim. Acta.,*** 110 **(2013)** 243.

[39] X.Lu *et al.*, Flexible Solid-state Supercapacitors: Design, Fabrication and Application. ***Energ. Environ. Sci.,*** 7 **(2014)** 2160.

[40] Y. Huang *et al*., Magnetic-Assisted, self-Healable, Yarn-Based supercapacitors. ***ACS. Nano.,*** 9 **(2015)** 6242.

[41] C. Zhu *et al.*, All Metal-Nitrides Solid-State Asymmetric Supercapacitors. ***Adv. Mater.,*** 27 **(2015)** 4566.

[42] X. Lu *et al*., Flexible solid-state supercapacitors: design, fabrication and applications**,** ***Sci.,*** 7 **(2014)** 2160.

[43] P. Simon *et al*., Materials for electrochemical capacitors, ***Nature Materials***, 7 **(2008)** 845.

[44] A.G. Pandolfo *et al*., Carbon properties and their role in supercapacitors**,** ***Journal of Power Sources***, 157 **(2006)** 11.

[45] E. Frackowiak *et al.*, Carbon Materials for the Electrochemical Storage of Energy in Capacitors**,** ***Carbon***, 39 **(2001)** 937.

[46] M. Inagaki *et al*., Carbon materials for electrochemical capacitors**,** ***Journal of Power Sources***, 195 **(2010)** 7880.

[47] M. Ishikawa *et al*., Effect of treatment of activated carbon fiber cloth electrodes with cold plasma upon performance of electric double-layer capacitors, ***Journal of Power Sources***, 60 **(1996)** 233.

[48] A. Krause *et al*., Electrochemical double layer capacitor and lithium-ion capacitor based on carbon black**,** ***Journal of Power Sources***, 196 **(2011)** 8836.

[49] J. Chmiola *et al*., Double-Layer Capacitance of Carbide Derived Carbons in Sulfuric Acid**,** ***Electrochemical and Solid State Letters***, 8 **(2005)** A357.

[50] J. Gamby *et al*., Studies and characterisations of various activated carbons used for carbon/carbon supercapacitors, ***Journal of Power Sources***, 101 **(2001)** 109.

[51] A. Burke, Ultracapacitors: why, how, and where is the technology***, Journal of Power Sources***, 91**(2000)** 37.

[52] O. Barbieri *et al*., Capacitance limits of high surface area activated carbons for double layer capacitors***, Carbon***, 43 **(2005)** 1303.

[53] H. Shi, ***Electro.*** Activated carbons and double layer capacitance***, Chimica. Acta.***, 41 **(1996)** 1633.

[54] A. Rudge *et al*., A study of the electrochemical properties of conducting polymers for application in electrochemical capacitors***, Electro. Chimica. Acta.,*** 39 **(1994)** 273.

[55] H.Y. Lee *et al*., Supercapacitor Behavior With KCl Electrolyte, ***J. Solid. State Chem.,*** 144 **(1999)** 220.

[56] J.P. Zheng *et al*., Hydrous Ruthenium Oxide as an Electrode Material for Electrochemical Capacitors. ***J. Electro. Chem.Soc***.,142 **(1995)** 2699.

[57] M. Toupin *et al*., Charges Storage Mechanism of MnO2 Electrode Used in Aqueous Electrochemical Capacitor. ***Chem. Mater.,*** 16 **(2004)** 3184.

[58] Y. Zhang, *et al*., Crystallization Design of MnO_2 towards Better supercapacitors. ***Cryst. Eng. Comm.,*** 14 **(2012)** 5892.

[59] D. Chen, *et al*., Probing the charge Storage Mechanism of a Pseudocapacitive MnO2 Electrode using in Operando Raman Spectroscopy. ***Chem. Mater.,*** 27 **(2015)** 6608.

[60] M. Yeager *et al*., Highly Efficient K0.15 MnO_2 Birnessite Nanosheets for stable Pseudocapacitive Cathodes. ***J. Phys. Chem. C***. 116 **(2012)** 20173.

[61] W. Wei *et al*., Manganese Oxide-Based Materials as Electrochemical Supercapacitor Electrodes. ***Chem. Soc. Rev.,*** 40 **(2011)** 1697.

[62] Y. Hu *et al*., Flexible Asymmetric Supercapacitor Based on Structure-Optimized Mn_3O_4/Reduced Graphene Oxide Nanohybrid Paper with High Energy and Power Density. ***Adv. Funct. Mater***., 25 **(2015)** 7291.

[63] L. Wang *et al*., Preparation of Fe_3O_4 with High Specific Surface Area and Improved Capacitance as a Supercapacitor. ***Nanoscale,*** 5 **(2013)** 3793.

[64] Z. Lin *et al*., Adjusting Electrode Initial Potential to Obtain High-Performance Asymmetric Supercapacitor based on Porous Vanadium Pentoxide Nanotubes and Activated Carbon Nanorods. ***J. Power Sources,*** 279 **(2015)** 358.

[65] Y. Liu *et al*., Hierarchical SnO_2 Nanostrucures Made of Intermingled Ultrathin Nanosheets for Environmental Remediation, Smart Gas Sensor, and Supercapacitor Applications. ***ACS. Appl. Mater. Interfaces,*** 6 **(2014)** 2174.

[66] S. Wu *et al*., Distinctive Supercapacitive Properties of Copper and Copper Oxide Nanocrystals Sharing a Similar Colloidal Synthetic Route. ***Adv. Energy Mater.*, (2017)** 1700105.

[67] L. Chen *et al*., Copper Salts Mediated Morphological Transformation of Cu_2O from Cubes to Hierarchical Flower-like or Microspheres andtheir Supercapacitors Performances. ***Sci. Rep*.,** 5 **(2015)** 9672.

[68] T. Brezesinski *et al*., Ordered Mesoporous Alpha-MoO_3 with Iso-Oriented Nanocrystalline Walls for Thin-Film Pseudocapacitors. ***Nat. Mater*.,** 9 **(2010)** 146.

[69] X. Geng *et al*., Two-Dimensional Water-Coupled Metallic MoS_2 with Nano channels for Ultrafast Supercapacitors. ***Nano Lett*.,** 17 **(2017)** 1825.

[70] S. Ozkan *et al*., Highly Conducting Spaced TiO_2 Nanotubes Enable Defined Conformal Coating with Nanocrystalline Nb_2O_5 and High Performance Supercapacitor Applications. ***Small,*** 13 **(2017)** 1603821.

[71] C. Wang *et al*., Carbon-Modified $Na_2Ti_3O_7.2H_2O$ Nanobelts as redox Active Materials for High-Performance Supercapacitor. ***Nano Energy,*** 28 **(2016)** 115.

[72] Z. Chen *et al*., Hierarchical Nanostructured WO3 with Biomimetic proton Channels and Mixed Ionic-Electronic Conductivity for Electrochemical Energy Storage. ***Nano Lett*.,** 15 **(2015)** 6802..

[73] F.L. Zheng *et al*., Synthesis of Hierarchical Rippled Bi_2O_3nanobelts for Supercapacitor Applications. ***Chem.Commun*.,** 46 **(2010)** 5021.

[74] R. Li *et al*., Large Scale Synthesis of NiCo Layered Double Hydroxides for Superior Asymmetric Electrochemical Capacitor. ***Sci. Rep*.,** 6 **(2016)** 18737, doi: 10.1038/srep18737.

[75] K.C. Liu, Porous Nickel Oxide/Nickel Films for Electrochemical Capacitors. ***J. Electro. Chem. Soc*.,** 143 **(1996)** 124.

[76] C. Lin, *et al*., Characterization of Sol-Gel-Derived Cobalt Oxide Xerogels as Electrochemical Capacitors. ***J. Electro. Chem. Soc*.,** 145 **(1998)** 4097.

[77] X. Ren *et al*., Facile Synthesis of Hierarchical Mesoporous Honeycomb-like Nio for Aqueous Asymmetric Supercapacitors. ***ACS. Appl.Mater. Interfaces,*** 7 **(2015)** 19930.

[78] T. Zhai *et al*., Phosphate Ion Functionalized Co_3O_4 Ultrathin Nanosheets with Greatly Improved Surface Reactivity for High Performance Pseudocapacitors. ***Adv. Mater*.,** 29 **(2017)** 104167.

[79] S.D. Perera *et al.*, Enhanced Supercapacitor Performance for Equal Co-Mn Stoichiomettry in Colloidal Co3-xMnxO4 Nanoparticles, in Additive-Free Electrodes. ***Chem.Mater.,*** 27 **(2015)** 7861.

[80] C. Yuan *et al.*, Growth of Ultrathin Mesoporous Co_3O_4Nanosheet Arrays on Ni Foam for High-Performance Electrochemical Capacitors. ***Energ. Environ. Sci.,*** 5 **(2012)** 7883.

[81] M. Xie *et al.*, In-Situ-Grown $Mg(OH)_2$-Derived Hybrid α-$Ni(OH)_2$ for Highly Stable Supercapacitor. ***ACS.Energy Lett.,*** 1 **(2016)** 814.

[82] L. Wang *et al.*, Phase Transformation Guided Single-Layer Beta-$Co(OH)_2$ Nanosheets for Pseudocapacitive Electrodes. ***ACS. Nano.,*** 8 **(2014)** 3724.

[83] H. Pang, One-Pot Synthesis of Heterogeneous Co_3O_4-nanocube/$Co(OH)_2$-Nanosheet Hybrids for High-Performance Flexible Asymmetric All-Solid-State Supercapacitors. ***Nano Energy,*** 35 **(2017)** 138.

[84] C. Zhang *et al.*, High-Energy All-Solid-State Symmetric Supercapacitor Based on Ni_3S_2 Mesoporous Nanosheet-Decorated Three-Dimensional Reduced Graphene Oxide. ***ACS Energy Lett.,*** 2 **(2017)** 759.

[85] B. You *et al.*, Hierarchically Porous Nickel Sulfide Multifunctional Superstructures. ***Adv. Energy Mater.,*** 6 **(2016)** 1502333.

[86] T. Wang *et al.*, Electro-Deposition of $CoNi_2S_4$ Flower-Like Nanosheets on 3D Hierarchically Porous Nickel Skeletons with High Electrochemical Capacitive Performance. ***J. Mater. Chem.,*** A 3 **(2015)** 2303523041.

[87] C. Tang *et al.*, In Situ Growth of NiSe Nanowire Film on Nickel Foam as an Electrode for High-Performance Supercapacitors. ***Chem. Electro. Chem.,*** 2 **(2015)** 1903.

[88] Z. Zhang *et al.*, Synthesis of Core-Shell NiSe/C Nanospheres as Anodes for Lithium and Sodium Storage. ***Electro. Chim. Acta.,*** 208 **(2016)** 238.

[89] W. An *et al.*, Ni0.9Co1.92Se4 Nanostructures: Binder-Free Electrode of Coral-like Bimetallic Selenide for Supercapacitors. ***RSC Adv.,*** 6 **(2016)** 75251.

[90] K. Zhou *et al.*, Ultrahigh-Performance Pseudocapacitor Electrodes Based on Transition Metal Phosphide Nanosheets Array via Phosphorization: A General and Effective Approach, ***Adv. Funct. Mater.,*** 25 **(2015)** 7530.

[91] M. Kong *et al.*, NiCoP Nanoarray: A superior Pseudocapacitor Electrode with High Areal Capacitance. ***Chem. Eur. J.,*** 23 **(2017)** 4435.

[92] Z. Zhang et al., Fiber-Based Multifunctional Nickel Phosphide Electrodes for Flexible Energy Conversion and Storage. ***J. Mater. Chem.,*** A4 **(2016)** 9691.

[93] Y. Xi *et al*., Well-Defined, Nanostructured, Amorphous Metal Phosphate as Electrochemical Pseudocapacitor Materials with High Capacitance. ***Chem. Mater.,*** 28 **(2016)** 1355.

[94] J. Zhao *et al*., Hydrothermal Synthesis of Nickel Phosphate Nanorods for High-Performance Flexible Asymmetric All-Solid-State Supercapacitors. ***Part. Part. Syst. Char.,*** 32 **(2015)** 880.

[95] S. Wang *et al*., $NH_4CoPO_4.H_2O$ Microbundles Consisting of One-Dimensional Layered Microrods for High Performance Supercapacitors. ***RSC Adv.***, 4 **(2014)** 340.

[96] X. Long *et al*., Transition Metal Based Layered Double Hydroxides Tailored for Energy Conversion and Storage. ***Mater. Today.,*** 19 **(2016)** 213.

[97] G. Mishra *et al*. Layered Double Hydroxides: A brief review from fundamentals to application as evolving biomaterials, ***Applied Clay Science,*** 153 **(2018)** 172.

[98] V. Rives, Layered Double Hydroxides: Present and Future. ***Nova Science Publishers*** (**2001**) New York, NY, USA.

[99] Teng Wang *et al*., 2-methylimidazole-derived Ni-Co Layered Double Hydroxide Nanosheets as High Rate Capability and High Energy Density Storage Material in Hybrid Supercapacitors. ***ACS Appl. Mater. Interfaces*** (**2017**) DOI: 10.1021/acsami.7b02987.

[100] T. Brousse *et al*., To Be or Not to Be Pseudocapacitive? ***J. Electrochem. Soc.,*** 162 (**2015**) A5185.

[101] Y. Wang *et al*., Electrochemical Capacitors: Mechanism, Materials, Systems, Characterization and Applications. ***Chem. Soc. Rev***. 45 (**2016**) 5925.

[102] Yinyin Lin *et al*., Understanding the enhancement of electrochemical properties of NiCo Layered Double Hydroxides via functional pillared effect: An insight into dual charge storage mechanisms; ***Electro. Chimica. Acta.*** 246 **(2017)** 406.

[103] V. Rives, Characterisation of layered double hydroxides and their decomposition products, ***Materials Chemistry and Physics*** 75 (**2002**) 19.

[104] K.A. Carrado *et al*., Layered double hydroxides (LDHs), ***Solid State Ionics*** 26 (**1988**) 77.

[105] H.F.W. Taylor *et al*., Crystal structure of some double hydroxide minerals, ***Mag***. 39 (**1973**) 377.

[106] M. Richetta *et al*., Layered Double Hydroxides: Tailoring Interlamellar Nanospace fora Vast Field of Applications. ***J. Material. Sci. Eng.,*** 6 (**2017**) 360. Doi: 10.4172/2169-0022.1000360.

[107] E. Manasse, Rocceeritree e di adendellacollezioneissel, Atti. Soc. Toscana Sc. ***Nat., Proc.Verb***. 24 (**1915**): 9.

[108] R. Allmann *et al*, The crystal structure of pyroaurite. *Acta Crystallogr*. Sect. B: Struct. Crystallogr. ***Cryst. Chem.,*** 24, **(1968)** 972.

[109] H.F.W. Taylor, Segregation and cation-ordering in Sjögrenite and Pyroaurite. ***Mineral. Mag.*** 37 **(1969)** 338.

[110] Afriyanti Sumboja *et al*., NiMn Layered Double Hydroxides as efficient electrocatalysts for the oxygen evolution reaction and their application in rechargeable Zn–air batteries, ***The Royal Society of Chemistry, Nanoscale***, 9 **(2017)** 774.

[111] Feifei Wang *et al.,* One-step synthesis of Nickel Iron Layered Double Hydroxide/reduced graphene oxide/carbon nanofibres composite as electrode materials for asymmetric supercapacitor, 8 **(2018)** 8908. DOI:10.1038/s41598-018-27171-0.

[112] J. He *et al*., Preparation of Double Layered Hydroxides. In: Duan, X., Evans, D.G. (Eds.), Layered Double Hydroxides. ***Springer, Berlin*** **(2006)**.

[113] A.I. Khan *et al*., Intercalation chemistry of layered double hydroxides: recent developments and applications. ***J. Mater. Chem.*** 12 (**2002**) 3191.

[114] D.G. Evans *et al*., Layered double hydroxides. In: Structure and Bonding. Vol.119. ***Springer Berlin*** (**2006**).

[115] A. Vaccari, In: Rives, V. (Ed.), Layered double hydroxides: present and future. ***Nova Science Publishers***, Inc., New York, ISBN 1-59033-060-9. ***Appl.Clay Sci***. 22 (**2001**) 75.

[116] L. Mohapatra *et al*., A review on the recent progress, challenges and perspective of layered double hydroxides as promising photocatalysts. ***J. Mater. Chem.*** A 4 (**2016**) 10744.

[117] M. Shao *et al*., The synthesis of hierarchical Zn-Ti layered double hydroxide for efficient visible-light photocatalysis. ***Chem. Eng. J.*** 168 (**2011**) 519.

[118] C. Forano *et al.*, Layered double hydroxides (LDH), in: Bergaya, F., Lagaly, G. (Eds.), ***Handbook of Clay Science***, 2nd edition. Part A: Fundamentals, ***Developments in Clay Science***, (**2013**) vol. 5. Elsevier, Amsterdam, pp. 745.

[119] F. Barahuie *et al*., Synthesis of protocatechuic acid–zinc/aluminium–layered double hydroxide nano composite as an anticancer nanodelivery system. ***J. Solid State Chem.*** 221 (**2015**) 21.

[120] N. Morel-Desrosiers *et al*., Intercalation of Dicarboxylate anions into a Zn−Al−Cl layered double hydroxide: microcalorimetric determination of the enthalpies of anion exchange. ***J. Mater. Chem.*** 13 (**2003**) 2582.

[121] J. Das *et al*., Heteropoly acid intercalated Zn/Al HTlc as efficient catalyst for esterification of acetic acid with n-butanol. ***J. Mol. Catal. A Chem.*** 264 (**2007**) 248.

Chapter 3. Sample Preparation and Characterization Techniques

3.1. Introduction

The experimental procedure used in this study to synthesize and characterize NiCo-LDH is presented and discussed in this chapter. Also, the electrochemical test to evaluate the properties of NiCo-LDH for supercapacitor applications is presented in detail.

3.1.1. Sample preparation

The co-precipitation method is one of the most usually applied techniques for direct synthesis of layered double hydroxides (LDH) as discussed above in detail in **chapter 2**. It is entirely based on the condensation of hexa-aqua metal complexes in solution, allowing the brucite-like layers to be formed with a uniform distribution of metallic cation with solvated interlamellar anions. Moreover, it can also be applied for large-scale synthesis of materials [1-3].

Herein, the NiCo-LDH was prepared via co-precipitation method. All chemicals were used as delivered by Sigma-Aldrich and no further purification was conducted. 10.016 mM of $Ni(NO_3)_2 \bullet 6H_2O$ and 20.006 mM of $Co(NO_3)_2 \bullet 6H_2O$ were dispersed into a solution containing a mixture of 152 ml of $(CH_2OH)_2$ and 60 ml of deionized water under vigorous stirring for about 8 minutes at room temperature. Thereafter, 148.004 mM of Urea was added into the main solution and kept under vigorous stirring for a further 12 minutes. The obtained solution was finally heated for 3 hours at 90°C until the precipitates were formed. The obtained precipitates were filtered using a filter paper having an appropriate pore dimension and washed in a mixture of deionized water and ethanol several times and finally dried at 80°C overnight. The as-obtained product was named NiCo-LDH@80°C having (Ni:Co=1/2) as an atomic ratio. **Figure 3.1** displays a schematic diagram showing the synthesis of NiCo-LDH@80°C.

Figure 3.1: Schematic diagram showing thesynthesisof NiCo-LDH@80°C.

3.2. Characterization techniques

3.2.1. X-rays Diffraction (XRD)

The X-rays Diffraction (XRD) is an effective analytical technique that preserves material properties integrity during the measurements. It is used to characterize the structural fingerprint of a solid-state material to identify phase formation from the diffraction patterns analysis [4].

The aligned beam of x-rays irradiates the compound under study to generate diffraction patterns as a function of the diffraction angle. Thus, Bragg's law can be used to elucidate the interference pattern of X-rays dispersed by crystals. **Equation 3.1** represents the mathematical fundamental description of the XRD process. The intensity of the diffracted x-rays is calculated as a function of a diffraction angle (2θ) and the representative orientation. **Figure 3.2** displayed the schematic principle of XRD through Bragg's law.

In this study, the structural analysis was carried out using the Rigaku Smartlab X-ray diffractometer having CuKα (λ= 1.5418Å) radiation.

$$n\lambda = 2\,d\sin\theta \qquad (3.1)$$

where:

- ❖ n : is diffraction series
- ❖ θ : is diffraction angle,
- ❖ λ : is the wavelength of X-ray,
- ❖ d : is interplanar distance. However, d is the lattice constant, in case of a single crystal.

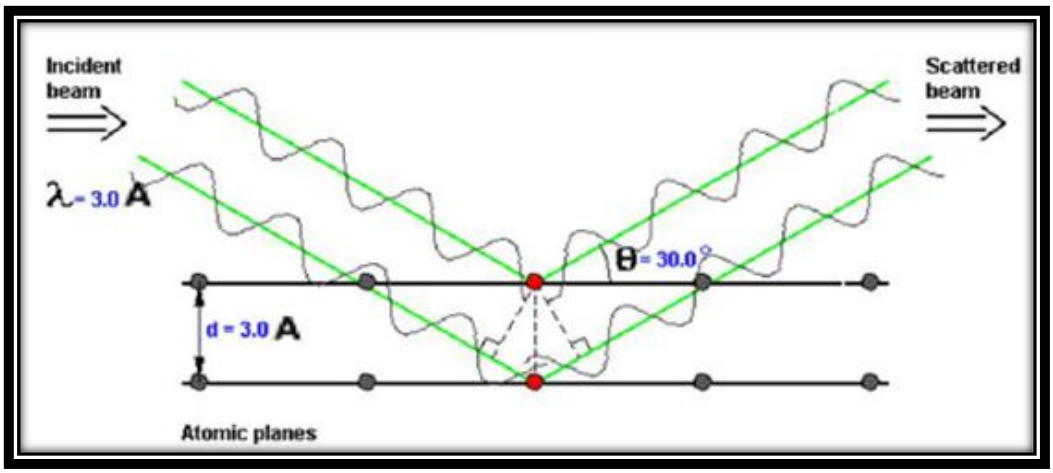

Figure 3.2: Principle of XRD based on bragg's law [5].

3.2.2. Scanning Electron Microscopy (SEM)

Scanning electron microscopy (SEM) is a powerful electron microscope instrument that provides images of material by scanning its surface. In principle, an electron column generates a beam of incident electrons that strike the targeted sample. A given electron will interact with atoms in the material, generating several signals containing information related to the precise description of the surface morphology of the material. The thermal emission source (heated tungsten filament) or the field emission cathode is the commonly used sources that produce electrons. The electrons are focused into a small beam through a group of electromagnetic lenses in the SEM column. Depending on the study's objectives, the energy of the incident electrons can be varied from 100 eV or 30 keV [6].

In this research, the SEM images were captured using the JEOL JSM-7800F FE-SEM. The elemental composition was captured using the energy-dispersive x-ray spectroscopy (EDS) from thermos Fisher scientific, which was coupled to the SEM.

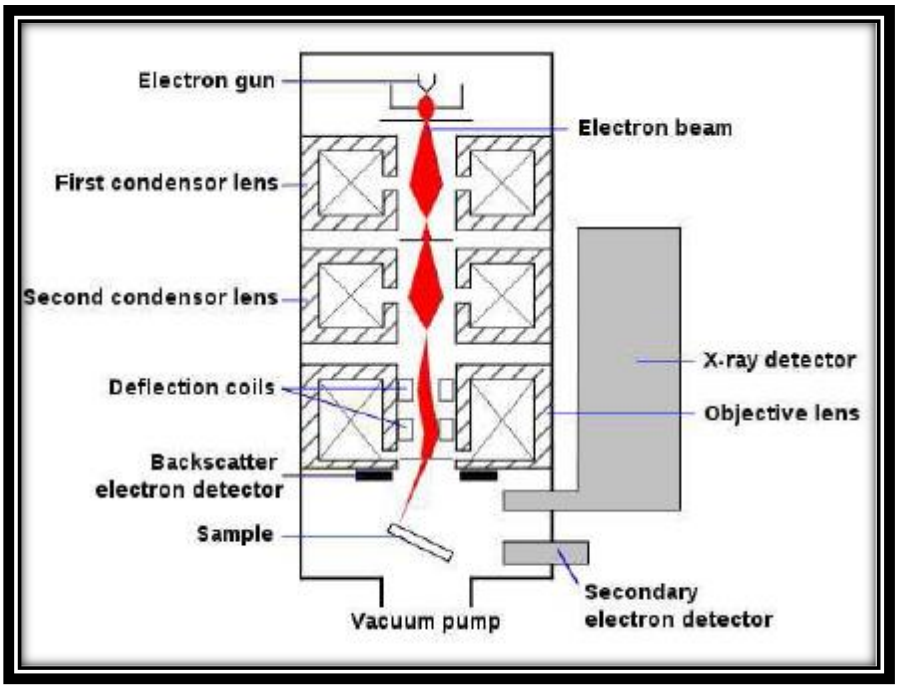

Figure 3.3: Schematic diagram of the SEM [7].

3.2.3. Fourier-Transform Infrared Spectroscopy

The Fourier-Transform Infrared spectroscopy (FTIR) is a non-destructive analytical technique used for the identification of functional groups present in a sample. The goal is to expose a sample to infrared radiations (IR) to obtain a transmittance spectrum when a part of IR passes through the sample. The absorbance spectrum is derived from part of absorbed IR [8].Moreover, the FTIR is a useful technique especially in the study of LDH, because it has the ability to deliver the identity related to the interlayer ions present in the LDH materials [9].In this research, the FTIR spectrum was collected using IR Tracer-100-SHIMADZU.

3.2.4. X-ray Photoelectron Spectroscopy

The X-ray photoelectron spectroscopy (XPS) is a remarkably puissant and useful surface technique that provides information related to the chemical states on the surface of a given material. In principle, the photoelectric effect which describes the foundation of the XPS technique has been described by Einstein in 1905, where the photon concept was used to explain how electrons were ejected from the surface when photons collide onto it [5]. Thus, the monochromatized X-rays investigate the sample by ejecting a photoelectron from an atom's K level under a vacuum. The photo-emitted electrons' energy is related to the chemical state of the elements present within the sample. Finally, photoelectrons are recorded and examined to generate a spectrum that indicates the binding energy of each element present on the surface of the sample [5].

In this study, XPS measurements were performed using a KRATOS-SUPRA spectrometer using monochromatic AlKα radiation with hν=1486.6 eV at a base pressure of $1.2*10^{-8}$Torr.

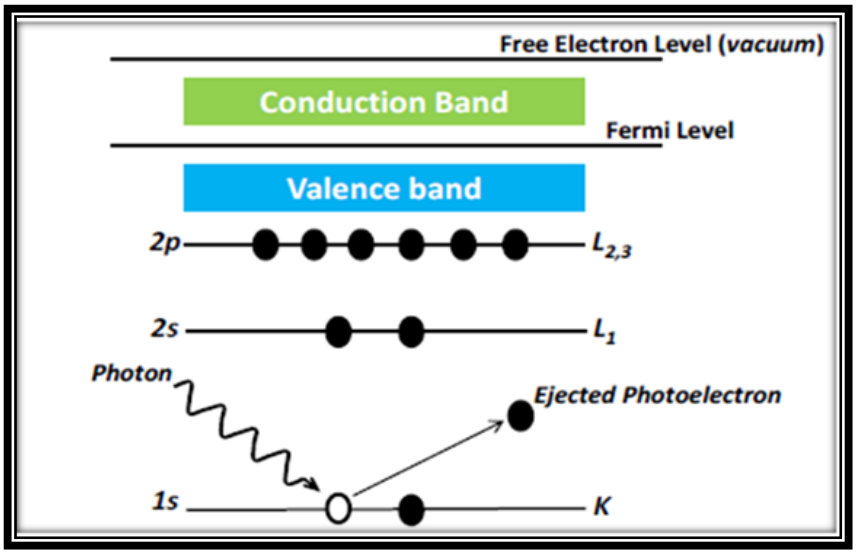

Figure 3.4: XPS emission process [5].

3.3. Electrochemical Analysis

In this study, the electrochemical tests were carried out using an AUTOLAB PGSTAT302N electrochemical station with NOVA 2.1 software.

The measurements were performed using a three-electrode configuration, consisting of glassy carbon as a working electrode, platinum wire, and Ag/AgCl (3 M KCl-filled), as counter and reference electrodes respectively. The sodium sulfate and potassium hydroxides were used as electrolytes with a concentration of 1.0 M. Finally, cyclic voltammetry and electrochemical impedance spectroscopy data were collected and analyzed in detail.

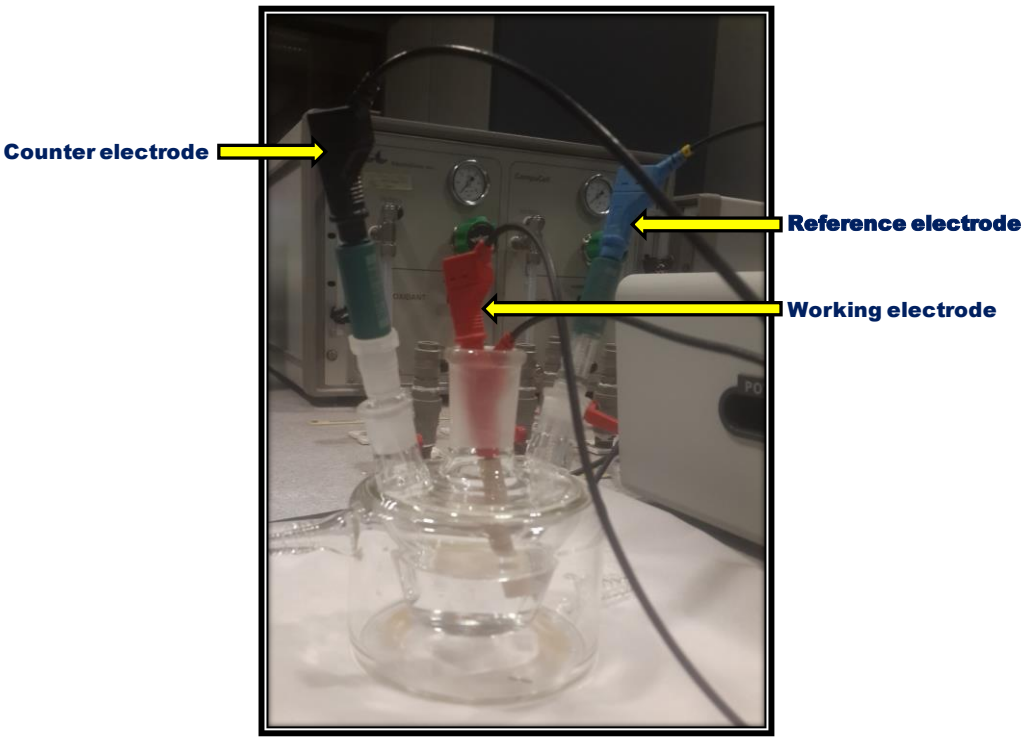

Figure 3.5: Three-electrode configuration used in this study.

3.3.1. Electrode preparation

The glassy carbon GC50 with a disk diameter of 5 mm was used as a working electrode. The active area of glassy carbon was cleaned by polishing it using alumina powder and emery paper until it looked like a mirror. The alumina fine powder and emery paper were used for that purpose. Finally, it was washed with deionized water and acetone [10]. The slurry was prepared by dispersing a mixture of active material (NiCo-LDH@80°C), carbon black and polyvinylidene fluoride (PVDF) with a weight ratio of (80:10:10) in N-methyl pyrrolidone (NMP). Thereafter, the mixture was sonicated for 10 min and 100 µL of the obtained slurry was drop-casted over the active area and dried at room temperature for 24 hours.

Figure 3.6: Working electrode used in this study.

3.3.2. Cyclic Voltammetry

Cyclic voltammetry (CV) is the most useful electrochemical technique which is able to provide the kinetics and thermodynamics information related to the redox reactions within a system. Moreover, it also enables to investigate thoroughly diverse analyte characteristics, for example: the diffusion, the number of electrons carried over in charge transfer reaction and the adsorption [11, 12].

During the cyclic voltammetry (CV) test, the potential is applied and the current is measured. Therefore, the CV curve represents a function of the measured current versus the applied potential. **Figure 3.7** illustrates the very commonly investigated CV curves.

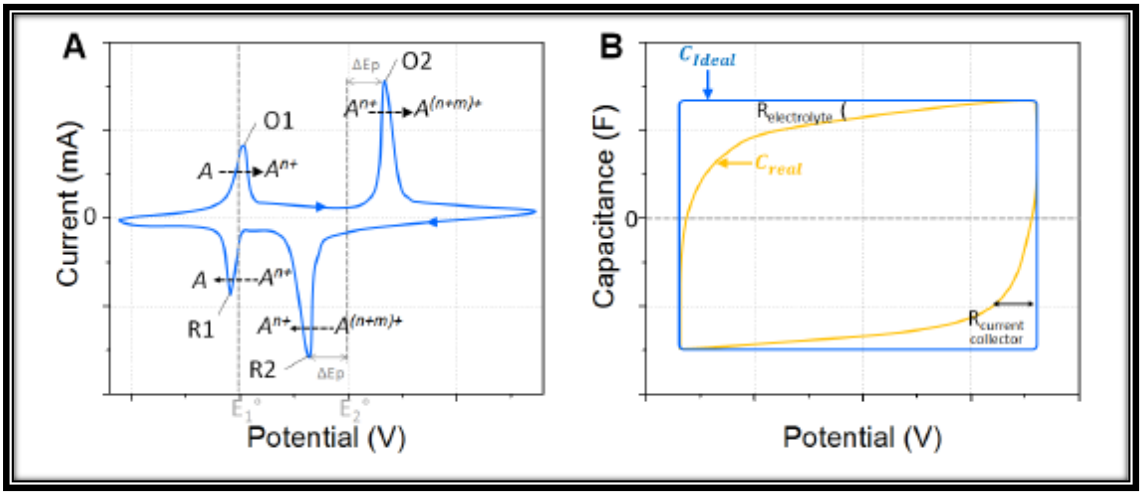

Figure 3.7: (A) Typical cyclic voltammograms of redox, (B) Cyclic voltammograms of double layer materials [13].

Previous studies have demonstrated that the charge storage capacity and the specific capacitance of a supercapacitor electrode could be calculated using the cyclic voltammetric (CV) curves through **equation 3.2** [14-16].

$$\boldsymbol{Csp} = \frac{\text{Voltammetric charge}}{(\text{potential window X active material mass loading})} \qquad (\mathbf{3.2})$$

Wei Chen *et al*. [14], have made further clarification by reporting that in case where the shape of cyclic voltammetric (CV) curves are not the ideal mirror-symmetry, which means the anodic voltammetric charges (q_a) and cathodic voltammetric charges (q_c) are not comparable, the total voltammetric charges can be calculated by integrating the positive and negative sweep in cyclic voltammograms.Thus, **equation 3.3** can now be applied to calculate the specific capacitance of a given supercapacitor [17-19].

$$C_{sp} = \frac{\int_{E_1}^{E_2} \boldsymbol{i(E)dE}}{\boldsymbol{2(E_2 - E_1)\, mV}} \quad (3.3)$$

where:

- ***Csp*** : is the specific capacitance (**Fg^{-1}**),
- $\int_{E1}^{E2} \boldsymbol{i(E)dE}$: is the total voltammetric charges which is the result of the integration of positive and negative sweep in cyclic voltammograms.
- **(E_2-E_1)** : is the potential window (**V**),
- **m** : is the mass of electrode after deposition of slurry (**gr**),
- **V** : is the potential scan rate (**V/s**).

3.3.3. Electrochemical Impedance Spectroscopy

The electrochemical impedance spectroscopy (EIS) is a critical investigation technique used to investigate the electrochemical phenomenon at the electrode-electrolyte interface. The EIS data collection consists of the application of a sinusoidal potential by a small amplitude in a wide range of frequencies from 100 kHz to a few MHz to a regular state. **Equation 3.4** analytically describes the EIS principle [13,20].

$$\boldsymbol{E} = E0 + \Delta Esi(\omega t) \quad (\mathbf{3.4})$$

The current response to the applied potential which is a sinusoidal current with a shifted angle of phase φ is described by **equation 3.5.**

$$\boldsymbol{I} = I0 + \Delta \mathrm{Is}(\omega \mathrm{t} + \varphi) \quad (\mathbf{3.5})$$

where

- **E** : is the potential (V),
- **E0** : is the initial regular state potential (V),
- **ΔE** : is the amplitude of the signal (V),
- **ω** : is the pulsation (rad.$^{s-1}$),
- **t** : is the time (s),
- ***I*** : is the current (A),
- **I0** : is the regular state current (A),
- **ΔI** : is the amplitude of the current response (A),
- **φ** : is the phase shift.

In order to simplify the mathematical calculations during the electrochemical impedance spectroscopy measurements, the potential and current are most often written using complex numbers as presented below (see **Equations 3.6** and **3.7)** [13].

$$\Delta E = \Delta \mathbf{E}_{max}\, e(\omega t) \qquad (\mathbf{3.6})$$

$$\Delta I = \Delta \mathbf{I}_{max} e(\omega t + \varphi) \qquad (\mathbf{3.7})$$

The complex impedance is determined by the ratio between the complex potential and complex current [16].

$$Z = \frac{\Delta E}{\Delta I} = \frac{\Delta \mathbf{E}_{max}}{\Delta \mathbf{I}_{max}} e^{-j\,\varphi} \qquad \mathbf{(3.8)}$$

Thus, the Euler's formula can be used as:

$$Z = \frac{\Delta E}{\Delta I} = \frac{\Delta \mathbf{E}_{max}}{\Delta \mathbf{I}_{max}}\, X\, [\cos(\varphi) - j sin(\varphi)] = Re(Z) - jX\, Im(Z) \qquad (\mathbf{3.9})$$

where:

- Re(Z) : is the real part of the impedance
- Im(Z) : is the imaginary part of the impedance.

Generally, the Electrochemical impedance spectroscopy (EIS) data is presented by a curve of –Im(Z) versus Re(Z) which is known as the Nyquist plot (see **Figure 3.8**).

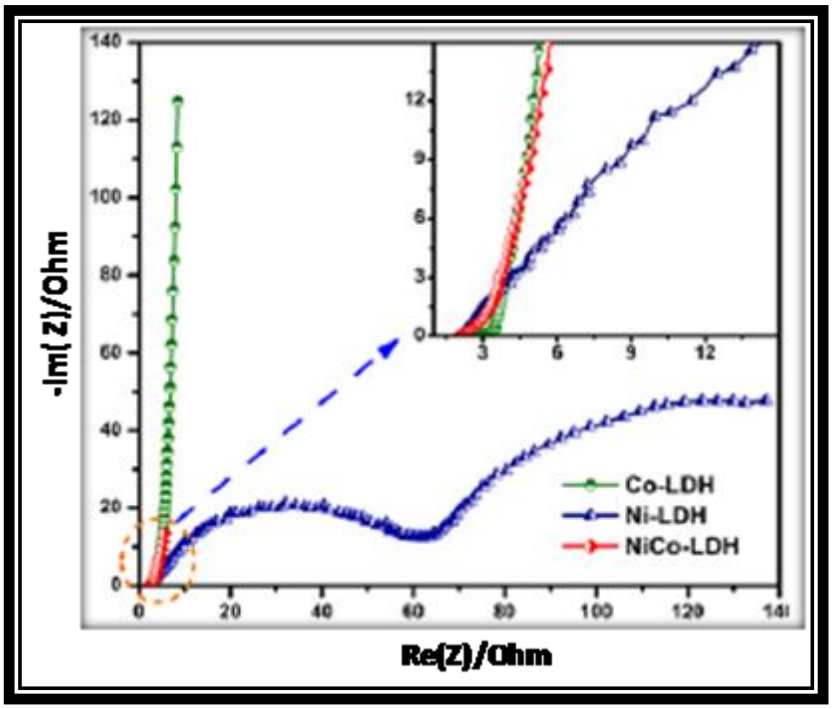

Figure 3.8: EIS Nyquist plot of NiCo-LDH [21].

In this study, the EIS measurements were performed with an AC amplitude of 5 mV in the frequency range of 100 kHz to 100 MHz.

3.4. References

[1] D.G. Evans et al., Layered double hydroxides. In: Structure and Bonding. Vol. 119. ***Springer***, ***Berlin*** (**2006**).

[2] A. Vaccari, In: Rives, V. (Ed.), Layered double hydroxides: present and future. ***Nova Science Publishers***, Inc., New York, ISBN 1-59033-060-9. ***Appl. Clay Sci***. 22 (**2001**) 75.

[3] L. Mohapatra *et al.*, A review on the recent progress, challenges and perspective of layered double hydroxides as promising photocatalysts. ***J. Mater. Chem.*** A 4 (**2016**) 10744.

[4] Ricardo Valdez *et al*., Nanosheets of Co-(Ni and Fe) Layered Double Hydroxides for Electrocatalytic Water Oxidation Reaction, ***Int. J. Electrochem. Sci.***, 10 (**2015**) 909.

[5] Cao Guozhong, Nanostructures and Nanomaterials: Synthesis, Properties & Applications, 6th edition, ***Imperial College Press, London*** (**2004**).

[6] G.L. Kabongo, Dissertation (M.Sc.), ***University of South Africa*** (**2013**).

[7] J.Das *et al*., Heteropoly acid intercalated Zn/Al HTlc as efficient catalyst for esterification of acetic acid with n-butanol. J. Mol. ***Catal. A Chem***., 264 (**2007**) 248.

[8] Sri D Suneel, Industrial Production Engineering: ***special nano materials***, characterization and tools.

[9] Y. Momodu Damilola , Thesis (PhD.), ***University of Pretoria*** (**2015**).

[10] ShimaaGamil *et al*., Nanohybrid layered double hydroxides materials as efficient catalysts for methanol electrooxidation, ***RSC Adv,*** 9 (**2019**) 13503.

[11] Wang, J. Analytical Electrochemistry; John Wiley & Sons: Hoboken, New Jersey, (**2006**).

[12] R. G. Compton *et al.*, Understanding Voltammetry, 2nd Ed., ***Imperial College Press*** (**2011**).

[13] Yohan Dall'Agnese. Study of early transition metal carbides for energy storage applications. Mechanics of materials [physics.class-ph].***Université Paul Sabatier - Toulouse III*** (**2016**).

[14] Wei Chen *et al*., Enhanced capacitance of manganese oxide via confinement inside carbon nanotubes, ***Royal Society of Chemistry*** (**2010**).

[15] Chi-Chang Hu *et al*., Ideal capacitive behavior of hydrous manganese oxide prepared by anodic deposition, ***Electrochemistry Communications*** 4 (**2002**) 105.

[16] B.E. Conway, Electrochemical Supercapacitors: Scientific Fundamentals and Technological Applications, ***Kluwer***, New York (**1999**).

[17] Chen-Ching Wang *et al*., Electrochemical catalytic modification of activated carbon fabrics by ruthenium chloride for supercapacitors, ***Carbon*** 43 (**2005**) 1926.

[18] Kyung-Wan Nama *et al*., Electrodeposited manganese oxides on three-dimensional carbon nanotube substrate: Supercapacitive behaviour in aqueous and organic electrolytes, ***Journal of Power Sources***, 188 (**2009**) 323.

[19] Thanh-Nhan Tran *et al.*, A facile in-situ activation of protonated histidine-derived porous carbon for electrochemical capacitive energy storage, ***Journal of Industrial and Engineering Chemistry,*** 73 (**2019**) 316.

[20] Bello Abdulhakeem, Thesis (PhD.), ***University of Pretoria*** (**2014**).

[21] Teng Wang *et al.*,2-methylimidazole-derived Ni-Co Layered Double Hydroxide Nanosheets as High Rate Capability and High Energy Density Storage Material in Hybrid Supercapacitors, ***ACS Applied Materials & Interfaces 9*** (**2017**) 15510.

Chapter 4. Physico-chemical Properties of NiCo-LDH

4.1. Introduction

Supercapacitor technologies are gaining tremendous momentum and becoming the center of attention of a large number of studies due to their superior capabilities, such as environmental friendliness, high efficiency, fast charge-discharge rates, high power density, safe operation, good cycling stability and lower maintenance cost [1-4]. It is important to note that their remarkable properties make supercapacitors key candidates for several applications which require high power density, long cycle life and excellent reversibility such as mobile communications, portable electronics, memory backup systems, hybrid electric vehicles, and military devices and where high power density is highly desired [5-10]. However, the major challenge is its low energy density [11]. The performances of supercapacitors are strongly dependent on the intrinsic fundamental physicochemical properties of electrode materials that they are made of [12]. Therefore, exploring electrodes interfacial properties to achieve high specific capacitance is one of the key tasks in order to successfully improve the energy density of supercapacitors.

In the recent past, a number of scholars have undertaken studies that demonstrated carbon-based materials as the most efficient material used for electric double layer supercapacitor electrodes because they exhibit high specific surface area, have good cycling stability, controllable porosity, high maximum power density and good safety [13,14]. On the other hand, the reversible ion adsorption limitation at the electrode/electrolyte interface hinders the attainment of high specific capacitance. Thus, the pseudo-capacitive materials can facilitate the achievement of that goal including good rate capability because their charge mechanism occurs through superficial faradic reactions.

To date, various pseudo-capacitive materials have been used as supercapacitor electrodes, such as metal oxide/metal hydroxide [15–22], and layered double hydroxides [23-25].

Consecutively, several studies reported on LDH as a promising supercapacitor electrode material because of their high specific capacitance, low-cost and facile synthesis procedure. They effectively allow the use of transition metal atoms to achieve unique structural property [27,28]. Thus, various LDHs have been successfully developed and studied for supercapacitor applications [26, 29-30].

Interestingly, most LDH studies have been focusing mainly on morphology control and the enhancement of surface area [31-33]. But very few studies were devoted to large scale synthesis of layered double hydroxides (LDH) [26]. Herein, we demonstrate a facile methodology to synthesize NiCo-LDH with the potential to be up-scaled for supercapacitor electrodes fabrication.

4.2. Experimental section

4.2.1. Preparation of NiCo-LDH@80°C

The sample was prepared via co-precipitation method as demonstrated in **chapter 3**. All chemicals were purchased from Sigma-Aldrich and used as received. The final product was named **NiCo-LDH@80°C** having (Ni:Co=1/2) as an atomic ratio.

4.2.2. Characterization techniques

The structural analysis of NiCo-LDH@80°C was carried out by a Rigaku Smartlab X-ray diffractometer having CuKα (λ= 1.5418Å) radiation. The FT-IR spectrum was recorded using the IR Tracer-100-SHIMADZU. Morphology composition was investigated using the JEOL JSM-7800F FE-SEM. The elemental composition was captured using the energy-dispersive x-ray spectroscopy (EDS) from thermos Fisher scientific, which was coupled to the SEM. X-ray photoelectron spectroscopy (XPS) measurements were performed by a KRATOS-SUPRA spectrometer using monochromatic AlKα radiation with hν=1486.6 eV and a base pressure of $1.2*10^{-8}$Torr.

4.2.3. Electrochemical characterization

4.2.3.1. Electrode preparation

The slurry was prepared by dispersing the active material (NiCo-LDH@80°C), carbon black and polyvinylidene fluoride (PVDF) in N-methyl pyrrolidone (NMP) in the weight ratio of (80 : 10 : 10). A glassy carbon GC50 with a disk diameter of 5 mm was used as a working electrode.

4.2.3.2. Electrochemical test

The electrochemical measurements were performed using an AUTOLAB PGSTAT302N electrochemical station controlled by NOVA 2.1 software.

The cyclic voltammetric tests were carried out using a three-electrode system. The measurement setup consists of glassy carbon, platinum wire and Ag/AgCl (3 M KCl-filled) used as a working electrode, counter and reference electrodes respectively.

In the current study, two types of aqueous electrolytes were used to evaluate the electrochemical behavior of NiCo-LDH@80°C. The used electrolytes were 1M Na_2SO_4 and 1 M KOH. The CV curves were collected in a voltage range from - 0.2 to 0.6 V at various voltage sweep 5, 10, 20, 30, 50, 75 and 100 mV/s. In addition, galvanostatic charge-discharge (GCD) were measured in 1M Na_2SO_4. While, the electrochemical impedance spectroscopy (EIS) measurements were performed with an AC amplitude of 5 mV in the frequency range of 100 kHz to 100MHz.

4.3. Results and discussion

4.3.1. Structural properties

The particular property that makes LDH to be a promising electrode for energy storage is its unique crystalline structure. Previous studies have demonstrated that during the faradaic redox charge transfer, the surface of LDH in conjunction with its entire crystalline structure is involved in the charge storage mechanism via intercalation/de-intercalation of electrolyte ions favoring the remarkable energy storage properties [31, 34-35].

Figure 4.1shows the diffraction peaks centered at 12.28°, 24.67°, 33°, 36.41°, and 59°.All diffraction peaks are indexed to the standard card (**JCPDS no. 14-0191**), and corresponded with the (003), (006), (009), (012) and (110) plane of hydrotalcite- structure [35, 40-42].

Moreover, the calculation related to the interlayer spacing was conducted and proved the spacing between nanosheets of the as-obtained LDH to be 0.771 nm (d_{003}) demonstrating the presence of carbonate ions and water molecules filling the interlayer spaces [44].

Moreover, the crystallinity of the as-synthesized sample as demonstrated via XRD patterns confirms the reliability of the adopted synthesis method to produce highly crystalline NiCo-LDH nanosheets.

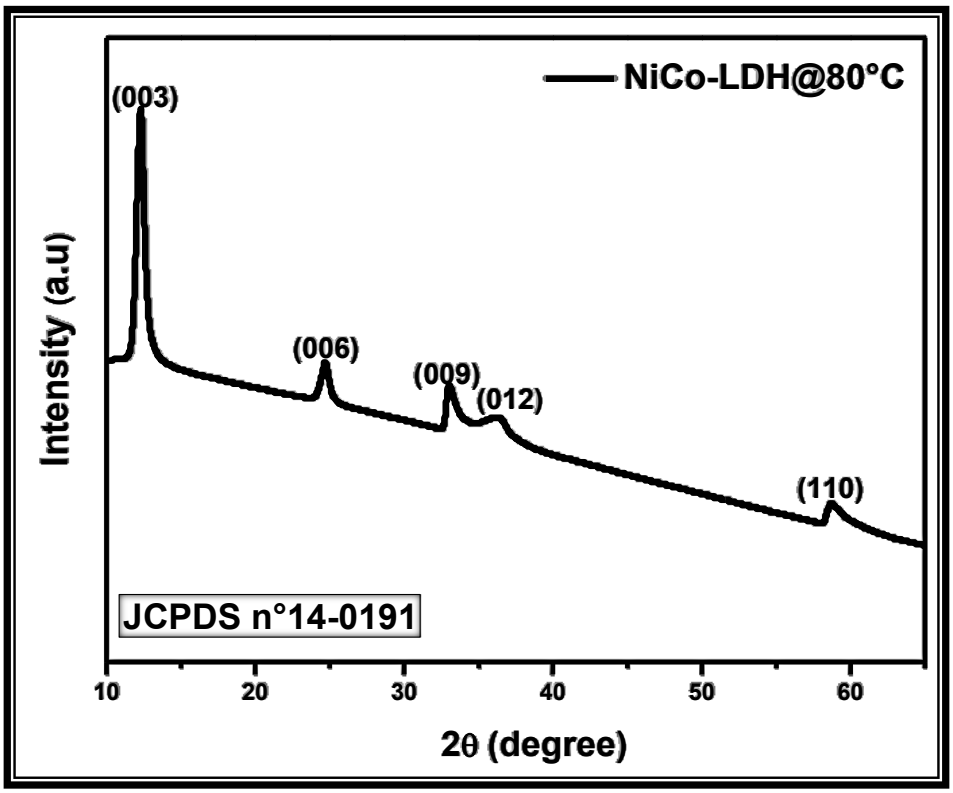

Figure 4.1: XRD pattern of NiCo-LDH@80°C.

4.3.2. Fourier Transform Infra-Red Spectroscopy

Recently, Teng Wang *et al*., reported that the hydrophilic nature of layered double hydroxides (LDH) is highly advantageous, especially during the diffusion of ions in aqueous solution electrolyte [35]. Thus, Richetta *et al.*, confirms that the presence of water within layered double hydroxides structure, no matter their types, either crystallite water or water adsorbed, they both contribute greatly to the excellent characteristics of layered double hydroxides [43].

Figure 4.2 displays the IR spectrum for NiCo-LDH@80°Cshowing a broad peak around 3635 cm^{-1} which was assigned to O-H stretching vibrations and ascribed to the water molecule and OH groups at the brucite-like layer and interlayer, followed by the peak at 1500 cm^{-1} [44-46]. Moreover, the peak at 1388 cm^{-1}can be assigned to the vibration stretching of interlayer carbonate anions retained in the interlayer of LDH [30, 35]. On the other hand, the peak at 638 cm^{-1} was ascribed to metal-oxygen (M-O) stretching and bending vibrations in the brucite-like lattice, confirming the existence of Nickel and Cobalt in the composites [30]. In addition, a peak located at 2241 cm^{-1} was assigned to the stretching vibrations of C≡N.

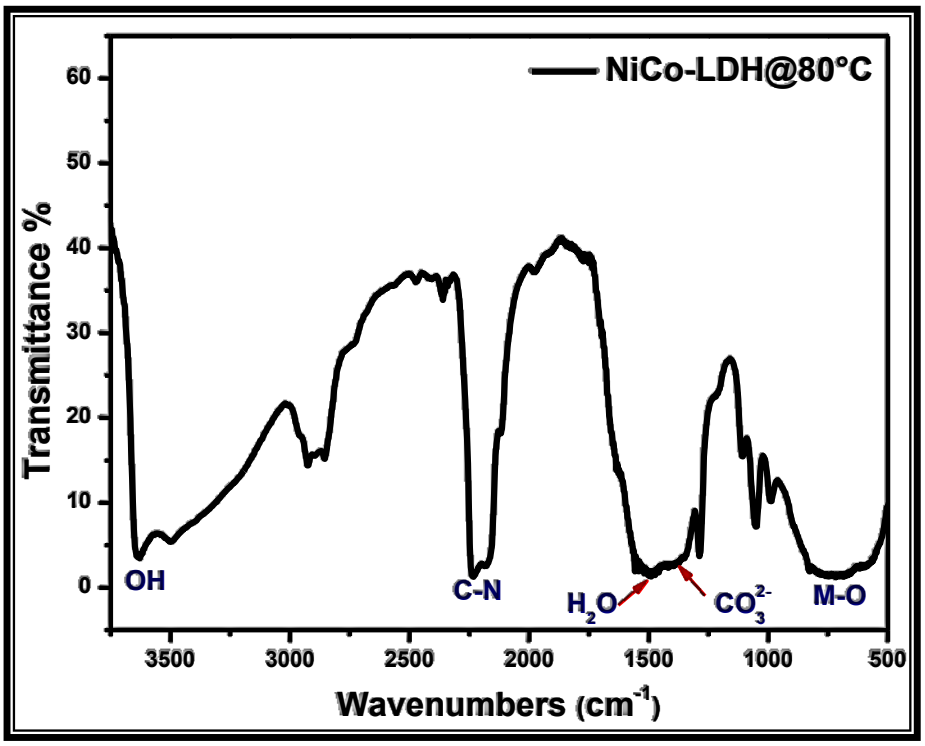

Figure 4.2: FT-IR spectrum of NiCo-LDH@80°C.

4.3.3. Surface morphology

The morphology of NiCo-LDH@80°C was analyzed using SEM. **Figure 4.3 (A)** exhibits a good arrangement of nanosheets linked to each other and presenting a structure like flowers. Moreover, **figure 4.3 (B)** depicts the EDS spectrum of NiCo-LDH@80°C sample which revealed the presence of all expected chemical elements among which, Nickel, Cobalt, and Oxygen without any form of impurities revealing the integrity of sample synthesis and handling. More interestingly, the distribution of all elements was relatively homogenous as revealed in **figure 4.3 (C)**. However, the detected carbon was due to the carbon tape resulting from the SEM sample preparation process. Finally, it was found that the atomic ratio (Ni:Co = 1:2) was strictly in accordance with the initial weights (see **figure 4.3 (B)/ Map Sum Spectrum**).

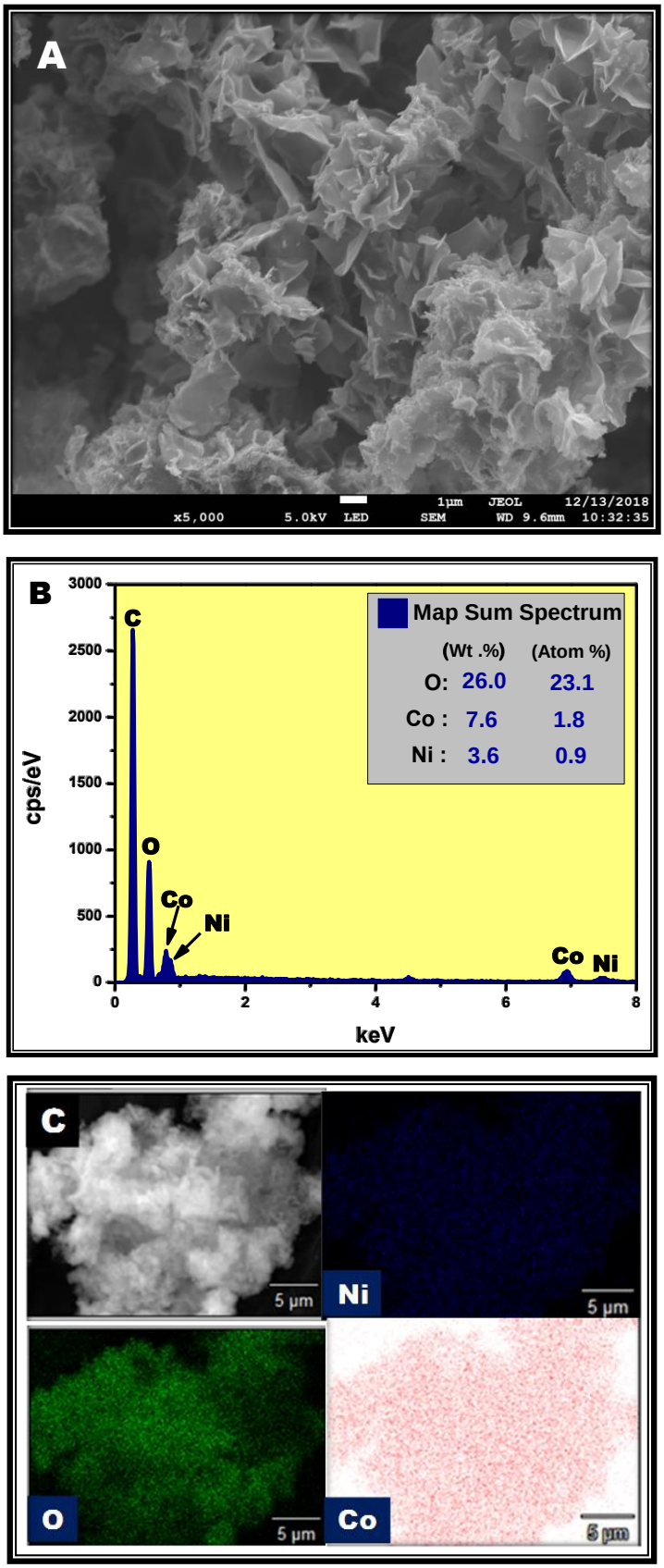

Figure 4.3: (A) FE-SEM micrograph and (B) EDS spectrum. (C) FE-SEM image of the area used to conduct EDS mappings and corresponding elemental mapping of O, Ni, Co.

4.3.4. X-ray Photoelectron Spectroscopy

In order to further unveil the surface chemical composition and elemental valence states of NiCo-LDH@80°C, X-ray Photoelectron Spectroscopy was conducted. It was found on the XPS survey scan the coexistence of all expected elements which were Nickel, Cobalt, and Oxygen (see **figure 4.4 (A)**). The XPS results are in accordance with the former EDS results presented and discussed above. Moreover, a remarkable N 1s core-level has been depicted as shown in **figure 4.4 (A)** and assigned to the remaining amount of nitrate precursors on the surface of NiCo-LDH@80°C. Finally, the C 1s core-level displayed on the XPS survey scan is ascribed to the C=C group originated from the presence of the carbonate ions in the LDH layers in accordance with the former FTIR results discussed above [35].

On the other hand, high-resolution XPS spectra were collected to get more insight into the valence states of elements on the surface. High-resolution spectra of NiCo-LDH@80°C revealed that both Ni 2p and Co 2p were split into doublets due to spin-orbit splitting. **Figure 4.4 (B)** presents Ni 2p core-level which appeared as a doublet showing a lower binding energy component Ni 2p3/2at about 853 eV and a well-defined satellite peak 858 eV. The main peak was ascribed to metallic Ni which corresponds to Ni^{2+} due to the surface oxidation confirming that Ni^{2+} was present in the hydroxide material. Consecutively, the Peak at 870 eV and 876 eV were assigned to Ni2p1/2 and satellite, respectively [47, 48]. On the other hand, **figure 4.4 (C)** presents the Co2p core-level spectrum of NiCo-LDH@80°C. As previously described for Ni 2p,Co 2p appeared as doublet Co 2p1/2 and 2p3/2, respectively located at 794 eV, 779 eV. Both peaks were associated with their respective satellite peaks [49]. Finally, **figure 4.4 (D)** displayed O1s core-level spectrum of NiCo-LDH@80. We applied a Gaussian deconvolution which revealed that the O 1s was the summation of two components at 528.38 eV and 528.16 eV that can be ascribed to the lattice oxygen [50-52].

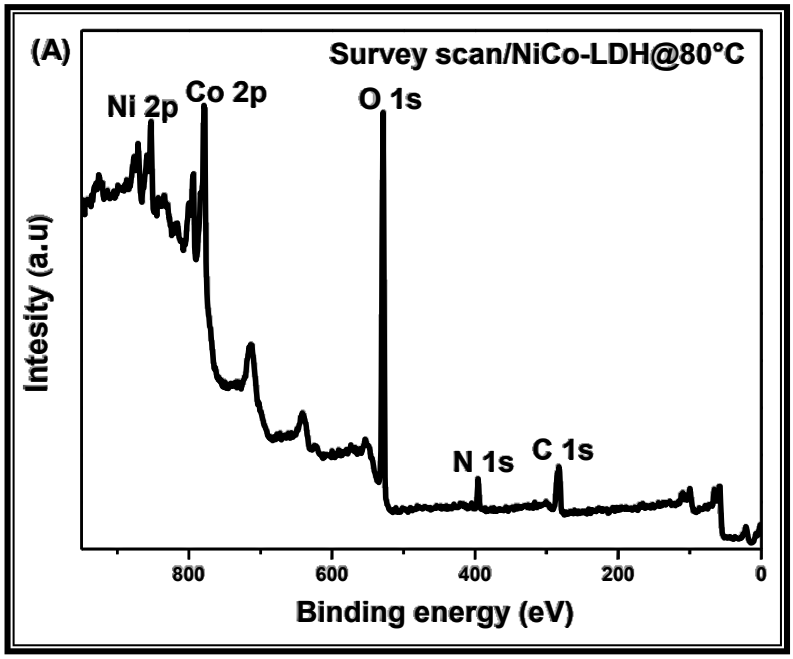
(A)
Survey scan/NiCo-LDH@80°C
Ni 2p
Co 2p
O 1s
N 1s
C 1s
Intesity (a.u)
800
600
400
200
0
Binding energy (eV)

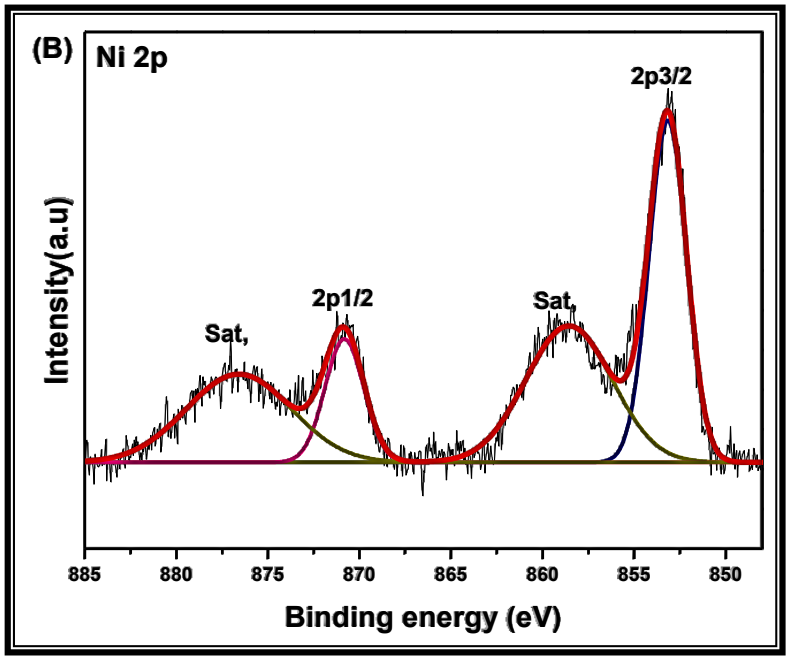
(B)
Ni 2p
2p3/2
2p1/2
Sat,
Sat,
Intensity(a.u)
885
880
875
870
865
860
855
850
Binding energy (eV)

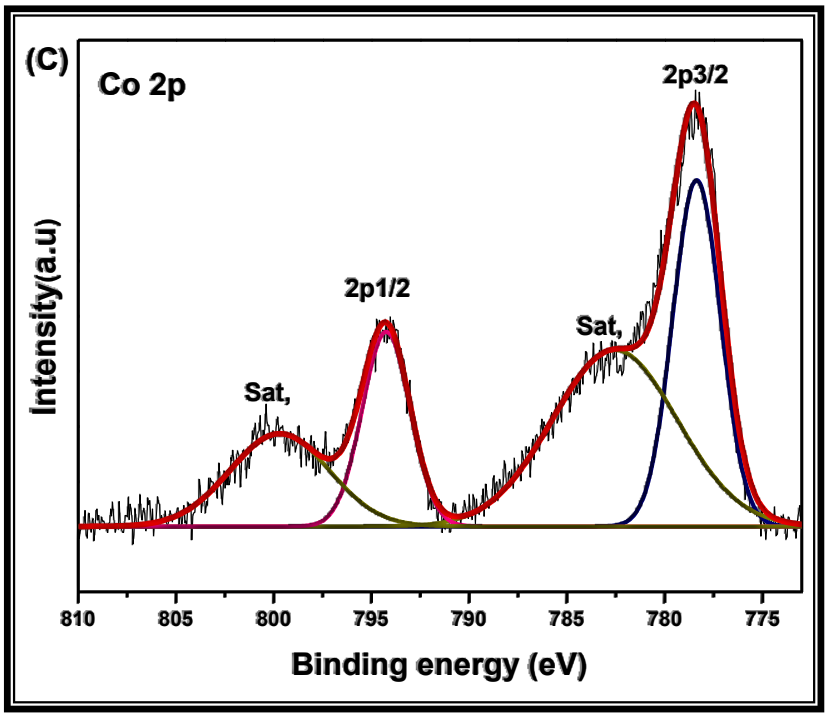

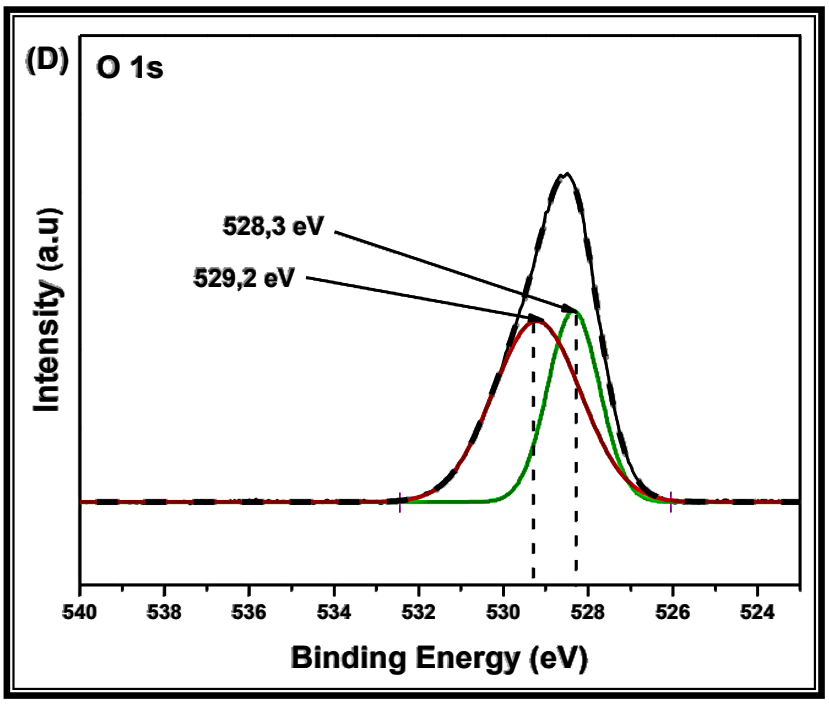

Figure 4.4: XPS spectra for NiCo-LDH@80°C:(A) Survey scan spectrum.(B) Ni2p, (C) Co2p and (D) O1s core levels.

4.3.5. Cyclic voltammetry

The cyclic voltammetry (CV) measurements were performed using a three-electrode system at various scan rates (from 5 mV/s to 100mV/s).

Figure 4.5 (A) shows practically symmetrical rectangular shape obtained in 1M Na_2SO_4 electrolyte at a scan rate of 5 mV/s between -0.2 to 0.6 V (vs. Ag/AgCl).This indicates an ideal capacitive behavior of NiCo-LDH@80° electrode material [53]. Moreover, it was clearly observed a peak at 0.4 V, demonstrating that the material overall capacitance was the result of a dual contribution of both double-layer capacitance and pseudo-capacitance. Generally, the presence of a peak at 0.4 V in a cyclic voltammogram is due to redox reactions [54]. Consequently, in this context whereby we are dealing with a material exhibiting both a nearly rectangular shape with redox peaks reveal the pseudo-capacitive nature of the materials [55]. Interestingly, the CV curves (see **figure 4.5 (B)**) at different voltage sweeps (from 5 to 100 mV/s) between -0.2 to 0.6 V have almost no inherent shape change when the scan rates increased from 5mV/s to 100 mV/s indicating relatively high-rate performance and high-current capability of the material in Na_2SO_4 electrolyte [56-57].

Furthermore, the cyclic stability of the NiCo-LDH@80°C electrode was tested in 1M Na_2SO_4 electrolyte by subjecting the electrode to 480 CV cycles at 200 mV/s. **Figure 4.5 (C)** revealed a capacitance increase from the first 50 cycles, which could be attributed to the stabilization of the material, its activation and the good penetration of electrolyte [58]. Surprisingly, it was observed no significant change regarding the performance once NiCo-LDH@80°C electrode was stabilized (after 300 cycles) indicating the ability of the electrode to preserve its electrochemical integrity along its structural. The CV curve possessing a larger mathematic area might also possess higher capacitance [59], thus, it can be noted that the capacitance value achieved after 480 cycles was higher than the capacitance recorded at the first cycle. The capacitance retention of the NiCo-LDH@80°C electrode was 89%. It was calculated by considering the highest capacitance value achieved by the electrode after 400 cycles.

Additionally, it can clearly be observed that after the exposure and stabilization of NiCo-LDH@80°C electrode at a higher scan rate the redox peak appears much prominent that before. The shift position observed could be attributed to the higher scan rate value during the test.

To further quantify the electrochemical behavior of NiCo-LDH@80°C, the galvanostatic charge/discharge (GCD) measurements were performed at different current density (0.2 Ag^{-1}, 0.3 Ag^{-1}, 0.5 Ag^{-1}, 0.7 Ag^{-1}, 1 Ag^{-1} and 1.6 Ag^{-1}) in 1M Na_2SO_4 electrolyte. The GCD curves are displayed in **figure 4.5 (D).** The linear shapes of the GCD curves correspond to the nearly rectangular shapes observed in the CV profile. It is worth mentioning that the symmetric GCD curves reveal the high reversible characteristic of the reactions that occur at the electrode/electrolyte interface.

Interestingly, in a comparison reason, NiCo-LDH@80°C was also tested in 1M KOH. **Figure 4.5 (E)** confirms the presence of exceptionally intense redox activity of the materials exhibiting clearly observable redox peaks at 0.28 V and 0.38 V demonstrating excellent pseudo-capacitive behavior of NiCo-LDH@80°C electrode in 1M KOH electrolyte. The obtained result shows that the pseudo-capacitive behavior of NiCo-LDH@80°C as shown in **figure 4.5 (E)** could be attributed to the faradaic redox reaction occurring between M-OH and M-O-O-H (with M representing Ni or Co ions) [60, 61].

More importantly, the specific capacitance (Csp) values of NiCo-LDH@80°C in 1M Na_2SO_4 electrolyte were calculated from CV curves using **equation 3.3** described in **chapter 3**. The highest specific capacitance obtained was **2140,625 Fg^{-1}** at 5 mV/s in 1M Na_2SO_4 due to the fact that at lower scan rates the electrolyte ions have sufficient time to penetrate the pores of the electrode material, while at higher scan rates only it accumulates on the outer surface (see **table 4.1**). Additionally, **table 4.2** displays the specific capacitance performance of various NiCo-LDH based electrodes. The present study high capacitance could be assigned to a relatively high crystalline structure as revealed in the previous XRD patterns which may contribute to effective ionic penetration into the electrode material pores.

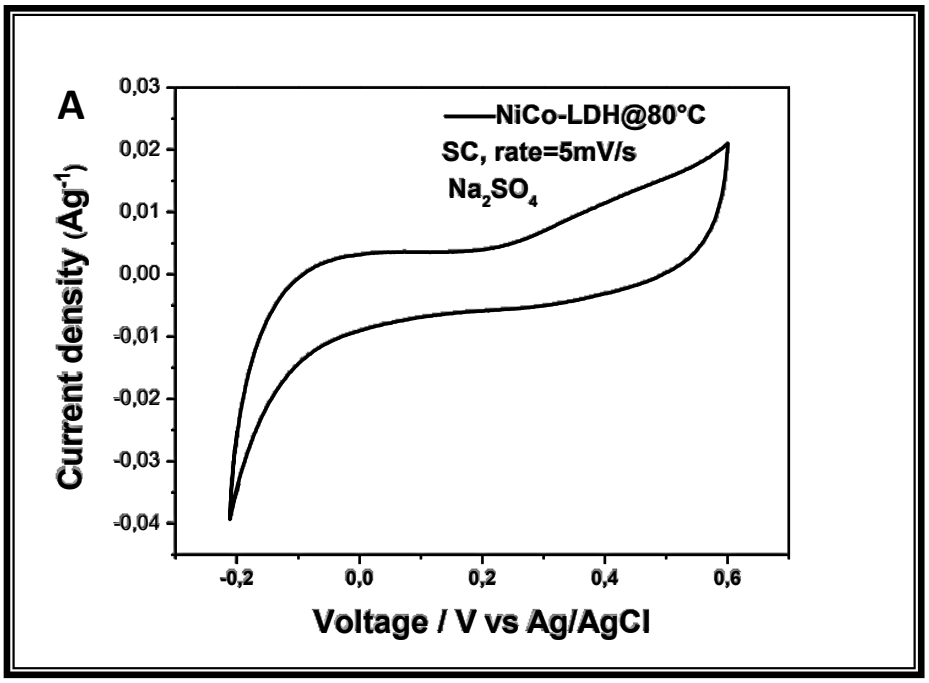

Figure 4.5: **(A)** CV curve of NiCo-LDH@80°C tested in 1M Na_2SO_4 at a scan rate of 5 mV/s.

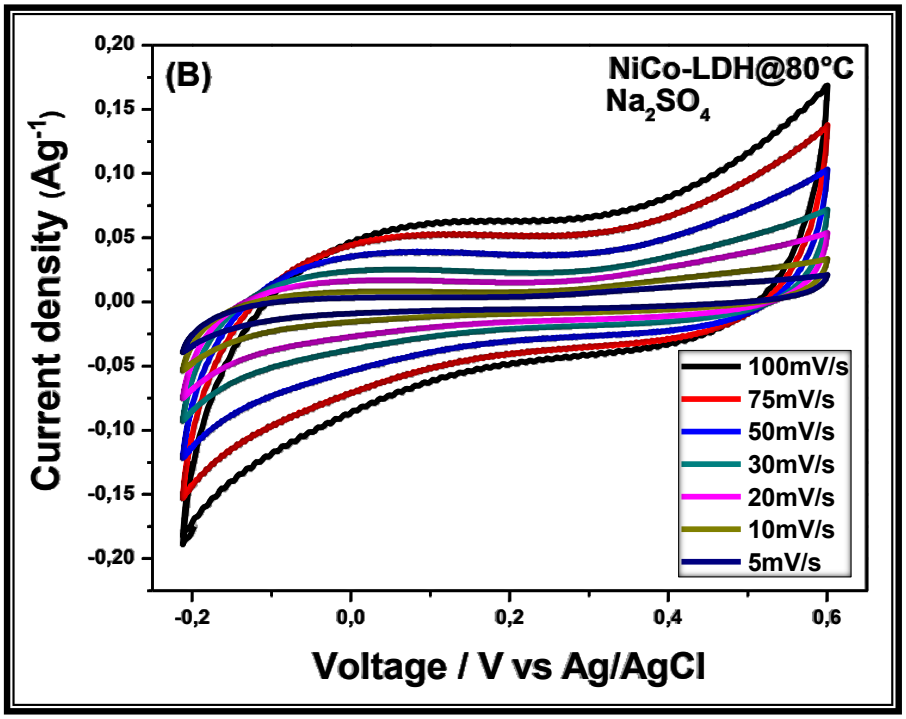

Figure 4.5: (B) CV curves of NiCo-LDH@80°C tested in 1M Na_2SO_4 at different scan rates from 5mV/s to 100 mV/s.

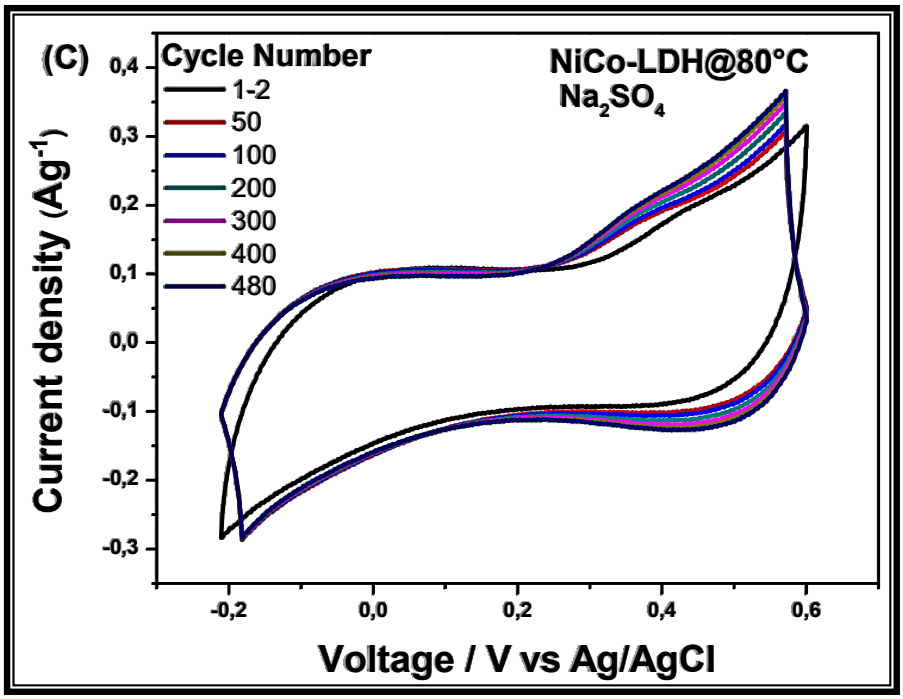

Figure 4.5: (C) Stability study of NiCo-LDH@80°C for 480 cycles tested in 1M Na_2SO_4 at a scan rate of200 mV/s.

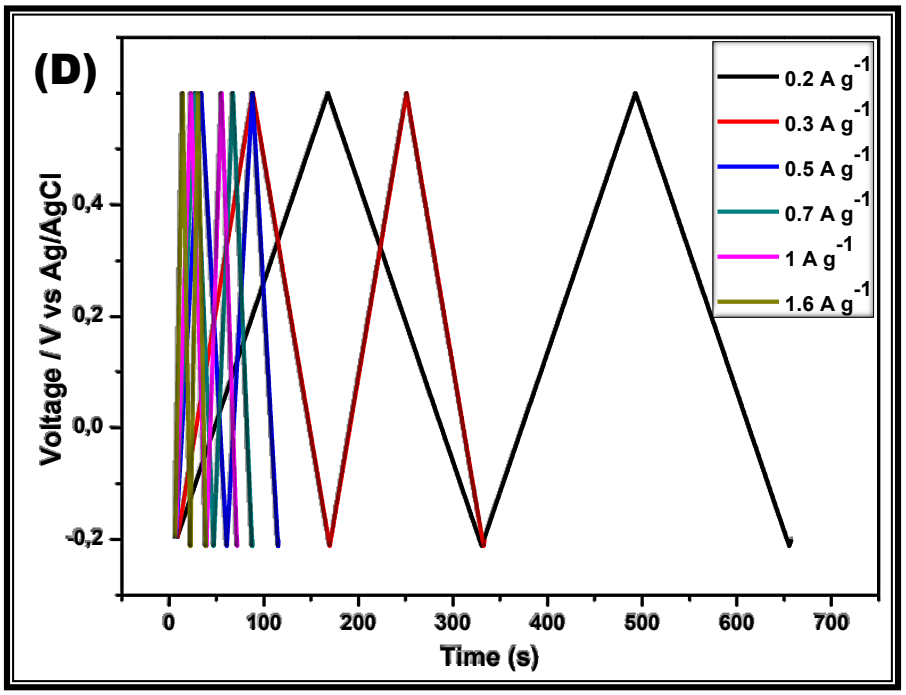

Figure 4.5: (D) GCD of NiCo-LDH@80°C in 1M Na_2SO_4 at different current density.

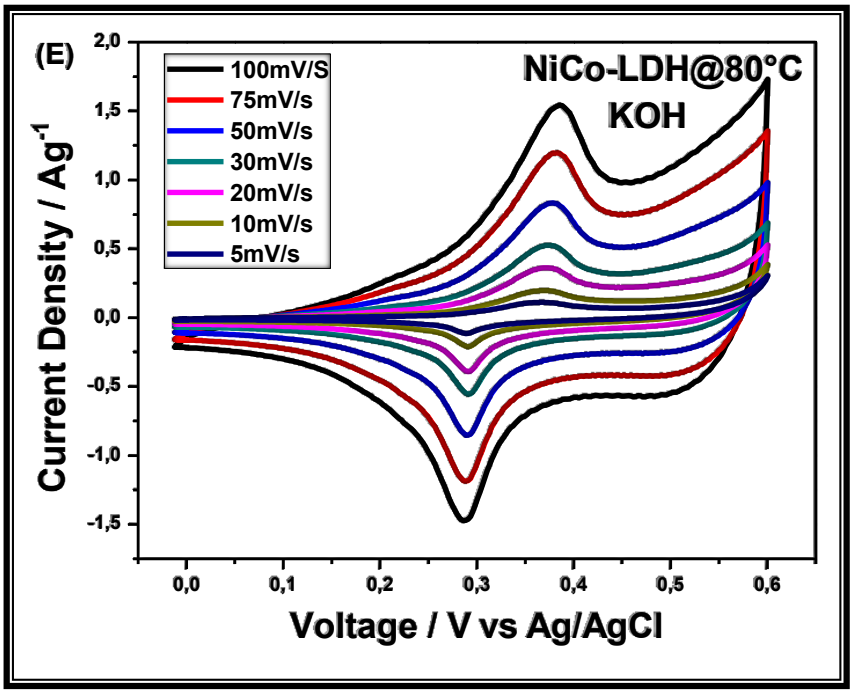

Figure 4.5: (E) CV curves of NiCo-LDH@80°C tested in 1M KOH at different scan rates from 5mV/s to 100mV/s.

Table 4.1: Specific capacitance calculation of NiCo-LDH@80°C in 1M Na_2SO_4 at various scan rates.

Scan rates	Specific Capacitance ($F.g^{-1}$)
100 mV/s	**895.3125**
75 mV/s	**983.333333**
50 mV/s	**1096.875**
30 mV/s	**1299.47917**
20 mV/s	**1394.53125**
10 mV/s	**1843.75**
5 mV/s	**2140.625**

Table 4.2: Specific capacitance performance of various NiCo-LDH based electrode.

Active material	Configuration	electrolyte	Specific Capacitance	References
(Ni,Co)Se2/NiCo-LDH//PC	2 electrode	3 M KOH	1224 F g-1	(63)
NiCoAl-LDH-NPs/CH-NWs //AC	2 electrode	6 M KOH	155.0 F g^{-1} (1.0 A g^{-1})	(64)
PANI/NiCo-LDH	3 electrode	2 M KOH	1845 F g^{-1} (0.5 A g^{-1})	(65)
α-phase NiCo DH microsphere	3 electrode	6 M KOH	1120 F g^{-1} (1 A g^{-1})	(66)
GS/NiCo-LDH	3 electrode	6 M KOH	1980.7 F g-1 (1 Ag-1)	(67)
CNF@Ni-Co LDH NR/ NS	3 electrode	-	1378.2 F g^{-1} (1 Ag^{-1})	(62)
Ni50Co50-LDH	3 electrode	6 M KOH	1537 F g^{-1} (0.5 A g^{-1})	(30)
NiCo-LDH/RGO	3 electrode	3 M KOH	1911.1 F g^{-1} (2 A g^{-1})	(59)
NiCo-LDH@CNT/NF	3 electrode	1 M KOH	2040 F g^{-1} (1 A g^{-1})	(60)
NiCo-LDH/CFC	3 electrode	KOH-PVA (solid)	2762.7 F g-1	(35)
NiCo-LDH/Ag/NF hybrid	3 electrode	1 MKOH	2920 Fg^{-1} (5 Ag^{-1})	(68)
MnO_2@NiCo-LDH/CoS_2nanocages	3 electrode	2 M KOH	1547 F g^{-1} (1 A g-1)	(69)
CoNiFe-LDH/CNFs	3 electrode	6 M KOH	1203 F g^{-1}(1 A g^{-1})	(70)
NiCo-LDH nanosheets	3 electrode	1 M Na_2SO_4	2140 F g^{-1}	This work

4.3.6. Electrochemical Impedance spectroscopy

As depicted in **figure 4.6**, electrochemical impedance spectroscopy (EIS) was carried out to further investigate the electrochemical properties of NiCo-LDH@80°C with the Nyquist plot recorded in the range of 100 kHz to 100 MHz at the open-circuit potentials. Ordinarily, the vertical slope in the lower frequency range of the plot indicates low ionic diffusion resistance and charge transfer at the interface between NiCo-LDH@80°C electrode and electrolyte [62]. Finally, the slight semicircle is the result of a relatively low interfacial resistance in the system.

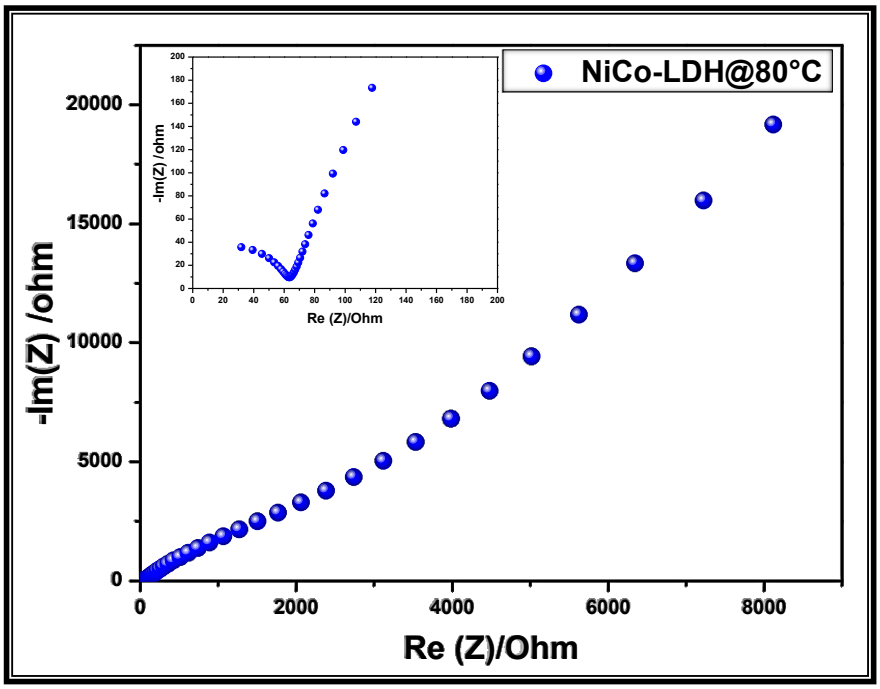

Figure 4.6: Nyquist plot of the NiCo-LDH@80°C in 1M Na_2SO_4.

4.4. Conclusion

In summary, we successfully produced NiCo-LDH@80°C by a simple co-precipitation method. The XRD and FT-IR have confirmed the reliability of the synthesis method to obtain NiCo-LDH. The as-prepared NiCo-LDH@80°C was tested as a supercapacitor electrode in 1 M Na_2SO_4 electrolyte and the specific capacitance high as **2140 Fg^{-1}** at the scan rate of 5 mV/s has been obtained. Moreover, NiCo-LDH@80°C was also tested in 1 M KOH electrolyte and the results revealed relatively high pseudo-capacitance behavior of NiCo-LDH@80°C in KOH. In addition, the synthesis method presented in this study provides a pathway for the large scale synthesis of NiCo-LDH and can be extended to the synthesis of other LDH for various energy conversion and storage applications.

4.5. References

[1] C. Largeot *et al.*, Relation between the ion size and pore size for an electric double-layer capacitor, ***J. Am.Chem. Soc***. 46 (**2008**) 30.

[2] B. Dyatkin *et al.*, Development of a green supercapacitor composed entirely of environmentally friendly materials, ***ChemSusChem***, 6 (**2013**) 2269.

[3] H. Chen *et al.*, Highly conductive NiCo2S4 urchin-like nanostructures for high-rate pseudocapacitors, ***Nanoscale,*** 5 (**2013**) 8879.

[4] M. Huang *et al.*, High performance asymmetric supercapacitor based on CoAlLDH/GF and activated carbon from expanded graphite, ***Ceram. Int.,*** 40 (**2014**) 5533.

[5] J. Zhang *et al.*, Preparation of cobalt hydroxide nanosheets on carbon nanotubes/carbon paper conductive substrate for supercapacitor application, ***Electrochim. Acta***, 104 (**2013**) 110.

[6] W. Lu *et al.*, Graphene: Fundamentals and functionalities, ***MRS Bull***., 37 (**2012**) 1119.

[7] G. Wang *et al.*, A review of electrode materials for electrochemical supercapacitors, ***Chem. Soc. Rev***., 41 (**2012**) 797.

[8] Z. Gao *et al.*, A New Partially Reduced Graphene Oxide Nanosheet/Polyaniline Nanowafer Hybrid as Supercapacitor Electrode Material, ***Energy Fuels***, 27 (**2012**) 568.

[9] L. Huang *et al.*,Nickel–Cobalt Hydroxide Nanosheets Coated on NiCo2O4 Nanowires Grown on Carbon Fiber Paper for High-Performance Pseudocapacitors, ***Nano Lett.***, 13 (**2013**) 3135.

[10] Q. Chen *et al.*, In situ shape and phase transformation synthesis of Co3S4 nanosheet arrays for high-performance electrochemical supercapacitors, ***RSC Adv***., 3 (**2013**) 22922.

[11] Brian Kihun Kim *et al.*, Electrochemical Supercapacitors for Energy Storage and Conversion, ***Handbook of Clean Energy Systems*** (**2015**). DOI: 10.1002/9781118991978.hces112.

[12] Antonino SALVATORE ARICÒ *et al.*; Nanostructured materials for advanced energy conversion and storage devices nature materials, Vol. 4, (**2005**). **www.nature.com/naturematerials**.

[13] G. Wang *et al.*, Enhanced capacitance in partially exfoliated multi-walled carbon nanotubes. ***J. Power Sources***, 196 (**2011**) 5209.

[14] J. Gamby *et al.*, Studies and characterisations of various activated carbons used for carbon/carbon supercapacitors. ***J. of Power Sources***, 101 (**2001**) 109.

[15] F. Luanet *et al*., High energy density asymmetric supercapacitors with a nickel oxide nanoflake cathode and a 3D reduced grapheme oxide anode. ***Nanoscale,*** 5 (**2013**) 7984.

[16] X. Lu *et al*., Hydrogenated TiO_2 nanotube arrays for supercapacitors. ***Nano Lett***. 12 (**2012**) 1690.

[17] L. Chen *et al*. Synthesis and pseudocapacitive studies of composite films of polyaniline and manganese oxide nanoparticles. ***J. PowerSources,*** 195 (**2010**) 3742.

[18] G. M. Wang *et al*., LiCl/PVA Gel Electrolyte Stabilizes Vanadium Oxide Nanowire Electrodes for Pseudocapacitors. ***Acs Nano,*** 6 (**2012**) 10296.

[19] G. Yu *et al*. Solution-processed graphene/MnO_2 nanostructured textiles for high-performance electrochemical capacitors. ***NanoLett***. 11 (**2011**) 2905.

[20] X. Xiao *et al*. Fiber-Based All-Solid-State Flexible Supercapacitors for Self-Powered Systems. ***ACS Nano*** 6 (**2012**) 9200.

[21] J. Cheng *et al*. Hierarchical Core/Shell $NiCo_2O_4$@$NiCo_2O_4$ Nanocactus Arrays with Dual-functionalities for High PerformanceSupercapacitors and Li-ion Batteries. ***Sci. Rep***. 5 (**2011**) 12099.

[22] Z. Lu *et al*., Beta-phased $Ni(OH)_2$ nanowall film with reversible capacitance higher than theoretical Faradic capacitance. ***Chem. commun***. 47 (**2011**) 9651..

[23] J. Luo *et al*., Three-dimensional graphene-polyaniline hybrid hollow spheres by layer-by-layer assemblyfor application in supercapacitor. ***Electrochim. Acta,*** 173 (**2015**) 184.

[24] G. Yu *et al*., Hybrid nanostructured materials for high-performance electrochemical capacitors. ***Nano. Energy,*** 2 (**2013**) 213.

[25] L. Yuan *et al*., Polypyrrole-coated paper for flexible solid-state energy storage. ***Energy Environ. Sci***. 6 (**2013**) 470.

[26] L. Yuan *et al*., Paper-based supercapacitors for self-powered nanosystems. Angew. ***Chem. Int. Edit***., 51 (**2012**) 4934.

[27] Y. Zou *et al*., Interconnecting Carbon Fibers with the In-situ Electrochemically Exfoliated Graphene as Advanced Binder-freeElectrode Materials for Flexible Supercapacitor. ***Sci. Rep***. 5 (**2015**) 11792.

[28] L. Xie *et al*. CoxNi1−x double hydroxide nanoparticles with ultrahigh specific capacitances as supercapacitor electrode materials. ***Electrochim.Acta,*** 78 (**2012**) 205.

[29] W. R. Lin *et al*. Superior Performance Asymmetric Supercapacitors Based on Flake-like Co/Al Hydrotalcite and Graphene. ***Electrochim. Acta***., 143 (**2014**) 331.

[30] R. Li *et al*. Large Scale Synthesis of NiCo Layered Double Hydroxides for Superior Asymmetric Electrochemical Capacitor. ***Sci. Rep***. 6 (**2016**) 18737. DOI: 10.1038/srep18737.

[31] W. Yang *et al*., Solvothermal One-Step Synthesis of Ni–Al Layered Double Hydroxide/Carbon Nanotube/Reduced Graphene Oxide Sheet Ternary Nanocomposite with Ultrahigh Capacitance for Supercapacitors, ***ACS Appl. Mater. Interfaces***, 5 (**2013**) 5443.

[32] A. Zhang *et al*., A hybrid aerogel of Co–Al layered double hydroxide/graphene with three-dimensional porous structure as a novel electrode material for supercapacitors, ***RSC Adv.,*** 5 (**2015**) 26017.

[33] Y. Lin *et al*., Understanding the enhancement of electrochemical properties of NiCo layered double hydroxides via functional pillared effect: An insight into dual charge storage mechanisms, ***Electrochimica Acta,*** 246 (**2017**) 406.

[34] Kun Xiang *et al*., Surface Sulfurization of NiCo-Layered Double Hydroxide Nanosheets Enable Superior and Durable Oxygen Evolution Electrocatalysis, ***ACS Appl. Energy Mater***., 1 (**2018**) 4040.

[35] Teng Wang *et al*., 2-methylimidazole-derived Ni-Co Layered Double Hydroxide Nanosheets as High Rate Capability and High Energy Density Storage Material in Hybrid Supercapacitors. ***ACS Appl. Mater. Interfaces*** 9 (**2017**) 15510.

[36] R. R. Salunkhe *et al*., Aligned nickel-cobalt hydroxide nanorod arrays for electrochemical pseudocapacitor applications. ***RSC Adv***., 2 (**2012**) 3190.

[37] G. Zhang *et al*., Controlled growth of NiCo2O4 nanorods and ultrathin nanosheets on carbon nanofibers for high performance supercapacitors. ***Sci. rep***. 3 (**2013**) 1470.

[38] T. Brousse *et al*., To Be or Not to Be Pseudocapacitive? ***J. Electrochem***. ***Soc.*** 162 (**2015**) A5185.

[39] Y. Wang *et al*., Electrochemical Capacitors: Mechanism, Materials, Systems, Characterization and Applications. ***Chem. Soc. Rev.***, 45 (**2016**) 5925-.

[40] Marcela Piassi Bernardo *et al*., [Mg-Al]-LDH and [Zn-Al]-LDH as Matrices for Removal of High Loadings of Phosphate, ***Materials Research***., 3 (**2018**) 21.e20171001, DOI: http://dx.doi.org/10.1590/1980-5373-MR-2017-1001.

[41] Tae-Hyun Kim *et al*., Size- and surface charge-controlled layered double hydroxides for efficient algal flocculation, ***Environ. Sci.: Nano***, 5 (**2018**) 183.

[42] Xueqin Wang *et al*., Controllable Synthesis of NiCo LDH Nanosheets for Fabrication of High-Performance Supercapacitor Electrodes; ***Electroanalysis***, 29 (**2017**) 1286.

[43] M Richetta *et al*., Layered Double Hydroxides: Tailoring Interlamellar Nanospace fora Vast Field of Applications. ***J. Material Sci. Eng*** 6(**2017**) 360.DOI: 10.4172/2169-0022.1000360.

[44] V. Rives, Layered Double Hydroxides: Present and Future. ***Nova Science Publishers*** (**2001**) New York, NY, USA.

[45] Yuqing Qiao*et al*., One-pot synthesized mesoporous Ni–Co hydroxide for high performance supercapacitors, ***Ionics***, 23 (**2017**) 1229.

[46] M. Del Arco *et al*., Cobalt-Iron Hydroxycarbonates and their evolution to mixed oxides with Spinel Structure. ***J. Mater. Chem***., 8 (**1998**) 761.

[47] Huiming Li *et al*., Phase-Controlled Synthesis of Nickel Phosphide Nanocrystals and Their Electrocatalytic Performance for the Hydrogen Evolution Reaction; ***Chem. Eur. J.,*** 24 (**2018**) 11748 – 11754. Doi: 10.1002/Chem. 201801964

[48] Y. Pan *et al*., Monodispersed nickel phosphide nanocrystals with different phases: synthesis, characterization and electrocatalytic properties for hydrogen evolution, ***Mater. Chem***., A 3 (**2015**) 1656.

[49] Jong-Woo Kima *et al*., Solution-processed n-ZnO nanorod/p-Co_3O_4 nanoplate heterojunctionlight-emitting diode, ***Applied Surface Science,*** 406 (**2017**) 192.

[50] H.C. Yao *et al*., Ceria in automotive exhaust catalysts: I. Oxygen storage, ***J. Catal***., 86 (**1984**) 254.

[51] G. Li *et al*., Thermally stable ordered mesoporous CeO_2/TiO_2 visible-light photocatalysts, ***Phys. Chem. Chem. Phys***. 11 (**2009**) 3775.

[52] Z. Zhang *et al*., Flower-like hydrogenated TiO_2(B) nanostructures as anode materials for high-performance lithium ion batteries, ***Power Sources***, 267 (**2014**) 388.

[53] Wei Chen *et al*., capacitance of manganese oxide via confinement inside carbon nanotubes, ***Royal Society of Chemistry*** (**2010**).

[54] Yohan Dall'Agnese, Study of early transition metal carbides for energy storage applications. Mechanics of materials [physics.class-ph]. ***Université Paul Sabatier - Toulouse III***, (**2016**).

[55] J.P. Zheng *et al*., Hydrous Ruthenium Oxide as an Electrode Material for Electrochemical Capacitors. ***Journal of the Electrochemical Society***, 142 (**1995**) 2699.

[56] Yan Tao *et al*., Nickel–cobalt layered double hydroxide ultrathin nanoflakes decorated on graphene sheets with a 3D nanonetwork structure as supercapacitive materials, ***Materials Research Bulletin***, 51 (**2014**) 97.

[57] J. Yan *et al*. Fast and reversible surface redox reaction of graphene–MnO2 composites as supercapacitor electrodes.***Carbon***, 48 (**2010**) 3825.

[58] Juan Xu *et al*., Tungsten oxide nanofibers self-assembled mesoscopic microspheres as high-performance electrodes for supercapacitor, ***Electrochim. Acta.,*** 174 (**2015**) 728e734.

[59] X. Cai et al., Solvothermal Synthesis of NiCo-Layered Double Hydroxide Nanosheets Decorated on RGO Sheets for High Performance Supercapacitor, ***Chemical Engineering Journal*** (**2015**), doi: http://dx.doi.org/10.1016/j.cej.2015.01.072

[60] Xiaocheng Li *et al*., A super-high energy density asymmetric supercapacitor based on 3D core–shell structured NiCo-layered double hydroxide@carbon nanotube and activated polyaniline-derived carbon electrodes with commercial level mass loading. ***J. Mater. Chem.****A*3 (**2015**) 13244.

[61] Shuai Yu *et al*., Synthesis of NiMn-LDH anosheet@Ni3S2 Nanorod Hybrid Structures for Supercapacitor Electrode Materials with Ultrahigh Specific Capacitance. ***Scientific Reports***, 8 (**2018**) 5246.

[62] F. Lai *et al*, Controllable preparation of multi-dimensional hybrid materials of nickel-cobalt layered double hydroxide nanorods/nanosheets on electrospun carbon nanofibers for high-performance supercapacitors, ***Electrochim. Acta,*** 174 (**2015**) 456..

[63] X. Li *et al*, (Ni,Co)Se_2 /NiCo-LDH Core/Shell Structural Electrode with the Cactus-Like (Ni,Co) Se_2 Core for Asymmetric Supercapacitors, (**2018**) 1803895.

[64] J. Yang et al, 3D Architecture Materials Made of NiCoAl-LDH Nanoplates Coupled with NiCo-Carbonate Hydroxide Nanowires Grown on Flexible Graphite Paper for Asymmetric Supercapacitors, ***Adv. Energy Mater***., (**2014**) 1400761.

[65] X. Ge *et al*, Hierarchical PANI/NiCo-LDH Core-Shell Composite Networks on Carbon Cloth for High Performance Asymmetric Supercapacitor. ***Nanomaterials***, 9 (**2019**) 527.

[66] J. Li *et al*, M. High-stable α-phase NiCo double hydroxide microspheres via microwave synthesis for supercapacitor electrode materials, ***Chem. Eng. J.***, 316 (**2017**) 277.

[67] Y. Tao *et al*, One-pot microwave-assisted synthesis of reduced graphene oxide/nickel cobalt double hydroxide composites and their electrochemical behavior, ***Mater. Res. Bull.***, 51 (**2014**) 97.

[68] T. Guan *et al*, Self-supported ultrathin NiCo-LDH nanosheet array/Ag nanowire binder-free composite electrode for high-performance supercapacitor, ***J. Alloys Compd***.,799 (**2019**) 521.

[69] X. Wang *et al*, Unique MOF-derived hierarchical MnO 2 nanotubes@ NiCo-LDH/CoS 2 nanocage materials as high performance supercapacitors, ***J. Mater Chem***. A, 7 (**2019**) 12018.

[70] F. Wang *et al*, High performance asymmetric supercapacitor based on Cobalt Nickel Iron-layered double hydroxide/carbon nanofibres and activated carbon, ***Sci. Rep***. 7 (**2017**) 4707.

Chapter 5. Conclusion and future works

5.1. Conclusion

The present dissertation report on a facile co-precipitation methodology to synthesize NiCo-LDH with the potential to be up-scaled for energy storage industrial applications including supercapacitor electrodes.

The XRD analysis has revealed a plane of hydrotalcite – structure indexed to the standard card (**JCPDS no. 14-0191**). The FTIR spectroscopy demonstrated the presence of functional groups in respect with the LDHs structure. The SEM analysis has revealed a structure like flowers comprising nanosheets. Finally, the EDS and XPS analysis have demonstrated the presence of all expected elements and the integrity of sample synthesis excluding unwanted impurities.

On the other hand, the electrochemical tests of NiCo-LDH@80°C as a supercapacitor electrode were studied via cyclic voltammetry which demonstrated excellent electroactive properties in 1M Na_2SO_4 electrolyte showing a capacitance up to 2140 Fg^{-1} at the scan rate of 5 mV/s. In addition, the cyclic voltammetry analysis conducted in 1M KOH revealed a relatively high pseudo-capacitive activity as compared to Na_2SO_4 due to favorable reactions at the electrolyte-electrode interface. Finally, the electrochemical impedance spectroscopy has exhibited moderate results.

5.2. Future work

Although a large number of research studies have demonstrated co-precipitation synthesized NiCo-LDH to exhibit exceptional electrochemical performances for energy conversion and storage, the quality of LDH still needs to be improved for stable device fabrication. More focus should be given to composites based on LDH with controlled interlayer distance with subsequent clean, highly stable and high-quality structures, which are suitable for energy storage applications. It is particularly important to fully understand the redox dynamic and its effect on the overall capacitance in various electrolytes including polymer electrolytes for solid-state energy storage devices. In addition, the two-electrode test and practical device fabrication is recommended in order to fully understand the applicability of NiCo-LDH material for efficient energy storage capability.

Publications

Int. J. Electrochem. Sci., 15 **(2020)** 4494 – 4502, doi: 10.20964/2020.05.33

International Journal of
ELECTROCHEMICAL
SCIENCE
www.electrochemsci.org

Up-scalable synthesis of highly crystalline electroactive Ni-Co LDH nanosheets for supercapacitor applications

G.E. Nyongombe[1], *G.L. Kabongo*[1,2,3,*], *L.L. Noto*[1], *M.S. Dhlamini*[1,*]

[1] Department of Physics, School of Science, CSET, University of South Africa, Private Bag X6, Florida, 1710, Science Campus, Christiaan de Wet and Pioneer Avenue, Florida Park, Johannesburg, South Africa
[2] TS&BHP S.E.N.C., Saint-Jean-sur-Richelieu, Québec J3B 6X4, Canada
[3] Département de Physique, FNEA, Université Pédagogique Nationale, 8815 Kinshasa, R.D. Congo
[*]E-mail: leba.kabongo@gmail.com, dhlamms@unisa.ac.za

Received: 5 August 2019 / *Accepted:* 22 September 2019 / *Published:* 10 April 2020

The development of cost-effective and scalable synthetic methods is of paramount importance to achieve industrial application of energy conversion and storage devices based on layered double hydroxides (LDH). Herein, we synthesized NiCo-LDH nanosheets via a simple up-scalable co-precipitation method at relatively low temperature. Moreover, we used several characterization techniques to unveil the unique properties of the novel NiCo-LDH among which XRD, EDS, XPS and FT-IR. Consequently, we further investigated NiCo-LDH nanosheets using cyclic voltammetry (CV) and electrochemical impedance spectroscopy (EIS) to evaluate the electroactivity of the as-synthesized NiCo-LDH for energy storage. Overall, the electrochemical test of the as-synthesized NiCo-LDH revealed remarkable performance exhibiting a specific capacitance as high as 2,140 Fg^{-1} (5 mV/s).

Keywords: NiCo-LDH nanosheets, co-precipitation, EIS, cyclic voltammetry, supercapacitor

1. INTRODUCTION

Over the past two decades, scientists in the global technological arena have conducted gigantic research and development initiatives to practically develop energy storage devices [1-4]. Layered double hydroxides (LDH) a class of ionic lamellar compounds, also known as anionic clays have tremendously attracted scientific attention worldwide. Accordingly, they became the center of a massive technological interest because of their excellent properties such as facile synthesis, unique structure, unvarying distribution of diverse metal cations in the brucite layer, surface hydroxyl groups, easy tunability, intercalated anions with interlayer spaces, good chemical stability and the ability to intercalate diverse varieties of anions (inorganic, organic, biomolecules, and even genes) [5]. The

unique advantages of LDH among others layered materials are the possibility to obtain through the synthesis the compositions and the combinations of metal-anions [5].

Several authors have reported studies related to the synthesis of Layered Double Hydroxides (LDH). Thus, various simple as well as expensive ways to synthesize Layered Double Hydroxides (LDH) for various applications were discussed [6-8]. However, previous studies on LDH were mostly focused on the controlled morphology, the enhanced surface area and other significant properties [9-12]. Nevertheless, the astonishing scarcity of studies focusing on large scale synthesis of LDH open doors to the greatest possible progress in the field for practical applications highly needed [13].

In this present study, we have successfully synthesized and presented the facile and scalable methodology to synthesize a novel NiCo-LDH nanosheets material having a high cristallinity and exhibiting good electrochemical properties for supercapacitor electrode applications relative to previous studies [13].

2. EXPERIMENTAL

2.1. Synthesis of NiCo-LDH nanosheets

The as-synthesized NiCo-LDH nanosheets were synthesized via co-precipitation method (Fig. 1a). All the chemicals purchased from Sigma-Aldrich was used without further purification. In a typical procedure, 10 mmol of $Ni(NO_3)_2 \bullet 6H_2O$ and 20 mmol of $Co(NO_3)_2 \bullet 6H_2O$ were dispersed in an initial solution containing 152 ml of $(CH_2OH)_2$ in 60 ml of deionized water under vigorous stirring for 8 minutes. Thereafter, 148 mmol of Urea were added to the mixture solution while maintaining vigorous stirring for another 12 minutes. The final solution was further aged for 3 h at 90°C. Finally, the precipitates were filtered and washed with deionized water and ethanol several times and dried at 80°C overnight. The as-obtained product was named NiCo-LDH@80°C having (Ni:Co=1/2) atomic ratio.

2.2. Materials characterization and electrochemical measurements

XRD study was conducted using a RigakuSmartlab diffractometer (λ = 1.54 nm). FT-IR spectrum was recorded using IR Tracer-100-SHIMADZU (3750-500 cm^{-1}). The morphology and chemical composition of the sample were characterized by scanning electron microscope (SEM-EDS JEOL JSM-7800F) coupled to EDS detector. XPS measurements were conducted using a KRATOS-SUPRA spectrometer using a monochromatic Al Kα radiation with hν=1486.6 eV and a base pressure of $1.2*10^{-8}$Torr.

The slurry was prepared by blending the active material, carbon black and polyvinylidene fluoride (PVDF) in a ratio of (80:10:10) in N-methylpyrrolidone (NMP) and sonicated for 10 min. The obtained slurry (100 μL) was drop-cast on glassy carbon and allowed to dry. Electrochemical data were collected on an Autolab PGSTAT302N potentiostat using a three-electrode system. Glassy carbon, platinum wire and Ag/AgCl (3 M KCl-filled) were used as working, counter and a reference

electrode, respectively. 1 M Na_2SO_4 solution was used as electrolyte. Finally, EIS measurements were performed with AC amplitude of 5 mV in the frequency range of 100 kHz-100 mHz.

3. RESULTS AND DISCUSSION

XRD and FTIR served to conduct structural studies of NiCo-LDH@80°C sample (Fig. 1). As depicted in Fig. 1b the diffraction peaks centered at 12.28°, 24.67°, 33°, 36.41° and 59° were attributed to (003), (006), (009), (012) and (110) plane of hydrotalcite-structure (JCPDS # 14-0191) standard card, respectively [14]. Moreover, the crystallinity of the as-synthesized sample as demonstrated via XRD patterns confirms the reliability of the adopted synthesis method to produce highly crystalline NiCo-LDH nanosheets.

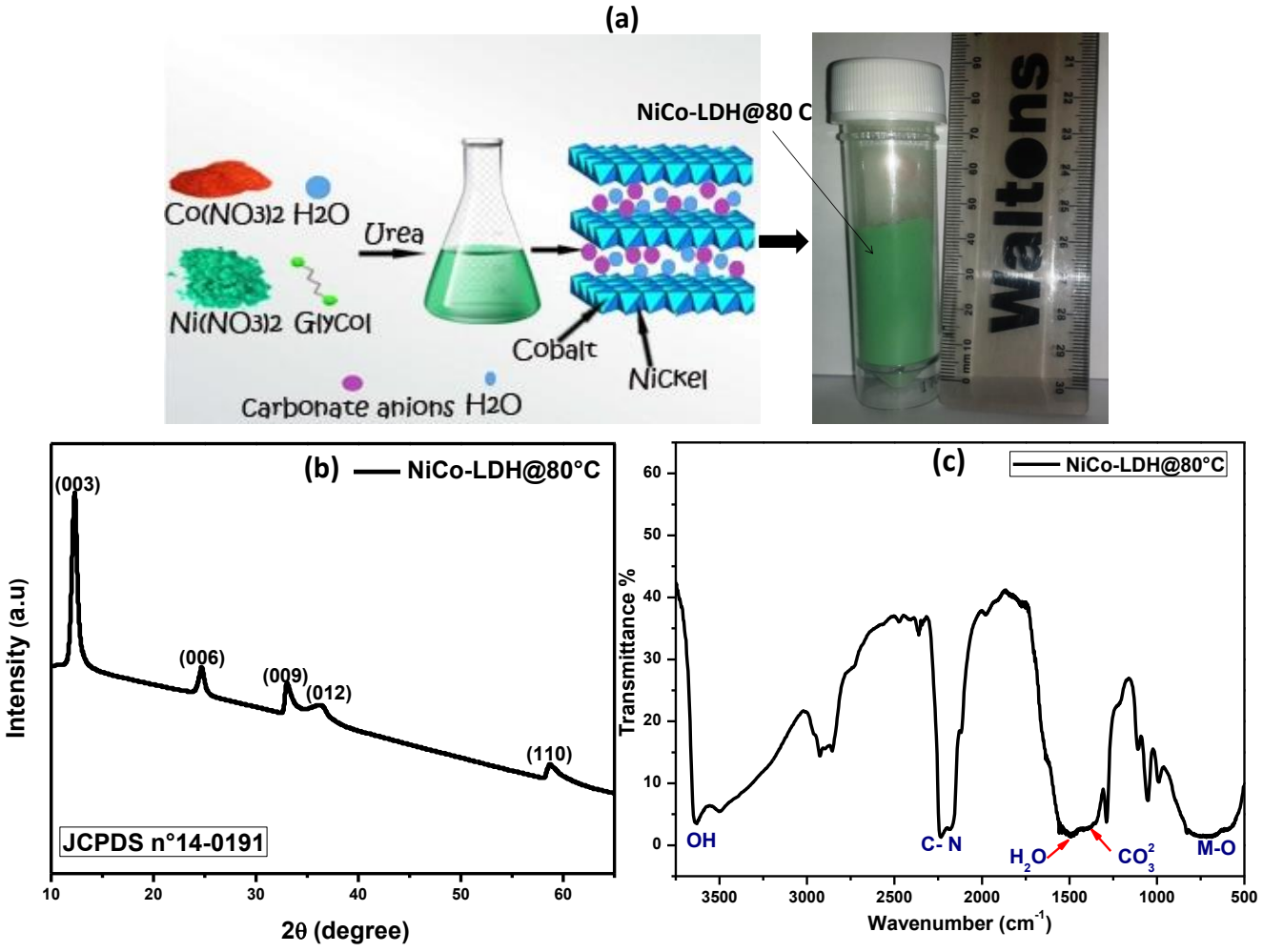

Figure 1. (a) Synthesis route, (b) XRD patterns and (c) FTIR spectrum of NiCo-LDH@80°C.

Fig. 1c displays the FTIR spectrum of NiCo-LDH@80°C which exhibited a broad peak around 3635 cm^{-1} assigned to O-H stretching vibrations related to water molecules and OH groups at the brucite-like layer and interlayer, following by a peak at 1500 cm^{-1} [8]. However, the peak at 1388 cm^{-1}

can be assigned to the vibration stretching of interlayer carbonate anions retained in the interlayer of LDH, while the peak at 638 cm^{-1} was ascribed to metal-oxygen (M-O) stretching and bending vibrations in the brucite-like lattice, confirming the existence of Nickel and Cobalt in the composite [13]. In addition, the peak located at 2241 cm^{-1} was assigned to the stretching vibrations of C≡N functional group.

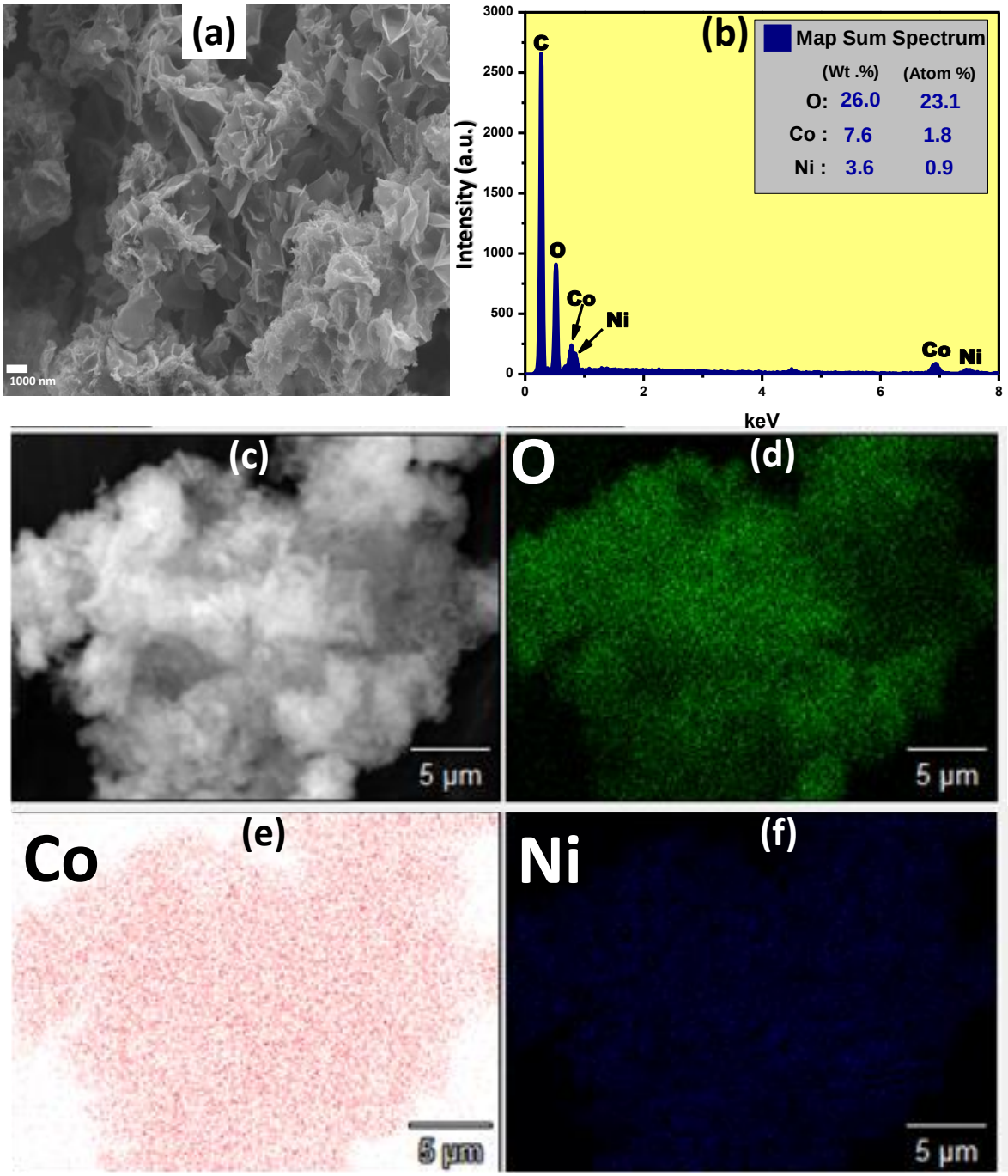

Figure 2. (a) FE-SEM micrograph and (b) EDS spectrum of NiCo-LDH@80°C. (c) FE-SEM image of the area used to conduct EDS mappings and (d-f) corresponding elemental mappings of O, Co and Ni.

The morphology of NiCo-LDH@80°C was characterized using SEM (Fig. 2a) which exhibited a good arrangement of nanosheets linked each other and presenting a structure like flowers. Moreover, Fig. 2b depicts the EDS spectrum of NiCo-LDH@80°C which revealed the presence of all expected chemical elements among which Nickel, Cobalt and Oxygen without impurities revealing the integrity of sample synthesis and handling. More interestingly, the distribution of all elements was relatively homogenous as revealed in Fig. 2(c-f). However, the detected carbon was due to carbon tape resulting from SEM sample preparation. Finally, it was found that the atomic ratio (Ni:Co = 1:2) was strictly in accordance with the initial weights.

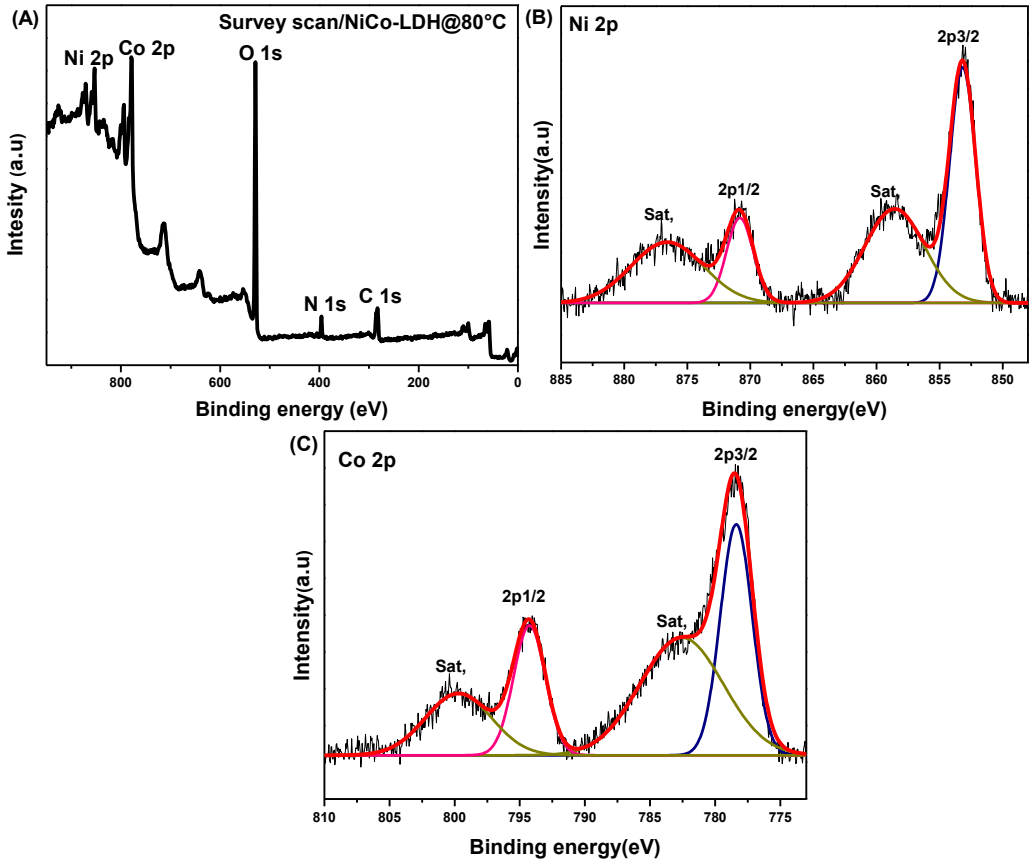

Figure 3. (a) XPS survey scan, HRXPS spectra of (b) Ni 2p and (c) Co 2p core-levels for NiCo-LDH@80°C.

To further investigate the surface composition and valence states XPS survey scan spectrum of NiCo-LDH@80°C (Fig. 3a) clearly demonstrated the coexistence of all expected elements which were Ni, Co and O. The XPS results are in accordance with the former EDS results presented and discussed above. On the other hand, high resolution XPS spectra were collected to get more insight on the valence states of elements on the surface. High resolution spectra of NiCo-LDH@80°C revealed that both Ni 2p and Co 2p were split into doublets due to spin-orbit splitting (Fig.3b and c) [9]. Fig. 3b presents Ni 2p core-level doublet showing a lower binding energy component Ni $2p_{3/2}$ at 853 eV and a well-defined satellite peak 858 eV of the binding energy (BE). The main peak located at 853 eV was

ascribed to metallic Ni which corresponds to Ni^{2+} due to the surface oxidation confirming that Ni^{2+} was present in the hydroxide material. Similarly, the Peak at 870 eV and 876 eV were assigned to Ni $2p_{1/2}$ and satellite, respectively [15, 16]. On the other hand, Fig. 3c displays Co 2p core-level spectrum of NiCo-LDH@80°C. As previously described for Ni 2p core-level Co 2p appeared as a doublet exhibiting peaks at 794 eV and 779 eV respectively assigned to Co $2p_{1/2}$ and $2p_{3/2}$ [17]. Finally, it is worth mentioning that the satellite peak observed at 784 eV is in accordance with the BE of Co^{2+} [9].

Electrochemical measurements were conducted to unveil the electrochemical performances of NiCo-LDH@80°C sample which was evaluated using a standard three-electrode system in 1 M Na_2SO_4 electrolytic solution. Fig. 4a shows the CV curves of NiCo-LDH@80°C at (5, 10, 20, 30 50, 75 and 100 mV/s). Surprisingly, the curves show nearly a symmetrical rectangular shape in the voltage window of 0.2-0.6 V, indicating the best capacitive behavior of as-synthesized NiCo-LDH@80°C. Consecutively, the overall capacitance was due to the dual contribution of both double-layer capacitance and pseudocapacitance. It is worth mentioning that the pseudocapacitive behavior observed in the scan range of 0.3 V-0.5 V could be attributed to the faradic redox reaction occurring between M-OH and M-O-O-H (with M representing the Ni or Co ions) [18]. Additionally, it should be pointed out that no inherent shape change due to the variation of the scan rate from 5 mV/s up to 100 mV/s was noticed, indicating high-rate performance and relatively high-current capability [19,20]. Interestingly, unlike Na_2SO_4 electrolyte the pseudocapacitive behavior was found to be much more pronounced for KOH electrolyte as shown in the cyclic voltammetry curves in Fig. 4c. To further quantify the electrochemical behavior of NiCo-LDH@80°C, the galvanostatic Charge/Discharge curves are displayed in Fig. 4b. The linear shape of the GCD curves indicates the ideal EDLC behavior of NiCo-LDH@80°C corresponding to the nearly rectangular shape observed in the CV profile. It is worth mentioning that the symmetric GCD curves reveal the high reversible characteristic of the reactions that occur at the electrode/electrolyte interface. Finally, the electrochemical investigation in KOH electrolyte revealed that NiCo-LDH@80°C exhibited a remarkably high pseudocapacitive behavior. This finding is in accordance with previous reports [9,21].

The specific capacitance (C_{sp}) of NiCo-LDH@80°C was calculated from CV curves using the equation (1) below and a record high specific capacitance of 2,140 $F.g^{-1}$ obtained at 5 mV/s.

$$C_{sp} = \frac{\int_{E_1}^{E_2} i(E)dE}{2(E_2 - E_1)\ mV} \quad (1)$$

Where C_{sp} is the specific capacitance ($F.g^{-1}$), $\int_{E_1}^{E_2} i(E)dE$ is total voltammetric charge which is the result of the integration of positive and negative sweep in the cyclic voltammogram. (E_2-E_1) is the potential window (V) of operation, m is the mass (g) of the active material after deposition of slurry and V is the scan rate (V/s) [22]. Interestingly, compared to previous reports available in the literature on NiCo-LDH supercapacitor electrode materials, our NiCo-LDH system exhibited higher specific capacitance than 79 % of them as illustrated in Table 1.

As depicted in Fig. 3d, electrochemical impedance spectroscopy (EIS) was carried out to further investigate the electrochemical properties of NiCo-LDH@80°C with Nyquist plot recorded in the range of 100 kHz to 100 mHz at the open circuit potentials. Ordinarily, the vertical slope in the

lower frequency range of the plot indicates low ionic diffusion resistance and charge transfer at the interface between NiCo-LDH@80°C electrode and electrolyte [23]. Finally, the slight semicircle is the result of a relatively low interfacial resistance in the system.

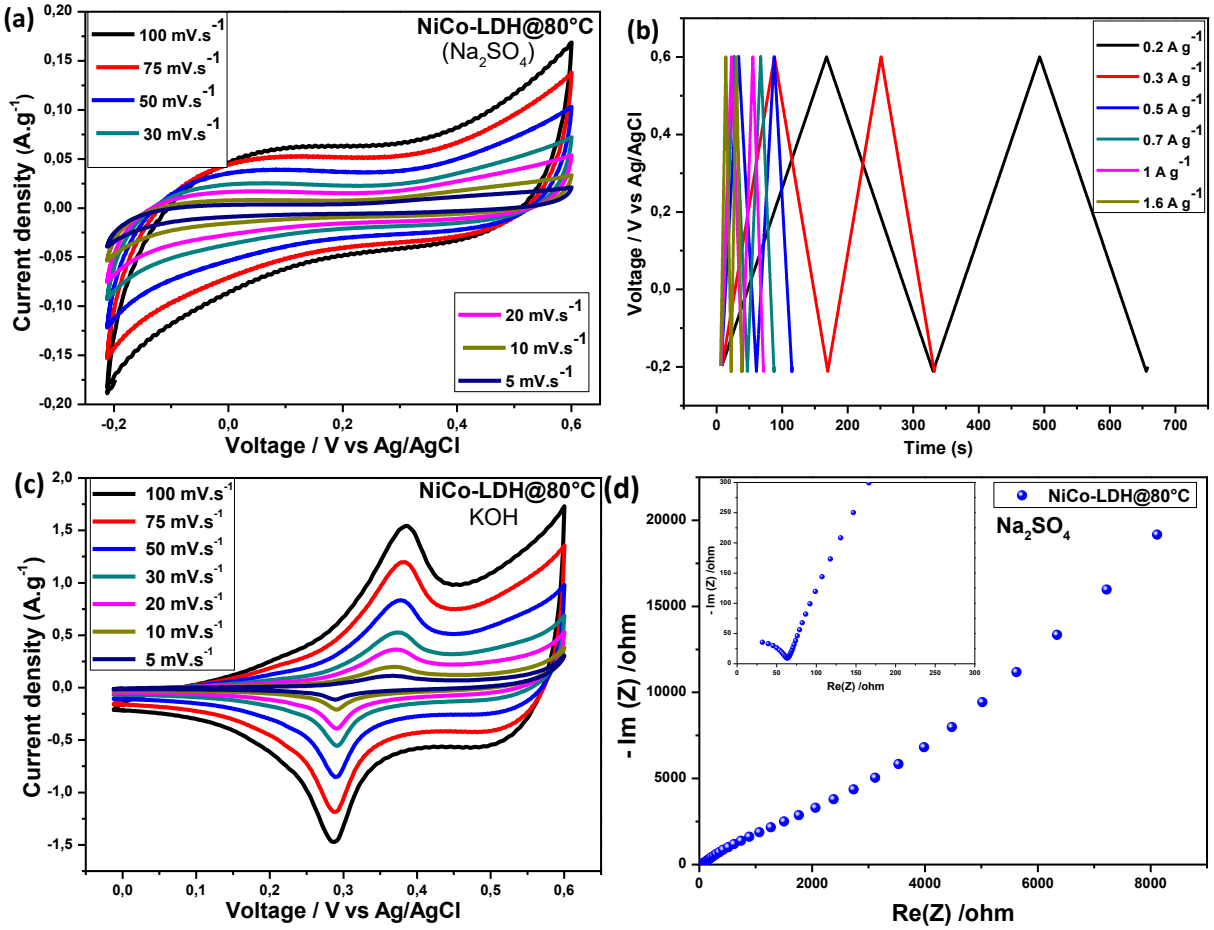

Figure 4. (a) CV curves of NiCo-LDH@80°C with various scan rates in 1 M Na_2SO_4 and (b) corresponding GCD at different current density; (d) Nyquist plots of NiCo-LDH@80°C and (c) CV profiles of NiCo-LDH@80°C 1 M KOH electrolyte.

Table 1. Specific capacitance performance of various NiCo-LDH based electrode.

Active material	Configuration	electrolyte	Specific Capacitance	References
(Ni,Co)Se2/NiCo-LDH//PC	2 electrode	3 M KOH	1224 F g-1	(24)
NiCoAl-LDH-NPs/CH-NWs //AC	2 electrode	6 M KOH	155.0 F g^{-1} (1.0 A g^{-1})	(25)
NiCo LDH nanoarrays	3 electrode	2M KOH	2391 F g^{-1}	(26)
PANI/NiCo-LDH	3 electrode	2 M KOH	1845 F g^{-1} (0.5 A g^{-1})	(27)
α-phase NiCo DH microsphere	3 electrode	6 M KOH	1120 F g^{-1} (1 A g^{-1})	(14)
GS/NiCo-LDH	3 electrode	6 M KOH	1980.7 F g-1 (1 Ag-1)	(19)

CNF@Ni-Co LDH NR/ NS	3 electrode	-	1378.2 F g^{-1} (1 Ag^{-1})	(23)
Ni50Co50-LDH	3 electrode	6 M KOH	1537 F g^{-1} (0.5 A g^{-1})	(13)
NiCo-LDH/RGO	3 electrode	3 M KOH	1911.1 F g^{-1} (2 A g^{-1})	(28)
NiCo-LDH@CNT/NF	3 electrode	1 M KOH	2040 F g^{-1} (1 A g^{-1})	(18)
NiCo-LDH/CFC	3 electrode	KOH-PVA (solid)	2762.7 F g-1	(9)
NiCo-LDH/Ag/NF hybrid	3 electrode	1 MKOH	2920 Fg^{-1} (5 Ag^{-1})	(29)
MnO_2@NiCo-LDH/CoS_2 nanocages	3 electrode	2 M KOH	1547 F g^{-1} (1 A g-1)	(30)
CoNiFe-LDH/CNFs	3 electrode	6 M KOH	1203 F g^{-1} (1 A g^{-1})	(31)
NiCo-LDH nanosheets	3 electrode	1 M Na_2SO_4	2140 F g^{-1}	This work

4. CONCLUSION

In summary, we successfully synthesized NiCo-LDH@80°C nanosheets via a facile up-scalable co-precipitation method. The XRD, EDS, XPS and FT-IR have confirmed the high crystallinity and stability of the as-synthesized materials. The electrochemical investigation of NiCo-LDH@80°C in 1 M Na_2SO_4 electrolyte resulted in a record high specific capacitance as high as 2,140 $F.g^{-1}$ (5 mV/s). Moreover, this method can be effectively up-scaled and extended to the synthesis of other LDH for various energy conversion and storage applications.

ACKNOWLEDGEMENTS
The authors are grateful to the University of South Africa (UNISA) for its generous financial support.

References

1. M.R. Lukatskaya, S. Kota, Z. Lin, M.-Q. Zhao, N. Shpigel, M.D. Levi, J. Halim, Pierre-Louis Taberna, M.W. Barsoum, P. Simon and Y. Gogotsi, *Nat. Energy,* 2 (8) (2017) 17105.
2. X. Xu, Y. Liu, P. Dong, P.M. Ajayan, J. Shen and M. Ye, *J. Power Sources,* 400 (2018) 96.
3. O. Jung, M.L. Pegis, Z. Wang, G. Banerjee, C.T. Nemes, W.L. Hoffeditz, J.T. Hupp, C.A. Schmuttenmaer, G.W. Brudvig and J.M. Mayer, *J. Am. Chem. Soc*., 140 (11) (2018) 4079.
4. M. Li, Y. Zhu, X. Ji and S. Cheng, *Mater. Lett*., 254 (2019) 332.
5. F. Li and X. Duan, Applications of layered double hydroxides. In: Duan, X., Evans, D.G. (Eds.), Structure and Bonding. Vol.119. Springer (2006), New York, NY, USA, pp.,193–223. http://dx.doi.org/10.1007/430-007.
6. J. He, M. Wei, B. Li, Y. Kang, D.G. Evans and X. Duan, Preparation of double layered hydroxides. In: Duan, X., Evans, D.G. (Eds.), Layered Double Hydroxides. Springer (2006), Berlin, pp. 89–119.
7. S. Gamil, M.A. El Rouby Waleed, M. Antuch and I.T. Zedan, *RSC Adv*., 9 (2019) 13503.
8. V. Rives, Layered Double Hydroxides: Present and Future. Nova Science Publishers (2001) New York, NY, USA.
9. T. Wang, S. Zhang, X. Yan, M. Lyu, L. Wang, J.M. Bell and H. Wang, *ACS Appl. Mater. Interfaces,* 9(18) (2017) 15510.
10. V. Prevot, C. Forano and J.P. Besse, *Inorg. Chem*., 37 (1998) 4293.
11. G.N. Pshinko, *J. Chem*., (2013) 347178.

12. L. Qin, M. Xue, W. Wang, R. Zhu, S. Wang, J. Sun, R. Zhang and X. Sun, *Int. J. Pharm*., 388 (2010) 223–230.
13. R. Li, Z. Hu, X. Shao, P. Cheng, S. Li, W. Yu, W. Lin and D. Yuan, *Sci. Rep*., 6 (2016) 18737.
14. J. Li, M. Wei, W. Chu, and N. Wang, *Chem. Eng. J*., 316 (2017) 277.
15. H. Li, S. Lu, J. Sun, J. Pei, D. Liu, Y. Xue, J. Mao, W. Zhu and Z. Zhuang, *Chem. Eur. J.,* 24 (2018) 11748.
16. Y. Pan, Y. Liu, J. Zhao, K. Yang, J. Liang, D. Liu, W. Hu, D. Liu, Y. Liu and C. Liu, *Mater. Chem*. A, 3 (2015) 1656.
17. J.-W. Kima, S.J. Lee, P. Biswas, T.I. Lee, J.-M. Myoung, *Appl. Surf. Sci.,* 406 (2017) 192.
18. X. Li, J. Shen, W. Sun, X. Hong, R. Wang, X. Zhao and X. Yan, *J. Mater., Chem. A*, 3 (2015) 13244.
19. Y. Tao, L. Ruiyi and L. Zaijun, *Mater. Res. Bull*., 51 (2014) 97.
20. J. Yana, Z. Fan, T. Wei, W. Qian, and F. We, *Carbon,* 48 (2010) 3825.
21. Y. Wang, D. Zhou, D. Zhao, M. Hou, C. Wang and Y. Xia, *J. Electrochem. Soc*., 160 (1) (2013) A98.
22. W. Chen, Z. Fan, L. Gu, X. Bao and C. Wan, *Chem. Commun*., 46 (2010) 3905.
23. F. Lai, Y. Huang, Y.-E. Miao and T. Liu, *Electrochim. Acta,* 174 (2015) 456.
24. X. Li, H. Wu, C. Guan, A.M. Elshahawy, Y. Dong, S. J. Pennycook, and J. Wang, Small, (2018) 1803895.
25. J. Yang, C. Yu, X. Fan and J. Qiu, *Adv. Energy Mater*., (2014) 1400761.
26. W. Zou, W. Guo, X. Liu, Y. Luo, Q. Ye, X. Xu and F. Wang, *Chem. Eur. J.,* 24 (1) (2018) 1.
27. X. Ge, Y. He, T. Plachy, N. Kazantseva, P. Saha and Q. Cheng, *Nanomaterials,* 9 (2019) 527.
28. X. Cai, X. Shen, L. Ma, Z. Ji, C. Xu, A. Yuan, *Chem. Eng. J*., 268 (2015) 251.
29. T. Guan, L. Fang, L. Liu, F. Wu, Y. Lu, H. Luo, J. Hu, B. Hu, M. Zhou, *J. Alloys Compd.,*799 (2019) 521.
30. X. Wang, F. Huang, F. Rong, Pe. He, R. Que, S. P. Jiang, *J. Mater Chem. A*, 7 (2019) 12018.
31. F. Wang, S. Sun, Y. Xu, T. Wang, R. Yu & H. Li, *Sci. Rep*. 7 (2017) 4707.

Journal of Nanosciences: Current Research

Kabongo et al., J Nanosci Curr Res 2018, 3:2
DOI: 10.4172/2572-0813.1000125

Review Article Open Access

Microwave Irradiation Induces Oxygen Vacancy in Metal Oxides based Materials and Devices: A Review

Kabongo GL[1,2*], Khawula TNY[1], Thokozani T[1], Nyongombe EG[3], Ozoemena K[1] and Dhlamini S[3]

[1]*Molecular Sciences Institute, School of Chemistry, University of the Witwatersrand, Johannesburg 2050, South Africa*

[2]*Department de Physique, Universite Pedagogique Nationale, Republique Democratique du Congo*

[3]*Department of Physics, University of South Africa, South Africa*

[*]**Corresponding author:** Guy Kabongo, Molecular Sciences Institute, School of Chemistry, University of the Witwatersrand, **Johannesburg**, South Africa, Tel: +27713392577; E-mail: Guy.Kabongo@wits.ac.za, geekale@gmail.com

Received date: July 5, 2018; **Accepted date:** August 9, 2018; **Published date:** August 17, 2018

Abstract

A mini-review of defects formation and engineering in energy and sensor materials through intentional doping and microwave irradiation is presented. Intensive research interest has been observed in the development of Transition Metal Oxides (TMOs) energy and sensor materials for industrial applications such as energy generation, energy storage and sensor devices. A variety of selected notable reports are organized into sections depicting structural, microstructural, luminescent and electronic properties of TMO materials and devices, regardless of their deep synthetic chemistry. There are three types of Oxygen Vacancies (VO) related to TMO materials among which neutrally ionized V 0, singly ionized Vo^{1+}, and doubly ionized Vo^{2+}. Oxygen vacancies (V) have been characterized using several experimental techniques such as X-ray diffraction, Thermo-Gravimetric Analysis (TGA), Ultra-Violet Visible Spectroscopy (UV-Vis), Photoluminescence (PL) spectroscopy, Raman spectroscopy, Electron Spin Resonance (ESR), Electron Energy Loss Spectroscopy (EELS) and X-ray Photoelectron spectroscopy (XPS). High resolution XPS O 1s core levels analysis is one of the most accurate analytical techniques to characterize VO in conjunction with other techniques. The deconvolution of O 1s core levels using a Gaussian function into three peaks Lattice oxygen (OL), surface hydroxyl oxygen (O-OH) and adsorbed oxygen (OS) has been widely used to correlate XPS to XRD, UV-Vis, PL and Raman data. This review summarizes the representative reports of VO formation via intentional doping or microwave irradiation in TMOs.

Keywords: Oxygen vacancies; TMOs; Doping; Microwave; Energy materials; Sensors

Introduction

Over the past two decades, oxygen vacancies (VO) have been widely reported to dramatically alter structural, luminescent, catalytic and electronic properties of materials applied in a variety of applications such as energy, sensors and display technologies [1-9]. These defects classified as point defects are till now the subject of a hot controversy on their natural origin among the scientific community worldwide due to the inherent challenges related to materials synthesis and characterization management in the vast majority of experimental fields. Oxygen vacancies exist in three states, namely neutrally ionized V_0, singly ionized V^{1+} and doubly ionized V^{2+}, the first and the former are stable (10,11) (Figure 1). Hitherto, fundamental studies have been devoted to elucidate the factors characterizing point defects, most of them have been investigated by first principle calculations [11,12]. The main factors are the formation energy and defect concentration, the former is well described in thermodynamic equilibrium by a Boltzmann distribution while at the same time it is closely related to the formation energy, defects with high formation energy are formed in low concentration [11]. The formation energy of point defects should not be considered as a constant due to its dependence to growth conditions. Previous studies have revealed that the formation energy of an oxygen vacancy depends on the abundance of the parent atoms found in the material and becomes more complex when the oxygen vacancy is charged because of the non-negligible effect of the electron chemical potential [11].

The major role of oxygen vacancy on the modification of electronic properties of materials has been discussed in a considerable volume of reports from fundamental studies to experimental investigations. The key fields of interest are primarily energy, secondly sensors and luminescent materials. In all these fields, TMOs have demonstrated exceptional performances, among them ZnO, TiO_2, NiO, MnO, CdO, Fe_2O_4, SnO_2, Co_3O_4 [13-53] are gaining momentum. However, fewer have successfully achieved intentional doping using foreign atoms to control intrinsic materials properties [49-51,54].

More importantly, innovative bi- and tri-metallic multifunctional nanostructure and heterostructure materials have been designed and constructed to achieve extraordinary device performances in selected topics such as reticular chemistry, electrochemical double-layer capacitors (EDLC), pseudo-capacitors, electrochemical sensors, white light emitting devices, solar cells, lithium-ion batteries, lithium-sulfur batteries, photoelectrochemical cells and gas sensors [55-66].

The growing interest in device's performance engineering stems among others from the possibility to intentionally tailor and control their oxygen vacancy content. To achieve such goal there is a critical need to judiciously undertake synthesis and characterization of materials to be investigated in clean environment and also deeply understand the effects of sample treatment on its lattice structure properties. To date several factors have been identified to remarkably alter the lattice structure properties of TMOs, among the major are the

pressure, temperature and gas treatment environment. Moreover, the exposure time to electromagnetic radiations sources such as Deep UV lamps, induction sources, and microwave reactors have been found to also contribute to the alteration of materials primitive lattice structure. It should be noted that these lattice structure alterations may have non- negligible direct contribution to the variation of oxygen vacancy content as it can be achieved elsewhere from simple conventional doping processes. Owing to the close correlation between materials lattice structure and electronic band-structure properties, one should have a precise understanding of the material band-structure in order to constructively and optimally describe research observations and findings.

Through structural doping the formation of oxygen defective sites has been successfully achieved, while the resulting tensile strain was revealed by the expansion of material lattice structure [67]. In fact, X-ray diffraction analysis of the lattice structure quality and crystallographic fingerprint may lead to the detection of possible alteration of the lattice structure resulting from foreign atoms insertion [68]. In their report, Kaur et al [68] demonstrated that doping a transition metal oxide host material with foreign atoms resulted in a tensile strain observed from XRD peak shift toward lower angles which leads to better materials properties later on. Moreover, the slight alteration observed in the lattice structure may have dramatic impact in the materials performance enhancement or degradation, depending of the targeted application.

Interestingly, Kumar et al. [69], have recently achieved lattice structure expansion via microwave irradiation, this process leads to the realization of high performing electrochemical spinel cathode materials for energy storage applications. Likewise, Mesfin et al. [70] and Jafta et al. [71] reported the same phenomenon and achieved exceptional electrochemical properties. Several factors have been identified by these authors to be responsible for these unique observations but oxygen vacancy increase should be seriously considered as the most plausible cause from a fundamental understanding [71].

Hence, the selection of a particular material synthetic method is of particular importance to the formation and careful control of oxygen vacancy. To date synthesis assisted with microwave treatment has proven to be one of the most effective approaches to meet such performance [70,71]. Microwave irradiation has demonstrated numerous advantages over other conventional materials processing such as fast and effective heating during chemical reactions, high product yield and environmental benign [72-74]. During microwave irradiation, a direct diffusion of electromagnetic wave energy to the material occurs via molecular interaction with the electric and magnetic field vectors of microwaves generated by a magnetron which produces waves in the frequency range of 300 MHz - 300 GHz (λ:1m-1mm) (Figure 2). It is plausible that during the interaction of microwaves with the material nonequilibrium processes occur, the formation of oxygen deficient sites are then promoted in the material lattice structure consecutively to entropy-driven desorption of lattice oxygen in the lattice structure [75,76] (Figure 3). Seminal studies have established that TMOs are among the best microwave absorbers and that their electrical resistance decreases with temperature increase and that microwave energy heats TMOs better than metals due to their low electric field penetration [77].

This review covers recent studies that focus on spectroscopic investigation of the versatile effects of oxygen vacancy on intrinsic properties of TMO materials for energy conversion, energy storage, sensors and solid state lighting. Special attention was devoted to XPS O 1s core level analysis of oxygen vacancy using GAUSSIAN function deconvolution.

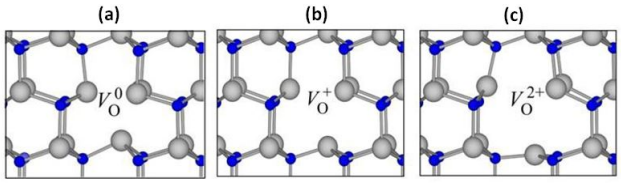

Figure 1: Local Atomic relaxations domain of oxygen vacancy in the (a) neutrally, (b) singly and (c) doubly ionized states. Reproduced with permission from ref. [78]. Copyright 2009 IOP publishing ltd.

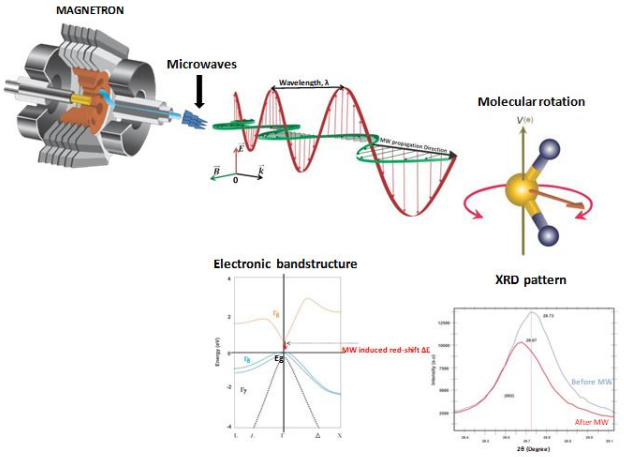

Figure 2: Proposed schematic diagram describing the mechanism of oxygen vacancy formation via microwave irradiation and its effect on lattice structure and electronic band- structure. Eg and ΔE represent the energy gap and the quantified red-shift resulting from microwave irradiation which is shown by the red arrow.

Formation of Oxygen Vacancy

Structural doping

In a recent study, it has been demonstrated that using dopants one can tune oxygen vacancy in TMO base devices, precisely studies revealed that p-type dopants introduced holes into the system to lower significantly the formation energy of oxygen vacancy [85]. Several other methods have been successfully used to dope transition metal oxide based materials and devices and hence generate oxygen vacancies, such as combustion synthesis, solution- combustion, solid state reaction, sol-gel [86-88], co-precipitation, hydrothermal [89], sonochemical, chemical vapor deposition, plasma enhanced chemical deposition, RF magnetron sputtering, evaporation, electrochemical synthesis, spin coating, spray pyrolysis, and spray coating, etc. Park et al. [90] have successfully doped ZnO with Co^{2+} ions and remarkably analyzed the variation of VO in the undoped and Co-doped ZnO samples via Maximum entropy method (MEM) using electron density distribution derived from Rietveld refinement. The authors found that

the ZnO unit cell volume was increased with Co^{2+} doping concentration and that consecutively the amount of VO increased up to a certain limit before dropping for higher doping concentration. The author faced a challenge to completely assigned the abrupt increase observed in the lowest Co^{2+} doping concentration and stated that further analysis were needed. It is plausible that Co^{2+} ions may have reached its saturation limit in the ZnO crystal lattice below 5 mol% and above 1 mol% and this could not lead to a continuous increase in VO content probably due to the segregation of Co^{2+} ions which are very likely to have formed islands of dopants in the crystal lattice instead of bonding.

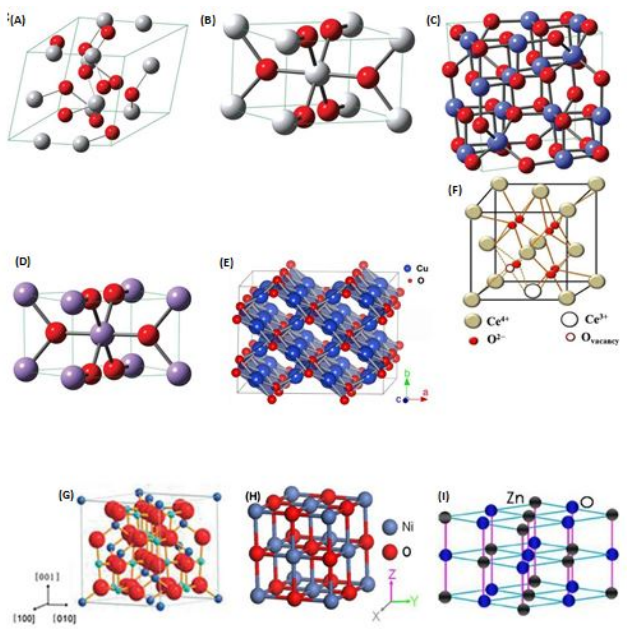

Figure 3: The crystal structures of (A) TiO_2, (B) Cr_2O_3, (C) V_2O_3, (D) MnO_2. Reproduced with permission from ref. [79]. Copyright 2015 The Royal Society of Chemistry. (E) Refined Crystal structure of the CuO unit cell. Reproduced with permission from ref. [80]. Copyright 2014 Springer Nature Publishing Group. (F) Schematic model of the CeO_2 structure showing Ce^{3+}-ions and oxygen vacancy. The whitish color ball is Ce^{4+}; the red color ball is O^{2-} on the lattice site; the red color circled ball is oxygen vacancy; the unfilled white ball represents Ce^{3+} on the lattice site formed after removing oxygen either from surface or from the interior of CeO_2. Reproduced with permission from ref. [81]. Copyright 2017 Springer Nature Publishing Group. (G) Atomic configurations for the unit cell of spinel Co_3O_4. Reproduced with permission from ref. [82]. Copyright 2014 The Royal Society of Chemistry. (H) The cubic NiO crystal structure. Reproduced with permission from ref. [83]. Copyright 2015 Elsevier Ltd (I) A schematic representation of wurtzite ZnO crystal structure. The Zn and O atoms are marked as well in the schematic with ash and blue circles, respectively. Reproduced with permission from ref. [84]. Copyright 2007 The American Institute of Physics.

Microwave irradiation

Material and device properties have been successfully tailored via microwave irradiation in a very recent past [81,91-92]. Microwave irradiation is a rapid and efficient heating way for highly homogenous materials processing which is eco-friendly and easy to manipulate as compared to conventional synthetic approaches. This approach has been used for large scale and cost- effective synthesis of supercapacitor electrode materials at desired temperatures up to 1500°C and controlled pressure (≤ 199 bar) at relatively short reaction time [93]. This technique has been used independently or in conjunction with other processing methods to complement them and achieve high yield innovative materials in the so-called microwave-assisted synthesis [94-102]. In a seminal research work, Newnham and co-workers investigated the microwave-matter interactions ; they reported that subjecting a material to microwave which has two vector components, namely, magnetic and electric field which induces in the material an electric polarization $P(C/m^2)$ equivalent to the dipole moment (C^{-m}) per unit volume (m^{-3}), hence generating thermodynamic nonequilibrium entropy mechanism [77]. The authors identified several polarization mechanisms in solids among which three major leads to loss in the microwave region, namely, space charges arising from localized electrical conduction, rotating electrical dipoles and ionic polarization associated with far-infrared vibrations [77].

Characterization of Oxygen Vacancy

Several analytical techniques have been used to characterize oxygen vacancies in transition metal oxides, namely, X-ray diffraction (XRD), Thermo-Gravimetric Analysis (TGA), Ultra- Violet Visible Spectroscopy (UV-Vis), Photoluminescence (PL) spectroscopy, Raman spectroscopy, Electron Spin Resonance (ESR), Electron Energy Loss Spectroscopy (EELS) and X-ray Photoelectron spectroscopy (XPS) [9,90,103-108]. The detailed analysis of XPS O 1s core level which consist of GAUSSIAN function deconvolution has been widely accepted among the analytical techniques used to qualitatively analyze VO and was carefully adopted to get more insights into O 1s medium peak located at ~531 eV presented in Figure 4ab. This peak has been ascribed to surface hydroxyl oxygen (O-OH) related to O^{2-} ions that are localized in the oxygen deficient regions within the ceramic lattice [109,110]. Moreover, Yoshida et al. successfully investigated the effect of microwave irradiation on electronic band-structure of ZnO via absorption and emission spectroscopy (92). The authors systematically demonstrated via PL spectroscopy that microwaves generated a new deep level defect which lowers the bandgap of ZnO as illustrated in Figure 4cd, and they assigned this defect level to zinc and oxygen plasma or to the thermal effect induced by microwave. However, particular attention should be given to the former assertion because the nonequilibrium processes resulting from thermal effect may have created oxygen vacancies which can be described via energy band-structure as shown in Figure 4e. It is important to note that for detailed quantitative analysis of oxygen vacancy Rutherford backscattering spectroscopy and X-Ray absorption spectroscopy using synchrotron radiation are more appropriate [111,112].

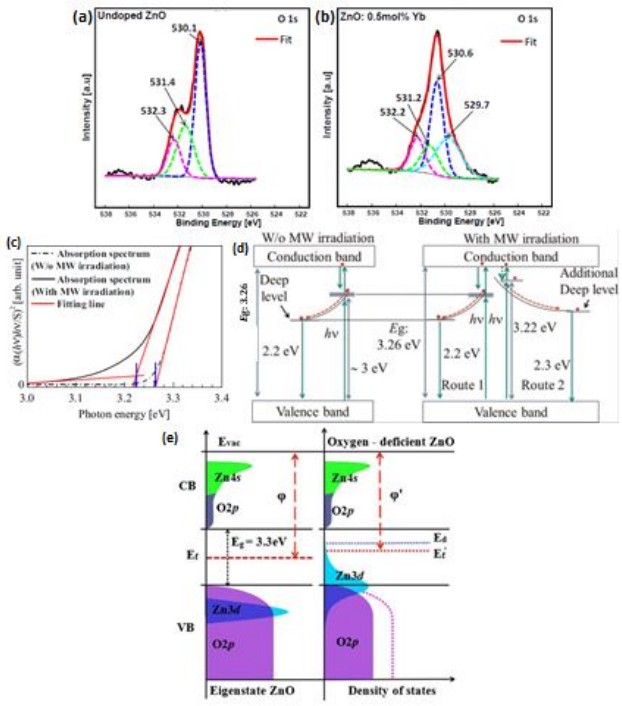

Figure 4: Deconvoluted XPS O 1s core level for (a) undoped and (b) Yb3+-doped ZnO Reproduced with permission from ref. (86). Copyright 2014 Elsevier Ltd. (c) Bandgap electronic structure and corresponding (d) energy band diagram at room temperature for microwave (MW) irradiated and non-irradiated ZnO Reproduced with permission from ref. (92). Copyright 2015 Elsevier Ltd. (e) Electronic energy band structure of eigenstate and oxygen-deficient ZnO, the pink dotted line represents the density of states of O 2p before the reduction, the orange bidirectional arrow indicates the work function (φ, φ′), the oxygen atoms are lost and unshared Zn 3d states move towards the CB to form a donor level (Ed), Evac and Ef are the vacuum level and the Fermi level, respectively. Reproduced with permission from ref. (25). Copyright 2017 Elsevier Ltd.

Oxygen Vacancy Enhanced Electrochemical Performances for Energy Storage

Very recently exceptional class of materials have been uncovered, these multifunctional materials have tremendous advantages and exceptional performances in energy storage applications, namely, Layered-Double Hydroxides (LDHs), Metal Organic Frameworks (MOFs), Multishelled and nanostructured materials; among various morphologies obtained hollow-spheres are the most efficient in energy storage [113-116].

Oxygen vacancy plays an important role in tuning the physico-chemical properties of these innovative materials applied in supercapacitors, lithium ions batteries, lithium sulfur batteries, sodium ion batteries, magnesium ion batteries and zinc air batteries. Some of these innovative materials were produced via microwave assisted synthesis. Copper and Nickel have been associated to produce via microwave synthesis a Hollow-sphere MOFs material for enhanced lithium battery performances [117]. Moreover, the authors revealed that the matched composition of CuO@NiO resulted in an efficient step-by-step lithium insertion reaction which finally contributed to the excellent electrochemical properties as presented in Figure 5. Furthermore, the core-shell architecture allowed easy lithium/electron diffusion while the volume change was accommodated in the microsphere pores of the bimetallic oxides [117].

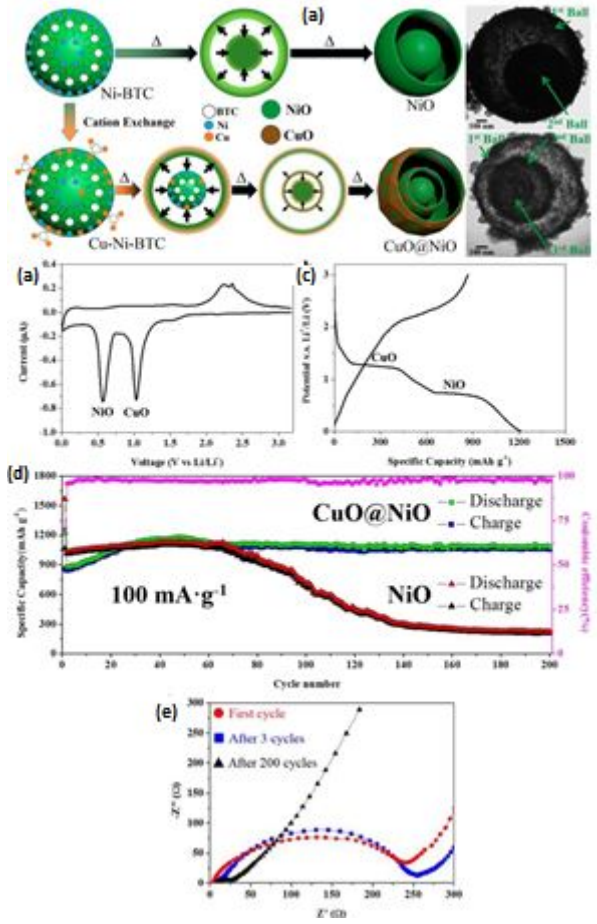

Figure 5: (a) Illustration of the cationic exchange process of metal organic framework (MOF) and its conversion to multi-layer hollow structure. Electrochemical performances of multilayer CuO@NiO spheres: (b) cycle voltammogram profile, (c) first cycle discharge (lithium insertion) and charge (lithium extraction) curve, (d) cycling performance at a current of 0.1 $A.g^{-1}$, and (e) Nyquist plots for the first, third and 200 cycles. Reproduced with permission from Ref. [117]. Copyright 2015 The American Chemical Society.

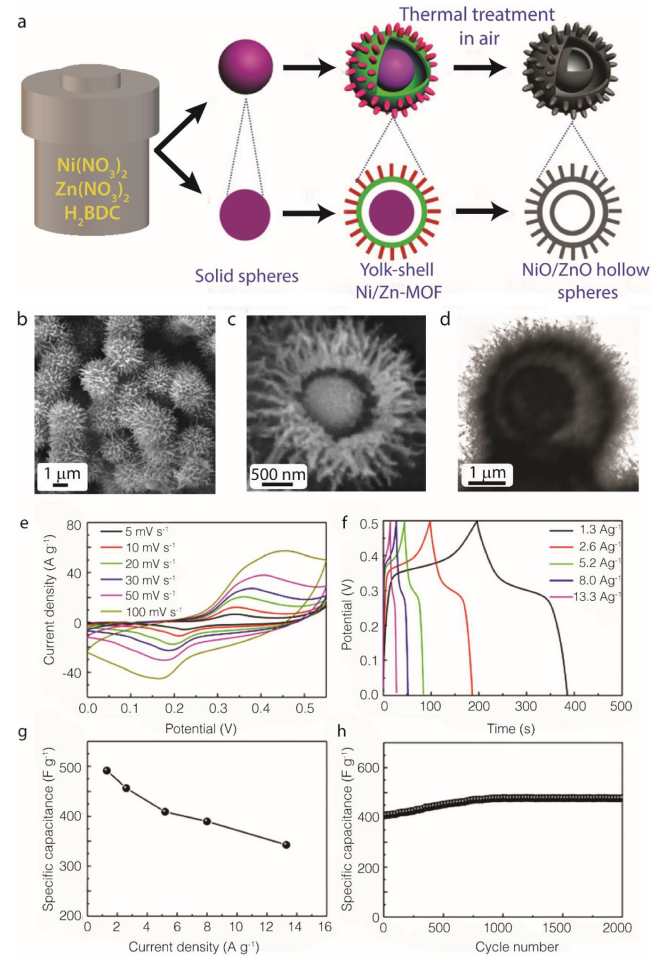

Figure 6: (a) Schematic illustration showing the formation of the yolk-shell Ni/Zn-MOF microspheres and double-shelled NiO/ZnO hollow spheres. (b) Low- and (c) high-magnification SEM images of the Ni/Zn-MOF microspheres. (d) TEM image of the double-shelled NiO/ZnO hollow spheres. (e) Cyclic voltammetry (CV) and (f) galvanostatic charge-discharge (GCD) curves of the NiO/ZnO electrode at different current densities. (g) Corresponding specific capacitance of NiO/ZnO electrode calculated by the GCD curves. (h) Cycle performance of NiO/ZnO electrode at a current density of 5.2 A.g^{-1} for 2000 cycles. Reproduced with permission from Ref. [120]. Copyright 2017.

The concept has been widely adopted and improved by several groups using different combination of TMOs and organic linkers to achieve better storage properties in supercapacitors and batteries as presented in Figures 6 and 7, respectively. In the same spirit, Li et al. produced NiO/ZnO hierarchical double-shelled hollow spheres with exceptional cycling stability up to 117% after 2000 cycles at a current density of 5.2 A.g-1 [118]. Bruce Dunn group on the other hand remarkably demonstrated the strategic influence of oxygen vacancy on faster promotion of charge storage kinetics which makes it easy for Li ions intercalation and de-intercalation [9]. That leads to enhanced capacity up to ~ 320 mA hg^{-1} as shown in Figure 8. Teng Zhai and co-workers have exceptionally demonstrated that oxygen vacancies could enhance both conductivity and capacitance of nanorods based wearable asymmetric supercapacitor [119]. The remarkable strategy consisted of a simple hydrogenation treatment of MnO2 electrodes which displayed exceptional rate capability and cycling with only a moderate concentration of oxygen vacancies [119].

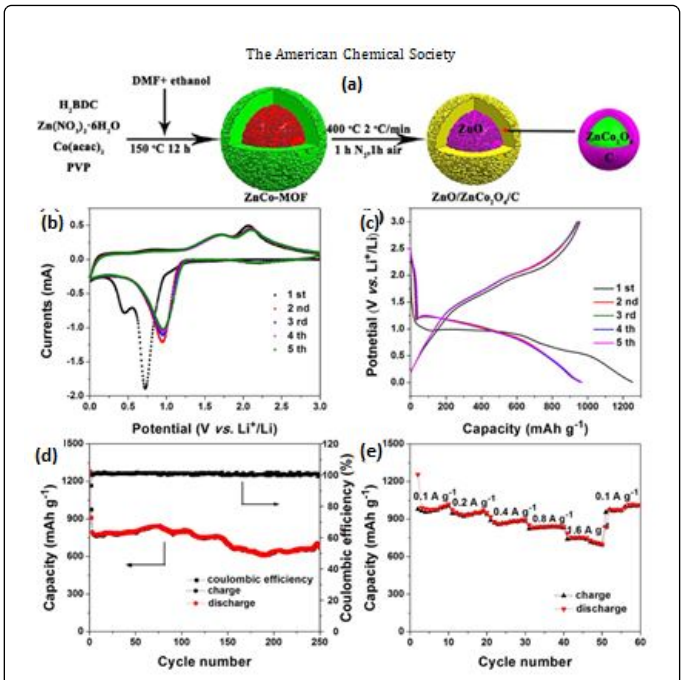

Figure 7: (a) Formation Process of Core/Shell ZnO/$ZnCo_2O_4$/C Nanospheres (b) CV curves at a scan rate of 0.1 mV s^{-1} in the voltage range of 0.01-3.0 V. (c) Charge/discharge profiles at a current density of 0.1 A.g^{-1}. (d) Cycling performance at a current density of 0.5 A.g^{-1}. (e) Rate capabilities of ZnO/$ZnCo_2O_4$/C anode. Reproduced with permission from Ref. [121] Copyright 2015 The American Chemical Society.

Oxygen Vacancy Dynamic in Photovolatiac Solar Cells

The increasing demand of clean and environmental benign energy production sources is today in the heart of public and private sector research institutes strategy development plans worldwide due to environmental concerns related to conventional energy sources based on fossil fuels and CO_2 production. Researchers are currently driven to achieve innovative solutions to the betterment of mankind life through the development of pollution-free energy sources such as photovoltaic solar cells. Regardless of the type of mechanism exploited to generate and dissociate electron-hole pairs in solar cells, TiO_2 has been extensively used as a counter electrode and also a hole conducting layer mainly in quantum dot and dye-sensitized solar cells [122-130]. In an astonishing investigation Su et al. [131] have for the first time experimentally demonstrated using Electron Paramagnetic Resonance (EPR) that oxygen vacancy could modulate photoelectrical conversion efficiency in a TiO_2 dye-sensitized solar cell grown via hydrogenation at low temperature and mild pressure. Their exceptional findings are summarized and presented in Figure 9. The effect of oxygen vacancy on the band gap corroborates the results found in previous studies [25]. Microwave synthesis has been used to synthesize highly crystalline TiO_2 with a shorter treatment time as compared to conventional heating sources when used in solar cells application

[132]. Hence, microwave heating has been demonstrated to be more efficient than conventional heating sources such as muffle furnace, nowadays a worldwide clue. Recently Ghosh and co-workers [133] have systematically designed and fabricated via microwave a high efficient counter electrode based on CuxS and grapheme oxide for quantum dot sensitized solar cells. Owing to the challenges involved in photoanode operation, particular care was devoted to its design in order to effectively reduce the oxidized electrolyte, hereafter achieving a 6.81% record efficiency of which corresponding results are depicted in Figure 10.

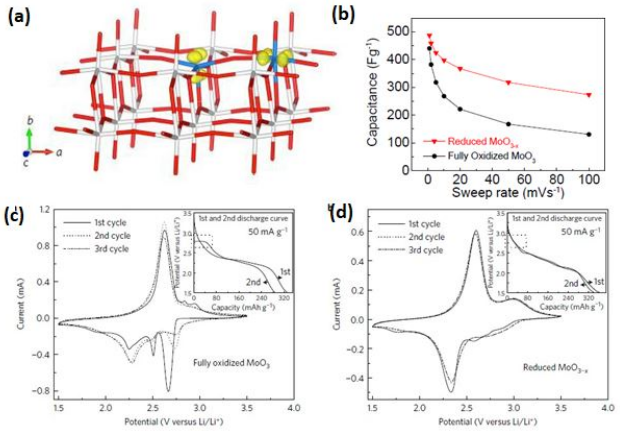

Figure 8: (a) The most stable oxygen vacancy configuration and polaron formation in R-MoO^{3-}_x calculated from DFT. The Mo^{5+} ions are highlighted with blue. (b) Sweep rate dependence on capacitance, (c) and (d) Cyclic voltammetry of the first three cycles at 10mVs^{-1} and galvanostatic discharge curves (insets, at 50 mA.g^{-1}) in F-MoO_3 and R-MoO^{3-}x, respectively. Reproduced with permission from ref. (9). Copyright 2016 Macmillan Publishers Limited, part of Springer Nature.

Sensor Sensitivity Derived Oxygen Vacancy

From medical applications, namely, diseases detection and environmental protection in the mining sector, there are rooms for improvements. The growing momentum observed in the design and fabrication of electrochemical, gas and chemical sensors drive researchers and technologists to meet the agenda of the next generation of sensor devices which are sought to be flexible, highly selective and sensitive than ever. TMOs based sensors have been widely investigated for the past two decades and a lot of issues related to their practical application have been exposed and much still need to be done for easy and safe domestic usage. Among the vast majority of synthetic methods used to produce TMOs, microwave has a place of choice due to the extraordinary variety of materials morphology which also exhibit unique physic-chemical properties such as high surface area and exceptional conductivity to cite few. It should be noted that oxygen vacancy plays a critical role in materials conductivity as demonstrated by several authors (9,25,92).

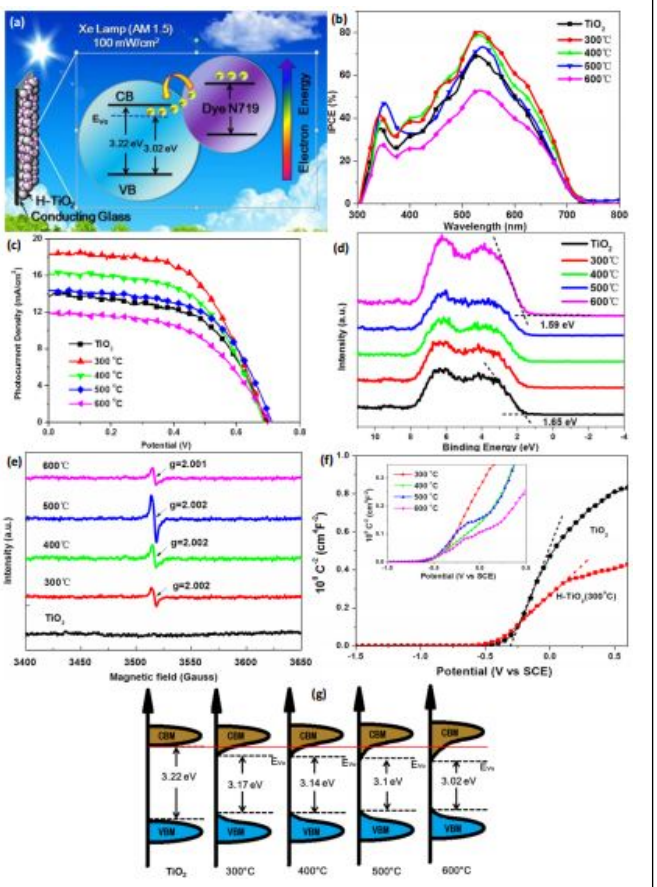

Figure 9: (a) Charge transfer mechanism for photoanode-modified DSSC based on H-TiO_2. (b) IPCE spectra of DSSCs based on TiO_2 and H-TiO_2 annealed at different temperature. (c) Photocurrent-photovoltage curves under illumination (d) Valence band of TiO_2 and H-TiO_2 treated under different temperatures. (e) EPR spectra recorded at 300 K for TiO_2, H-TiO_2 samples. (f) Mott-Schottky plots collected in the dark for the TiO_2 and the H-TiO_2 nanopowders. Inset Figure: Mott-Schottky plots of HTiO_2 nanopowders prepared at 300°C, 400°C, 500°C, and 600°C, which was collected under the same conditions. (g) Schematic diagrams of electronic band structure of TiO_2 and H-TiO_2. EVo located below the TiO_2 conduction band represents the energy levels of oxygen vacancy. Reproduced with permission from ref. [131]. Copyright 2015 The American Chemical Society.

From a fundamental point of view, it is well agreed that the targeted metal oxide sensors resistance modulation is the result of a surface mechanism of oxidation-reduction reaction (ORR) involving chemisorbed oxygen with the molecules of the detected gases [134]. This implies that there exist in metal oxides based sensors a relative correlation between their sensitivity and the concentration of surface adsorbed oxygen [134]. In the same spirit, several authors have reported results in agreement of this understanding, and in particular it should be pointed out that the samples investigated in these studies were produced via microwave-assisted synthesis [89,135-139].

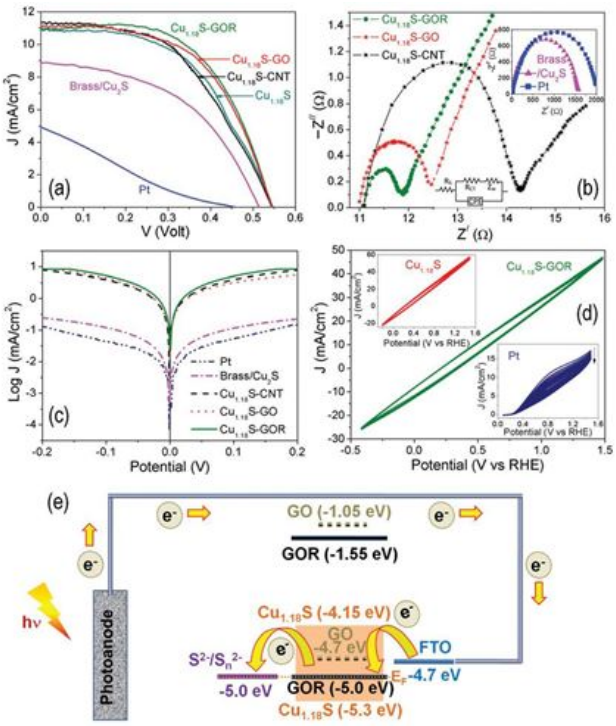

Figure 10: (a) J-V characteristics, (b) Nyquist plot and (c) Tafel polarization characteristics of Pt, brass/Cu_2S and Cu1.18S composites with 10 wt% CNT, GOR and GO. (d) Stability tests: 50 cycles of CV plots for Cu1.18S-GOR as the working electrode in a three electrode cell. The insets show the CV plots of the Cu1.18S working electrode for 50 cycles and Pt for 10 cycles, with an arrow showing the downward shift in current density over an increasing number of cycles. (e) Energy band diagram (not to scale) of Cu1.18S-GOR CE showing electron transfer. The energy levels of GO are also indicated. Reproduced with permission from ref. [133]. Copyright 2016 The Royal Society of Chemistry.

Via oxygen vacancy modulation investigated using XPS, Wang and colleagues [134] enhanced sensing performance and mechanism of hydrogenated NiO particles. The innovative concept investigated based on hydrogenation consisted in increasing the density of unsaturated transition metal atoms with dangling bonds on the surface, this concept was investigated elsewhere using Raman spectroscopy [104]. In the study by Wang et al., for which the sensing reaction mechanism is described and presented in the Figure 11, the XPS analysis revealed that the relative amount (%) of oxygen vacancy increased with increase hydrogenated time as shown in Figure 11. The authors found reasonable to conclude that the sensing properties enhancement resulting from hydrogenation may originate from the increase of the relative percentage of OV and OC GAUSSIAN components in the XPS O 1s core levels and also the decrease in the amount of -OH group [134]. Due to its role on the electronic band gap decrease and conductivity increase discussed earlier in section 3, oxygen vacancy increase could be considered as the main factor responsible for enhanced sensing activity. The response and recovery along with the sensors resistance are summarized in the Figure 12.

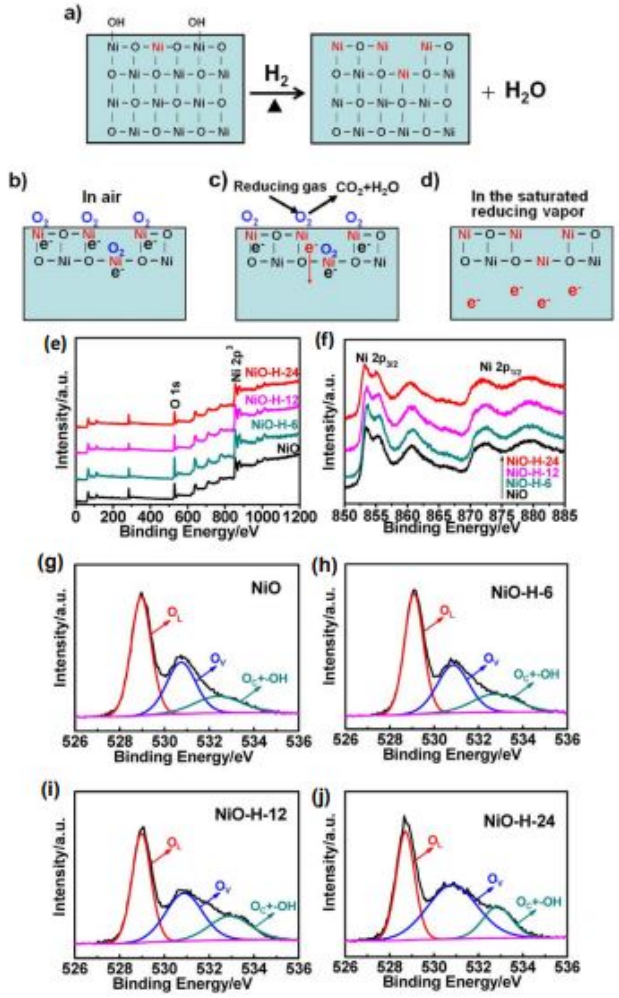

Figure 11: Schematic diagram of hydrogenation reaction of NiO particles. (b)-(d) Sensing reaction mechanism for NiO sensing materials. The letter Ni in red is unsaturated Ni atom with dangling bonds. Black e- and red e- represent the electron captured by O_2 and free electron, respectively. (For interpretation of the references to colour in this figure legend, the reader is referred to the web version of this article.).The survey spectra, (e) Ni 2p3/2, 2p1/2 and (f)-(i) O 1s spectra of the hydrogenated and non-hydrogenated NiO samples, (f) NiO, (g) NiO-H-6, (h) NiO-H-12 and (i) NiO-H-24. Reproduced with permission from ref. [134]. Copyright 2017 Elsevier Ltd.

Oxygen Vacancy Modulation for Efficient Control of Field Emission and Light Emitting Devices Properties

Since the past two decades, the display technology industry is experiencing a considerable investment of scientists and technologists to the realization of white light emitting materials and devices. It has been however demonstrated that controlling these devices calorimetric performances is closely dependent on their oxygen vacancy content [140-142]. A number of research groups have devoted their efforts to

synthesize these light emitting materials using microwave approach [143-146].

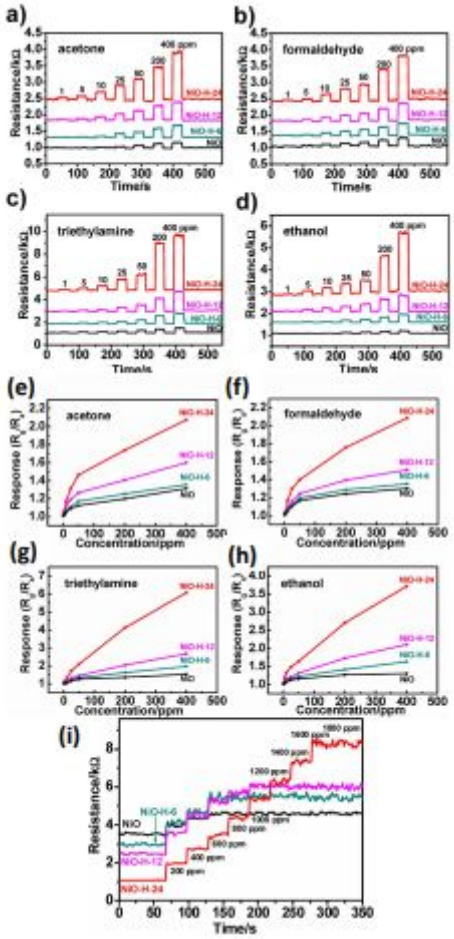

Figure 12: Response and recovery curves of the sensors based on the hydrogenated and non- hydrogenated NiO samples towards different concentrations of a) acetone, b) formaldehyde, c) triethylamine and d) ethanol at 350 °C and a relative humidity of 15-22%. (The relative humidity values were measured at 18-22 °C). The response curves of the sensors based on the hydrogenated and non-hydrogenated NiO samples towards different concentrations of (e) acetone, (f) formaldehyde, (g) triethylamine and (h) ethanol at 350 °C and a relative humidity of 15-22%. (The relative humidity values were measured at 18-22 °C). (i) The resistances of the sensors based on the hydrogenated and nonhydrogenated NiO samples in air and in different concentrations of ethanol vapor at 350 °C and a relative humidity of 15%. (The relative humidity value was measured at 24 °C. The concentrations labeled in this figure represent the injected concentration of ethanol each time.). Reproduced with permission from ref. [134]. Copyright 2017 Elsevier Ltd.

Two years ago a thorough investigation by Zhang et al. [147] was conducted to elucidate on the role of oxygen vacancy on the persistent luminescence of a terbium doped light emitting material. The investigators focused their effort on unraveling the origin of defects involved in the enhancement of persistent luminescence for samples annealed in an oxygen-poor atmosphere. They observed via thermoluminescence spectroscopy analysis that the increase of persistent luminescence was accompanied by oxygen vacancy content increase. Moreover, a comparison of defect energy levels was conducted between their experimental findings and theoretical calculations derived from Khon-Sham levels studies by Freysoldt and co-worker [148]. They proposed a re-evaluation of the theoretical result obtained for the depth of doubly charged VO2+ at 0.69-0.74 eV as compared to 1 eV below the conduction band [147]. In the same line, Xu et al. [149] investigated red phosphorescence of Sr_2SnO_4:Sm^{3+} phosphor successively sintered in air and 10^{-2} Torr vacuum atmosphere. The later treatment option contributed to the increase in oxygen vacancies amount which according to authors acted as the sensitizer and electron traps for effective energy transfer from the host matrix Sr2SnO4 to the dopant Sm3+. The findings of their study are summarized in Figure 13. Finally, remarkable enhanced phosphorescence properties were achieved by the authors after vacuum sintering process [149].

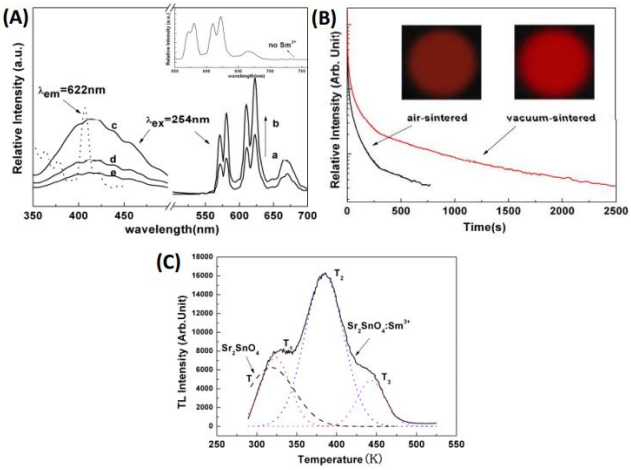

Figure 13: (A) Emission (λex = 254 nm) and excitation (λem = 622 nm) spectra of Sr_2SnO_4 and Sr_2SnO_4:Sm^{3+}. (a) is the emission spectrum of the air-sintered Sr_2SnO_4: Sm^{3+}. (b), (d) and inset are the emission spectra of Sr_2SnO_4: Sm^{3+} sintered in vacuum. (c) and (e) are the emission spectra of Sr_2SnO_4 sintered in vacuum and air, respectively. Left dash curve is the excitation spectrum of Sr_2SnO_4: Sm^{3+} sintered in vacuum. (B) Afterglow decay curves of Sr_2SnO_4: Sm^{3+} sintered in air and vacuum. Inset: long afterglow photographs of Sr_2SnO_4: Sm^{3+} sintered in air and vacuum. The photographs were taken in the darkroom for 1 min after the removal of the 254-nm ultraviolet lamp. (C) Thermoluminescence glow curves of the vacuum-sintered Sr_2SnO_4 and Sr_2SnO_4: Sm^{3+}. Reproduced with permission from ref. (149). Copyright 2010 The Optical Society of America.

In a very recent research work, Ai-Zhen Liao et al. [150] successfully increased field emission properties of a device based on α-Fe_2O_3 nanorod arrays via conductivity increase and work function decrease through polaronic hopping mechanism owing to oxygen vacancy. The significant findings of the study among which band-structure modification similarly reported by earlier authors are summarized in the Figure 14 shown below [25,92]. Unambiguously the investigation revealed according to the authors that oxygen deficient HNAs were potential candidates for nanoelectronic applications and more

precisely in cutting-edge field of electron emitter devices and flat panel displays [150].

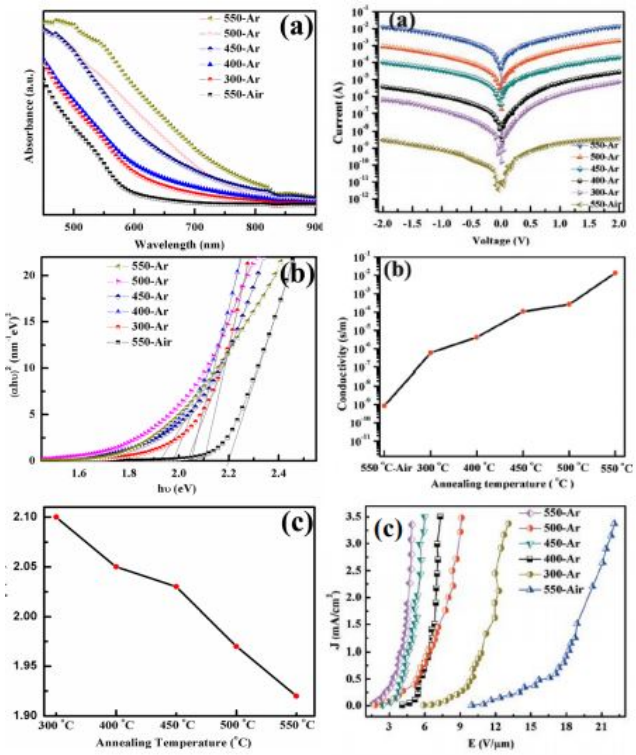

Figure 14: Left panel (a) UV-vis absorption spectra of the oxygen-deficient HNAs annealed at 300°C, 400°C, 450°C, 500°C and 550°C, respectively, and pristine HNAs annealed at 550°C. (b) Plots of (αhυ)2 vs (hυ) for these samples, from whose tangents we obtain (c) the corresponding variations of the band gap with annealing temperature. Right panel (a) I-V characteristics of oxygen-deficient HNAs annealed at 300°C, 400°C, 450°C, 500°C, and 550°C and pristine HNAs annealed at 550°C, and (b) the corresponding specific conductivity as a function. (c) J-E curves of pristine HNAs annealed at 550°C and oxygen-deficient HNAs annealed at 300°C, 400°C, 450°C, 500°C, and 550°C. Reproduced with permission from ref. [150]. Copyright 2016 The American Vacuum Society.

Conclusion

This mini-review paper provides an overview of microwave irradiation tuning of oxygen vacancy and its role in tailoring materials properties. The key performances of energy storage, sensor and light emitting materials have been widely assigned to oxygen vacancy. Various approaches have been reported to account for oxygen vacancy control among which microwave irradiation is one of the most accessible and cost effective. It has been demonstrated that at some extent oxygen vacancy increase is responsible of the p-type conductivity observed in these materials and plays a considerable role in the exceptional performances documented in the literature. Due to thermodynamic nonequilibium processes that occur during microwave irradiation which contribute to the formation of oxygen deficient sites in the lattice structure, microwave treatment should be considered as an effective approach to boost electrochemical, sensing and optical properties via protonic conductivity enhancement among others. A consistent observation of the microwave effect on the band structure modification has been established, which in most cases resulted in band-gap decrease due to the creation of defects levels above the valence band highest unoccupied level and below the conduction band lowest occupied level. These lead to the overall agreement that oxygen vacancy enhance electronic conductivity and carriers mobility in most materials and devices leading to easy transport of injected electrons through oxygen deficient sites. Further thermodynamic nonequilibrium processes can be studied from other electromagnetic radiation sources such as UV light to achieve same or better results. However, in devices where exciton dissociation and recombination processes occur, challenging control of interfacial oxygen vacancy is required in order not to degrade their physico-chemical performances. Finally, the attention of the reader should also be directed to the importance of XPS analysis which is one of the most accessible analytical techniques needed for effective oxygen vacancy characterization.

Acknowledgements

One of the authors (G.L.) gratefully acknowledges the University of Witwatersrand fianacial support via the URC postdoctoral fellowship (#A0055687).

References

1. Cliffe MJ, Wan W, Zou XD, Chater PA, Kleppe AK, et al. (2014) Correlated defect nanoregions in a metal- organic framework. Nat Commun 5: 4176.
2. Taylor J, Dekura S, Ikeda R, Kitagawa H (2015) Defect control to enhance proton conductivity in a metal-organic framework. Chem Mater 27: 2286-2289.
3. Fu J, Hassan FM, Zhong C, Lu J, Liu H, et al. (2017) Defect engineering of chalcogen-tailored oxygen electrocatalysts for rechargeable quasi-solid-state zinc-air batteries. Adv Mater 29: 1702526.
4. Pan X, Min-Quan Y, Fu X, Zhang N, Yi-Jun X (2013) Defective TiO2 with oxygen vacancies: synthesis, properties and photocatalytic applications. Nanoscale 5: 3601.
5. Ting Su, Yang Y, Yong Na, Ruiqing Fan, Liang Li, et al. (2015) An insight into the role of oxygen vacancy in hydrogenated Tio2 nanocrystals in the performance of dye-sensitized solar cells. ACS Appl Mater Interfaces 7: 3754-3763.
6. Zhang L, Wang S, Chao Lu (2015) Detection of oxygen vacancies in oxides by defect-dependent cataluminescence. Anal Chem 87: 7313-7320.
7. Cheng F, Zhang T, Zhang Y, Du J, Han X, et al. (2013) Enhancing electrocatalytic oxygen reduction on mno2 with vacancies. Angew Chem Int Ed 52: 2474 -2477.
8. Veal BW, Kim SK, Zapol P, Iddir H, Baldo PM, et al. (2016) Interfacial control of oxygen vacancy doping and electrical conduction in thin film oxide heterostructures. Nat Commun 7.
9. Kim HS, Cook JB, Lin H, Ko JS, Tolbert SH, et al. (2017) Oxygen vacancies enhance pseudocapacitive charge storage properties of MoO3-x. Nat Mater 16: 454-460.
10. Ganduglia-Pirovano MV, Hofmann A, Sauer J (2007) Oxygen vacancies in transition metal and rare earth oxides: current state of understanding and remaining challenges. Surf Sci Rep 62: 219-270.
11. Janotti A, Van de Walle CG (2007) Native point defects in ZnO. Phys Rev B 76: 165202.
12. Erhart P, Albe K, Klein A (2006) First-principles study of intrinsic point defects in ZnO: role of band structure, volume relaxation, and finite-size effects. Phys Rev B 73: 205203.

13. Ai-Zhen L, Jian-Biao C, Cheng-Wei W, Xiao-Feng S, Li Y, et al. (2016) Enhanced field emission properties from oxygen-deficient a-Fe2O3 nanorod arrays. J Vac Sci Technol B 34: 021803.
14. Wang M, Wang Y, Liu J, Pei C, Liu B, et al. (2017) Enhanced sensing performance and sensing mechanism of hydrogenated NiO particles. Sensors Actuators B 250: 208-214.
15. Fan YH, Ho CY, Chang YJ (2017) Enhancement of dye-sensitized solar cells efficiency using mixed-phase TiO2 nanoparticles as photoanode. Scanning.
16. Ghosh D, Halder G, Sahasrabudhe A, Bhattacharyya S (2016) A microwave synthesized CuxS and graphene oxide nanoribbon composite as a highly efficient counter electrode for quantum dot sensitized solar cells. Nanoscale 8: 10632.
17. Karppinen M, Fjellvåg H, Konno T, Morita Y, Motohashi T, et al. (2004) Evidence for Oxygen Vacancies in Misfit-Layered Calcium Cobalt Oxide, [CoCa2O3]qCoO2. Chem Mater 16: 2790-2793.
18. Ahmad R, Tripathy N, Ahn MS, Bhat KS, Mahmoudi T, et al. (2017) Highly efficient non-enzymatic glucose sensor based on CuO modified vertically-grown ZnO nanorods on electrode. Sci Rep 7: 5715.
19. Huygh S, Bogaerts A, Neyts EC (2016) How oxygen vacancies activate CO2 dissociation on TiO2 anatase (001). J Phys Chem C 120: 21659-21669.
20. Stefik M, Heiligtag FJ, Niederberger M, Gratzel M (2013) Improved Nonaqueous Synthesis of TiO2 for Dye-Sensitized Solar Cells. ACS Nano 7: 8981-8989.
21. Carrettin S, Hao Y, Aguilar-Guerrero V, Gates BC, Trasobares S, et al. (2007) Increasing the Number of Oxygen Vacancies on TiO2 by Doping with Iron Increases the Activity of Supported Gold for CO Oxidation. Chem Eur J 13: 7771-7779.
22. Zhang J, Zhao Z, Wang X, Yu T, Guan J, et al. (2010) Increasing the oxygen vacancy density on the TiO2 surface by la-doping for dye-sensitized solar cells. J Phys Chem C 114: 18396-18400.
23. Park S, Ahn HS, Lee CK, Kim H, Jin H, et al. (2008) Interaction and ordering of vacancy defects in NiO. Phys Rev B 77: 134103.
24. Brahma S, Liu CP, Shivashankar SA (2017) Microwave irradiation assisted, one pot synthesis of simple and complex metal oxide nanoparticles: a general approach. J Phys D Appl Phys 50: 40LT03.
25. Su XF, Chen JB, He RM, Li Y, Wang J, et al. (2017) The preparation of oxygen-deficient ZnO nanorod arrays and their enhanced field emission. Mater Sci Semicond Process 67: 55-61.
26. Simo A, Kaviyarasu K, Mwakikunga B, Madjoe R, Gibaudv A, et al. (2017) Phase transition study in strongly correlated VO2 based sensing systems transition study in strongly correlated VO2 based sensing systems. J Electron Spectros Relat Phenomena 216: 23-32.
27. Qi X, Zheng W, Li X, He G (2016) Multishelled NiO hollow microspheres for high- performance supercapacitors with ultrahigh energy density and robust cycle life. Sci Rep 6: 33241.
28. Ren H, Yu R, Wang J, Jin Q, Yang M, et al. (2014) Multishelled TiO2 hollow microspheres as anodes with superior reversible capacity for lithium ion batteries. Nano Lett 14: 6679-6684.
29. Wang J, Tang H, Ren H, Yu R, Qi J, et al. (2014) pH-Regulated synthesis of multi-shelled manganese oxide hollow microspheres as supercapacitor electrodes using carbonaceous microspheres as templates. Adv Sci 1: 1400011.
30. Xu S, Hessel CM, Ren H, Yu R, Jin Q, et al. (2014) α-Fe2O3 multi- shelled hollow microspheres for lithium ion battery anodes with superior capacity and charge retention. Energy Environ Sci 7: 632.
31. Sun C, Wang Y, Zou J, Smith SC (2011) A formation mechanism of oxygen vacancies in a MnO2 monolayer: a DFT + U study. Phys Chem Chem Phys 13: 11325-11328.
32. Teresa OH (2017) A study on an oxygen vacancy and conductivity of oxide thin films deposited by rf magnetron sputtering and annealed in a vacuum. Trans Electr Electron Mater 18: 21.
33. Li N, Du K, Liu G, Xie Y, Zhou G, et al. (2013) Effects of oxygen vacancies on the electrochemical performance of tin oxide. J Mater Chem A 1: 1536.
34. Sushko PV, Rosso KM, Zhang JG, Liu J, Sushko ML (2013) Oxygen vacancies and ordering of d-levels control voltage suppression in oxide cathodes: the case of spinel LiNi0.5Mn1.5O4-δ. Adv Funct Mater 23: 5530-5535.
35. Gaggiotti G (1994) Surface chemistry of tin oxide based gas sensors. J Appl Phys 76: 4467.
36. Wu QH, Thissen A, Jaegermann W, Liu ML (2004) Photoelectron spectroscopy study of oxygen vacancy on vanadium oxides surface. Appl Surf Sci 236: 473.
37. Lambrecht W, Djafari-Rouhani B, Vennik J (1981) Electronic structure of the vanadyl oxygen vacancy in V2O5: periodic vacancy single layer model. Solid State Commun 39: 257.
38. Tit N (1993) Electronic-structure of a single oxygen vacancy in rutile TiO2. Nuovo Cimento 15: 1405.
39. Bredow T, Pacchioni G (2002) Electronic structure of an isolated oxygen vacancy at the TiO2(110) surface. Chem Phys Lett 355: 417.
40. Wu X, Selloni A, Lazzeri M, Nayak SK (2003) Oxygen vacancy mediated adsorption and reactions of molecular oxygen on the TiO2(110) surface. Phys Rev B 68: 241402.
41. Hofmann SJ, Clark M, Oppel I, Hahndorf I (2002) Hydrogen adsorption on the tetragonal ZrO2(101) surface: a theoretical study of an important catalytic reactant. Phys Chem Chem Phys 4: 3500.
42. Safonov AA, Bagaturyants AA, Korkin AA (2003) Oxygen vacancies in tetragonal ZrO2: Ab initio embedded cluster calculations. Microelectron Eng 69: 629.
43. Sayle TXT, Parker SC, Catlow CRA (1994) The role of oxygen vacancies on ceria surfaces in the oxidation of carbon-monoxide. Surf Sci 316: 329.
44. Jiang Y, Adams JB, van Schilfgaarde M, Sharma R, Crozier PA (2005) Theoretical study of environmental dependence of oxygen vacancy formation in CeO2. Appl Phys Lett 87: 141917.
45. Skorodumova NV, Simak SI, Lundqvist BI, Abrikosov IA, Johansson B (2002) Quantum origin of the oxygen storage capability of ceria. Phys Rev Lett 89: 166601.
46. Nolan M, Fearon JE, Watson GW (2006) Oxygen vacancy formation and migration in ceria. Solid State Ion 177: 3069.
47. Mori-Sanchez P, Recio JM, Silvi B, Sousa C, Pendas AM, et al. (2002) Rigorous characterization of oxygen vacancies in ionic oxides. Phys Rev B 66: 075103.
48. Bredow T, Gerson AR (2000) Effect of exchange and correlation on bulk properties of MgO, NiO, and CoO. Phys Rev B 61: 5194.
49. Kumar V, Swart HC, Ntwaeaborwa OM, Kroon RE, Terblans JJ, et al. (2013) Origin of the red emission in zinc oxide nanophosphors. Materials Letters 101: 57-60.
50. Pandey A, Rai VK, Kumar V, Swart HC (2015) Upconversion based temperature sensing ability of Er3+-Yb3+ codoped SrWO4: an optical heating phosphor. "Sens Actuators B Chem 209: 352-358.
51. Som S, Kunti AK, Kumar V, Kumar V, Dutta S, et al. (2014) Defect correlated fluorescent quenching and electron phonon coupling in the spectral transition of Eu3+ in CaTiO3 for red emission in display application. J Appl Phys 115: 193101.
52. Ngom BD, Mpahane T, Manyala N, Nemraoui O, Buttner U, et al. (2009) Structural and optical properties of nano-structured tungsten-doped ZnO thin films grown by pulsed laser deposition. Appl Surf Sci 2557: 4153-4158.
53. Magdalane CM, Kaviyarasu K, Vijaya JJ, Siddhardha B, Jeyaraj B, et al. (2018) Evaluation on the heterostructured CeO2/Y2O3 binary metal oxide nanocomposites for UV/Vis light induced photocatalytic degradation of Rhodamine - B dye for textile engineering application. J Alloys Compd 727: 1324-1337.
54. Kabongo GL, Mhlongo GH, Mothudi BM, Mbule PS, Hillie KT, et al. (2017) Structural, photoluminescence and XPS properties of Tm3+ ions in ZnO nanostructures. J Lum 187: 141-153.

55. Yaghi OM, O' Keeffe M, Ockwig NW, Chae HK, Eddaoudi M, et al. (2003) Reticular synthesis and the design of new materials. Nature 423: 705-714.
56. Dolgopolova EA, Brandt AJ, Ejegbavwo OA, Duke AS, Maddumapatabandi TD, et al. (2017) Electronic properties of bimetallic metal-organic frameworks (MOFs): tailoring the density of electronic states through mof modularity. J Am Chem Soc 139: 5201-5209.
57. Guan BY, Kushima A, Yu L, Li S, Li J, et al. (2017) Coordination polymers derived general synthesis of multishelled mixed metal-oxide particles for hybrid supercapacitors. Adv Mater 29: 1605902.
58. Hu H, Guan B, Xia B, Wen X (2015) Designed formation of Co3O4/NiCo2O4 double-shelled nanocages with enhanced pseudocapacitive and electrocatalytic properties. J Am Chem Soc 137: 5590-5595.
59. Zhang G, Wen X (2014) General synthesis of multi-shelled mixed metal oxide hollow spheres with superior lithium storage properties. Angew Chem Int Ed 53: 9041-9044.
60. Li H, Ma H, Yang M, Wang B, Shao H, et al. (2017) Highly controlled synthesis of multi-shelled NiO hollow microspheres for enhanced lithium storage properties. Mater Res Bull 87: 224-229.
61. Jiang Z, Li Z, Qin Z, Sun H, Jiao X et al. (2013) LDH nanocages synthesized with MOF templates and their high performance as supercapacitors. Nanoscale 5: 11770.
62. Li X, Wang L, Shi J, Du N, He G (2016) Multishelled nickel-cobalt oxide hollow microspheres with optimized compositions and shell porosity for high-performance pseudocapacitors. ACS Appl Mater Interfaces 8: 17276-17283.
63. Li R, Hu Z, Shao X, Cheng P, Li S, et al. (2016) Large scale synthesis of NiCo layered double hydroxides for superior asymmetric electrochemical capacitor. Sci Rep 6: 18737.
64. Lu XF, Gu LF, Wang JW, Wu JX, Liao PQ, et al. (2017) Bimetal-organic framework derived CoFe2O4/C porous hybrid nanorod arrays as high-performance electrocatalysts for oxygen evolution reaction. Adv Mater 29: 1604437.
65. Qi H, Wenji Z, Li X, He G (2016) Multishelled NiO hollow microspheres for high- performance supercapacitors with ultrahigh energy density and robust cycle life. Sci Rep 6: 33241.
66. Kabongo GL, Mhlongo GH, Mothudi BH, Mbule PS, Hillie KT, et al. (2017) Structural, photoluminescence and XPS properties of Tm3+ ions in ZnO nanostructures. J Lum 187: 141-153.
67. Fell CR, Qian D, Carroll KJ, Chi M, Jones JL, et al. (2013) Correlation between oxygen vacancy, microstrain, and cation distribution in lithium-excess layered oxides during the first electrochemical cycle. Chem Mater 25: 1621-1629.
68. Kaur J, Kumar P, Sathiaraj TS, Thangaraj R (2013) Structural, optical and fluorescence properties of wet chemically synthesized ZnO:Pd2+ nanocrystals. Int Nano Lett 3: 1-7.
69. Raju K, Nkosi FP, Viswanathan E, Mathe MK, Damodaran K, et al. (2016) Microwave-enhanced electrochemical cycling performance of the LiNi0.2Mn1.8O4 spinel cathode material at elevated temperature. Phys Chem Chem Phys 18: 13074-13083.
70. Kebede MA, Yannopoulos SN, Sygellou L, Ozoemena KI (2017) High-voltage LiNi0.5Mn1.5O4-δ spinel material synthesized by microwave-assisted thermo-polymerization: some insights into the microwave-enhancing physico-chemistry. J Electrochem Soc 164: A3259-A3265.
71. Jafta CJ, Mathe MK, Manyala N, Roos WD, Ozoemena KI (2013) Microwave-assisted synthesis of high-voltage nanostructured LiMn1.5Ni0.5O4 spinel: tuning the Mn3+ content and electrochemical performance. ACS Appl Mater Interfaces 5: 7592-7598.
72. Zhu YJ, Chen F (2014) Microwave-assisted preparation of inorganic nanostructures in liquid phase. Chem Rev 114: 6462-6555.
73. Sun J, Wang W, Yue Q (2016) Review on microwave-matter interaction fundamentals and efficient microwave-associated heating strategies. Materials 9: 231.
74. Jacob J, Chia LH (1995) Thermal and non-thermal interaction of microwave radiation with materials. J Mat Sci 30: 5321-5327.
75. Newnham RE, Jang SJ, Xu M, Jones F (1991) Fundamental interaction mechanisms between microwaves and matter. Ceramic Transactions 21. Proceedings of the symposium on microwave theory and application in materials processing annual meeting of the american ceramic society.
76. Pfau A, Schierbaum KD (1994) The electronic structure of stoichiometric and reduced CeO 2 surfaces: an XPS, UPS and HREELS study. Surface Science 321: 71-80.
77. Horikoshi S, Minatodani Y, Tsutsumi H, Uchida H, Abe M (2013) Influence of lattice distortion and oxygen vacancies on the UV-driven/microwave assisted TiO2 photocatalysis. J Photochem Photobiol A: Chem 265: 20-28.
78. Janotti A, Van de Walle CG (2009) Fundamentals of zinc oxide as a Semiconductor. Rep Prog Phys 72: 126501.
79. Khan ME, Khan MM, Cho MH (2017) Ce3+-ion, surface oxygen vacancy, and visible light-induced photocatalytic dye degradation and photocapacitive performance of CeO2- graphene nanostructures. Scientific Reports. 7: 5928.
80. Su D, Xie X, Dou S, Wang G (2014) CuO single crystal with exposed {001} facets - A highly efficient material for gas sensing and Li-ion battery applications. Scientific Reports 4: 5753.
81. Golbamaki N, Rasulev B, Cassano A, Robinson RLM, Benfenati E, et al. (2015) Genotoxicity of metal oxide nanomaterials: review of recent data and discussion of possible mechanisms. Nanoscale 7: 2154-2198.
82. Li Y, Shen W (2014) Morphology-dependent nanocatalysts: rod-shaped oxides. Chem Soc Rev 43: 1543-1574.
83. Liu B, Yang H, Wei A, Zhao H, Ning L, et al. (2015) Superior photocatalytic activities of NiO octahedrons with loaded AgCl particles and charge separation between polar NiO {111} surfaces. Appl Catal B Environ 172: 165-173.
84. Ashrafi A, Jagadish C (2007) Review of zincblende ZnO: stability of metastable ZnO phases. J Appl Phys 102: 071101.
85. Jiang H, Stewart DA (2017) Using dopant to tune oxygen vacancy formation in Transition metal oxide restive memory. ACS Appl Mater Interfaces 9: 16296-16304.
86. Kabongo GL, Mhlongo GH, Mothudi BM, Hillie KT, Swart HC, et al. (2014) Enhanced exciton emission from ZnO nano-phosphor induced by Yb3+ ions. Materials Letters 119: 71-74.
87. Kabongo GL, Mhlongo GH, Malwela T, Mothudi BM, Hillie KT, et al. (2014) Microstructural and photoluminescence properties of sol-gel derived Tb3+ doped ZnO nanocrystals. J Alloys Compds 591: 156-163.
88. Mhlongo GH, Motaung DE, Swart HC (2015) Pd2+ doped ZnO nanostructures: Structural, luminescence and gas sensing properties. Mater Lett 160: 200-205.
89. Mhlongo GH, Shingange K, Tshabalala ZP, Dhonge BP, Mahmoud FA, et al. (2016) Room temperature ferromagnetism and gas sensing in ZnOnanostructures: Influence of intrinsic defects and Mn, Co, Cu doping. Appl Surf Sci 390: 804-815.
90. Park JH, Lee YJ, Bae JS, Kim BS, Cho YC, et al. (2015) Analysis of oxygen vacancy in co-doped ZnO using the electron density distribution obtained using MEM. Nanoscale Res Lett 10: 186.
91. Sreeprasad TS, Nguyen P, Kim N, Berry V (2013) Controlled, Defect-Guided, Metal- Nanoparticle Incorporation onto MoS2 via Chemical and Microwave Routes: Electrical. Thermal, and Structural Properties, Nano Lett 13: 4434-4441.
92. Yoshida K, Sonobe T, Zen H, Hachiya K, Okumura K, et al. (2015) Effect of microwave irradiation on the electronic structure of ZnO. J Phys Chem Solids 83: 47-51.
93. Khamlich S, Khamliche T, Dhlamini MS, Khenfouch M, Mothudi BM, et al. (2017) Rapid microwave-assisted growth of silver nanoparticles on 3D graphene networks for supercapacitor application. J Colloid Interface Sci 493: 130-137.
94. Ming B, Li J, Kang F, Pang G, Zhang Y, et al. (2012) Microwave-hydrothermal synthesis of birnessite-type MnO2 nanospheres as supercapacitor electrode materials. J Power Sources 198: 428-431.

95. Alsharaeh E, Ahmed F, Aldawsari Y, Khasawneh M, Abuhimd H, et al. (2016) Novel synthesis of holey reduced graphene oxide (HRGO) by microwave irradiation method for anode in lithium-ion batteries. Sci Rep 6: 29854.

96. Kiani A, Dastafkan K, Obeydavi A, Rahimi M (2017) Solid solutions of gadolinium doped zinc oxide nanorods by combined microwave-ultrasonic irradiation assisted crystallization. Solid State Sci 74: 152-167.

97. Motaung DE, Mhlongo GH, Nkosi SS, Malgas GF, Mwakikunga BW, et al. (2014) Shape-Selective Dependence of Room Temperature Ferromagnetism Induced by Hierarchical ZnO Nanostructures. ACS Appl Mater Interfaces 6: 8981-8995.

98. Pahalagedara LR, Dharmarathna S, Kingondu CK, Pahalagedara MN, Meng YT, et al. (2014) Microwave-assisted hydrothermal synthesis of αMnO2: lattice expansion via rapid temperature ramping and framework substitution. J Phys Chem C 118: 20363-20373.

99. Mohamed RM, Aazam ES (2012) Synthesis and characterization of CeO2-SiO2 nanoparticles by microwave-assisted irradiation method for photocatalytic oxidation of methylene blue dye. Int J Photoenergy ID 928760.

100. Liu FW, Hsu CH, Chen FS, Lu CH (2012) Microwave-assisted solvothermal preparation and photoluminescence properties of Y2O3:Eu3+ phosphors. Ceramics International 38: 1577-1584.

101. Pahalagedara LR, Dharmarathna S, Kingondu CK, Pahalagedara MN, Meng YT, et al. (2014) Microwave-assisted hydrothermal synthesis of α-MnO2: lattice expansion via rapid temperature ramping and framework substitution. J Phys Chem C 118: 20363-20373.

102. Mohamed RM, Aazam ES (2012) Synthesis and characterization of CeO2-SiO2 nanoparticles by microwave-assisted irradiation method for photocatalytic oxidation of methylene blue dye. Int J Photoenergy ID 928760.

103. Hai-Bo F, Shao-Yan Y, Pan-Feng Z, Hong-Yuan W, Xiang-Lin L, et al. (2007) Investigation of oxygen vacancy and interstitial oxygen defects in zno films by photoluminescence and x-ray photoelectron spectroscopy. Chinese Phys Lett 24: 2108.

104. Liu LZ, Li TH, Wu XL, Shen JC, Chu PK (2012) Identification of oxygen vacancy types from Raman spectra of SnO2 nanocrystals. J Raman Spectrosc 43: 1423-1426.

105. Nishida K, Osada M, Takeuchi H, Yosiaki I, Sakai J, et al. (2008) Raman spectroscopy study of oxygen vacancies in PbTiO3 thin films generated heat-treated in hydrogen atmosphere. J Appl Phys 47: 7510-7513.

106. Guo M, Lu J, Wu Y, Wang Y, Luo M (2011) UV and visible raman studies of oxygen vacancies in rare-earth-doped ceria. Langmuir 27: 3872-3877.

107. Wang ZL, Yin JS, Jiang YD (2000) EELS analysis of cation valence states and oxygen vacancies in magnetic oxides. Micron 31: 571-580.

108. Wu QH, Thissen A, Jaegermann W, Liu M (2004) Photoelectron spectroscopy study of oxygen vacancy on vanadium oxides surface. Appl Surf Sci 236: 473-478.

109. Kumar V, Swart HC, Ntwaeaborwa OM, Kroon RE, Terblans JJ, et al. (2013) Origin of the red emission in zinc oxide nanophosphors. Materials Letters 101: 57-60.

110. Li Y, Feng Y, Zhou Q, Wu M, Mi J (2017) Effects of microwave irradiation on the structure of Zinc oxide sorbents for high temperature coal gas desulfurization. Energy Fuels 31: 8512-8520.

111. Yang H, Wang YQ, Jia QX (2010) Oxygen concentration and its effect on the leakage current in BiFeO3, thin films. Appl Phys Lett 96: 012909.

112. Ciatto G, Di Trolio A, Fonda E, Alippi P, Testa AM (2011) Evidence of Cobalt-Vacancy Complexes in Zn1-x CoxO. Phys Rev Lett 107: 127206.

113. Yan D, Wang W, Luo X, Chen C, Zeng Y, et al. (2018) NiCo2O4 with oxygen vacancies as better performance electrode material for supercapacitor. Chem Eng J 334: 864-872.

114. Zhai T, Xie S, Yu M, Fang P, Liang C, et al. (2014) Oxygen vacancies enhancing capacitive properties of MnO2 nanorods for wearable asymmetric supercapacitors. Nano Energy 8: 255-263.

115. Dillip GR, Banerjee AN, Anitha VC, Raju BDP, Joo SW, et al. (2016) Oxygen vacancy-induced structural, optical, and enhanced supercapacitive performance of zinc oxide anchored graphitic carbon nanofiber hybrid electrodes. ACS Appl Mater Interfaces 8: 5025-5039.

116. Xiang K, Xu Z, Qu T, Tian Z, Zhang Y, et al. (2017) Two dimensional oxygen-vacancy-rich Co3O4 nanosheets with excellent supercapacitor performances. Chem Commun 53: 12410.

117. Guo W, Sun W, Wang Y (2015) Multilayer CuO@NiO hollow spheres: microwave- assisted metal-organic-framework derivation and highly reversible structure-matched stepwise lithium storage. ACS Nano 9: 11462-11471.

118. Li GC, Liu PF, Liu R, Liu M, Tao K, et al. (2016) MOF-derived hierarchical double-shelled NiO/ZnO hollow spheres for high-performance supercapacitors. Dalton Trans 45: 13311.

119. Zhai T, Xie S, Yu M, Fang P, Liang C, et al. (2014) Oxygen vacancies enhancing capacitive properties of MnO2 nanorods for wearable asymmetric supercapacitors Nano Energy 8: 255-263.

120. Salunkhe RR, Kaneti YV, Yamauchi Y (2017) Metal-organic framework-derived nanoporous metal oxides toward supercapacitor applications: progress and prospects. ACS Nano 11: 5293-5308.

121. Ge X, Li Z, Wang C, Yin L (2015) Metal-organic frameworks derived porous core/shell structured ZnO/ZnCo2O4/C hybrids as anodes for high-performance lithium-ion battery. ACS Appl Mater Interfaces 7: 26633-26642.

122. Dembele A, Rahman M, MacElroy JMD, Dowling DP (2012) Evaluation of microwave plasma sintering for the fabrication of dye sensitized solar cell (DSSC) electrodes. J Nanosci Nanotechnol 12: 4769-74.

123. Cao Q, Yang S, Gao Q, Lei L, Yu Y, et al. (2016) Fast and controllable crystallization of perovskite films by microwave irradiation process. ACS Appl Mater Interfaces 8: 7854-7861.

124. Po-Shen S, Chuan-Ming T, Ta-Chuan K, Ching-Kuei S, Ming-Hsien L, et al. (2015) Microwave-assisted synthesis of titanium dioxide nanocrystalline for efficient dye-sensitized and perovskite solar cells. Solar Energy 120: 345-356.

125. Liu H, Wu Z, Gao H, Shao J, Zou H, et al. (2017) One-step preparation of cesium lead halide CsPbX3 (X = Cl, Br, and I) perovskite nanocrystals by microwave irradiation. ACS Appl Mater Interfaces 9: 42919-42927.

126. Abulikemu M, Neophytou M, Barbe JM, Tietze ML, El Labban A, et al. (2017) Microwave-synthesized tin oxide nanocrystals for low-temperature solution-processed planar junction organo-halide perovskite solar cells. J Mater Chem A 5: 7759-7763.

127. Menzies DB, Dai Q, Cheng YB, Simon GP, Spiccia L (2006) One-step microwave calcination of ZrO2-coated TiO2 electrodes for use in dye-sensitized solar cells. C R Chimie 9: 713-716.

128. Uchida S, Tomiha M, Masaki N, Miyazawa A, Takizawa H (2004) Preparation of TiO2 nanocrystalline electrode for dye-sensitized solar cells by 28GHz microwave irradiation. Sol Energy Mater Sol Cells 81: 135-139.

129. Wang HE, Zheng LX, Liu CP, Liu YK, Luan CY, et al. (2011) Rapid microwave synthesis of porous TiO2 spheres and their applications in dye-sensitized solar cells. J Phys Chem C 115: 10419-10425.

130. Hart JN, Cervinia R, Chenga YB, Simona GP, Spiccia L (2004) Formation of anatase TiO2 by microwave processing. Sol Energy Mater Sol Cells 84: 135-143.

131. Su T, Yang Y, Na Y, Fan R, Li L, et al. (2015) An Insight into the Role of Oxygen Vacancy in Hydrogenated TiO2 Nanocrystals in the Performance of Dye-Sensitized Solar Cells. ACS Appl Mater Interfaces 7: 3754-3763.

132. Hart JN, Menzies D, Cheng YB, Simon GP, Spiccia L (2006) Microwave processing of TiO2 blocking layers for dye-sensitized solar cells. J Sol-Gel Sci Techn 40: 45-54.

133. Ghosh D, Halder G, Sahasrabudhe A, Bhattacharyya S (2016) A microwave synthesized CuxS and graphene oxide nanoribbon composite as a highly efficient counter electrode for quantum dot sensitized solar cells. Nanoscale 8: 10632.

134. Wang M, Wang Y, Liu J, Pei C, Liu B, et al. Enhanced sensing performance and sensing mechanism of hydrogenated NiO particles. Sensors Actuators B 250: 208-214.

135. Felix S, Chakkravarthy RBP, Grace AN (2015) Microwave assisted synthesis of copper oxide and its application in electrochemical sensing. IOP Conf Ser Mater Sci Eng 73: 012115.

136. Alali KT, Lu Z, Zhang H, Liu J, Liu Q, et al. (2017) P-p heterojunction CuO/CuCo2O4 nanotubes synthesized via electrospinning technology for detecting n-propanol gas at room temperature. Inorg Chem Front 4: 1219-1230.

137. Motaung DE, Mhlongo GH, Makgwane PR, Dhonge BP, Cummings FR, et al. (2018) Ultra-high sensitive and selective H2 gas sensor manifested by interface of n-n heterostructure of CeO2-SnO2 nanoparticles. Sensors Actuators B: Chemi 254 : 984-995.

138. Azam A, Habib SS, Salah NA, Ahmed F (2013) Microwave-assisted synthesis of SnO2 nanorods for oxygen gas sensing at room temperature. Int J Nanomedicine 8: 3875-3882.

139. Shingange K, Tshabalala ZP, Ntwaeaborwa OM, Motaung DE, Mhlongo GH (2016) Highly selective NH3 gas sensor based on Au loaded ZnO nanostructures prepared using microwave-assisted method. J Colloid Interf Sci 479: 127-138.

140. Luo LB, Wang XH, Xie C, Li ZJ, Lu R, et al. (2014) One-dimensional CuO nanowire: synthesis, electrical, and optoelectronic devices application. Nanoscale Res Lett 9: 637.

141. Su XF, Chen JB, He RM, Li Y, Wang J et al. (2017) The preparation of oxygen-deficient ZnO nanorod arrays and their enhanced field emission. Mater Sci Semicond Process 67: 55-61.

142. Su J, Ye S, Yi X, Lu FQ, Yang XB, et al. (2017) Influence of oxygen vacancy on persistent luminescence in ZnGa2O4:Cr3+ and identification of electron carriers. 7: 734-743.

143. Zhang J, Wang X, Zhang X, Zhao X, Liu X, et al. (2011) Microwave synthesis of NaLa(MoO4)2 microcrystals and their near-infrared luminescent properties with lanthanide ion doping (Er3+,Nd3+,Yb3+). Inorg Chem Communi 14: 1723-1727.

144. Zhang Y, Xu J, Cui Q, Yang B (2017) Eu3+-doped Bi4Si3O12 red phosphor for solid state lighting: microwave synthesis, characterization, photoluminescence properties and thermal quenching mechanisms. Sci Rep 7: 42464.

145. Liu FW, Hsu CH, Chen FS, Lu CH (2012) Microwave-assisted solvothermal preparation and photoluminescence properties of Y2O3:Eu3+ phosphors. Ceramics Int 38: 1577-1584.

146. Aijaz S, Ahmed AS, Pandey RS, Choubey RK (2017) Synthesis, structural and optical properties of transition metal doped ZnO Nanoparticles. In: Jain V, Rattan S, Verma A (eds) Recent Trends in Materials and Devices. Springer Proceedings in Physics 178: 205-210.

147. Zhang S, Hu Y, Duan H (2016) Phosphorescence performance of La3GaGe5O16:Tb3+ by enhancing the bridging oxygen vacancies. Opt Mat Exp 6: 1998-2013.

148. Freysoldt C, Grabowski B, Hickel T, Neugebauer J, Kresse G (2014) "First principles calculations for point defects in solids". Rev Mod Phys 86: 253-304.

149. Xu X, Wang Y, Gong Y, Zeng W, Li Y (2010) Effect of oxygen vacancies on the red phosphorescence of Sr2SnO4:Sm3+ phosphor. Opt Exp 18: 16989-16994.

150. Liao AZ, Chen JB, Wang CW, Su XF, Li Y, et al. (2016) Enhanced field emission properties from oxygen-deficient α-Fe2O3 nanorod arrays. J Vac Sci Technol B 34: 021803.